NASA/CR—2008-215238

# Intelligent Engine Systems

## Thermal Management and Advanced Cooling

*Robert Bergholz*
*General Electric Aviation, Cincinnati, Ohio*

June 2008

# NASA STI Program . . . in Profile

Since its founding, NASA has been dedicated to the advancement of aeronautics and space science. The NASA Scientific and Technical Information (STI) program plays a key part in helping NASA maintain this important role.

The NASA STI Program operates under the auspices of the Agency Chief Information Officer. It collects, organizes, provides for archiving, and disseminates NASA's STI. The NASA STI program provides access to the NASA Aeronautics and Space Database and its public interface, the NASA Technical Reports Server, thus providing one of the largest collections of aeronautical and space science STI in the world. Results are published in both non-NASA channels and by NASA in the NASA STI Report Series, which includes the following report types:

- TECHNICAL PUBLICATION. Reports of completed research or a major significant phase of research that present the results of NASA programs and include extensive data or theoretical analysis. Includes compilations of significant scientific and technical data and information deemed to be of continuing reference value. NASA counterpart of peer-reviewed formal professional papers but has less stringent limitations on manuscript length and extent of graphic presentations.

- TECHNICAL MEMORANDUM. Scientific and technical findings that are preliminary or of specialized interest, e.g., quick release reports, working papers, and bibliographies that contain minimal annotation. Does not contain extensive analysis.

- CONTRACTOR REPORT. Scientific and technical findings by NASA-sponsored contractors and grantees.

- CONFERENCE PUBLICATION. Collected papers from scientific and technical conferences, symposia, seminars, or other meetings sponsored or cosponsored by NASA.

- SPECIAL PUBLICATION. Scientific, technical, or historical information from NASA programs, projects, and missions, often concerned with subjects having substantial public interest.

- TECHNICAL TRANSLATION. English-language translations of foreign scientific and technical material pertinent to NASA's mission.

Specialized services also include creating custom thesauri, building customized databases, organizing and publishing research results.

For more information about the NASA STI program, see the following:

- Access the NASA STI program home page at *http://www.sti.nasa.gov*

- E-mail your question via the Internet to *help@sti.nasa.gov*

- Fax your question to the NASA STI Help Desk at 301–621–0134

- Telephone the NASA STI Help Desk at 301–621–0390

- Write to:
  NASA Center for AeroSpace Information (CASI)
  7115 Standard Drive
  Hanover, MD 21076–1320

NASA/CR—2008-215238

# Intelligent Engine Systems

## Thermal Management and Advanced Cooling

*Robert Bergholz*
*General Electric Aviation, Cincinnati, Ohio*

Prepared under Contract NAS3–01135, Work element 4.2, Task order 37

National Aeronautics and
Space Administration

Glenn Research Center
Cleveland, Ohio 44135

June 2008

# Acknowledgments

The assistance of V. Pandey in creating various iterations of the Unigraphics CAD files is much appreciated. The author is also grateful to D. Wagner for manipulating the Unigraphics CAD files. Many thanks go out to C. Gilman and R. Dunton for skillfully manufacturing the ABS prototypes of the concept parts. Thanks to R. Jendrix, F. Buck, K. Klasing, M. Weaver, T. Taylor, G. Liter, M. Hamdan, S. Lamson, J. Deaton, N. Nirmalan, ASE Technologies, and Parker Hannifin for their input.

This work was sponsored by the Fundamental Aeronautics Program at the NASA Glenn Research Center.

*Level of Review*: This material has been technically reviewed by NASA technical management.

Available from

NASA Center for Aerospace Information
7115 Standard Drive
Hanover, MD 21076–1320

National Technical Information Service
5285 Port Royal Road
Springfield, VA 22161

# Intelligent Engine Systems
## Thermal Management and Advanced Cooling

Robert Bergholz
General Electric Aviation
Cincinnati, Ohio 45215

### 4.2.1 Advanced Thermal Management Systems and Cooling Designs

The objective of the Advanced Turbine Cooling and Thermal Management program is to develop intelligent control and distribution methods for turbine cooling, while achieving a reduction in total cooling flow and assuring acceptable turbine component safety and reliability. The program also will develop embedded sensor technologies and cooling system models for real-time engine diagnostics and health management. Both active and passive control strategies will be investigated that include the capability of intelligent modulation of flow quantities, pressures, and temperatures both within the supply system and at the turbine component level.

Thermal management system concepts were studied, with a goal of reducing HPT blade cooling air supply temperature. An assessment will be made of the use of this air by the active clearance control system as well. Turbine component cooling designs incorporating advanced, high-effectiveness cooling features, will be evaluated. Turbine cooling flow control concepts will be studied at the cooling system level and the component level. Specific cooling features or sub-elements of an advanced HPT blade cooling design will be downselected for core fabrication and casting demonstrations.

### 4.2.2 Advanced Blade Thermal Modeling (ASE Technologies)

## ***Blade Modeling Objective***

One key technology area for the next generation of gas turbine engines is in turbine blade cooling. Improving the blade cooling circuit performance reduces maintenance costs (by improving blade life) and improves engine efficiency by requiring less coolant air or allowing higher turbine inlet temperatures. Developing alternative cooling approaches to the traditional serpentine is one avenue towards this goal. The objective of the current research was to develop a system to evaluate non-traditional blade cooling concepts, and apply the system to developing an advanced blade that demonstrates improved cooling performance over a traditional blade (producing similar metal temperatures with reduced cooling flow). The work was broken into several sections: conceptual screening of ideas, development of an evaluation system, and overall blade thermal analysis. Additional studies were completed to evaluate swirl cooling as an alternative method using CFD tools, and to evaluate a tip sub-model to improve blade tip temperatures. A combined experimental (in conjunction with the USA program) and CFD analysis program of the final blade design was undertaken to verify the performance of the system.

## ***Concept Screening Studies***

To support the advanced conceptual design activities, a screening methodology was developed to quickly evaluate blade internal cooling configurations that do not follow a traditional serpentine design. The screening process has four primary steps. After determining a layout for the internal cooling arrangement, a 1D flow network of the blade is constructed using three sections (hub, pitch and tip). For the purposes of screening the designs, the external heat transfer conditions (heat load, film cooling effectiveness, etc.) are maintained from a baseline, reference serpentine blade. To meet that constraint, the new design internal arrangement must be adjusted to match the flowrate and backflow margin for each filmrow to the base case. Chamber areas, cross-over hole sizes and wall treatments were adjusted to provide the proper flow balance in the new design flow network. Those 1D flow networks were then updated to included thermal effects using the adiabatic flow conditions and correlations for the heat transfer. If necessary, the flow areas were updated and the models re-converged.

The second step was to layout a pitchline geometry. A discretized approach was used for this purpose. The region inside of the blade skin was discretized using a fine quadrilateral mesh (figure 4.2.2.1). Flow passages were then laid out on this mesh, and adjusted until the pitchline flow areas from the 1D flow networks were matched. The passages were also adjusted such that the total metal area from the base design at the pitchline was matched. The edge points from each of the discretized passages are exported to a CAD program, where the blade internal structure was drafted.

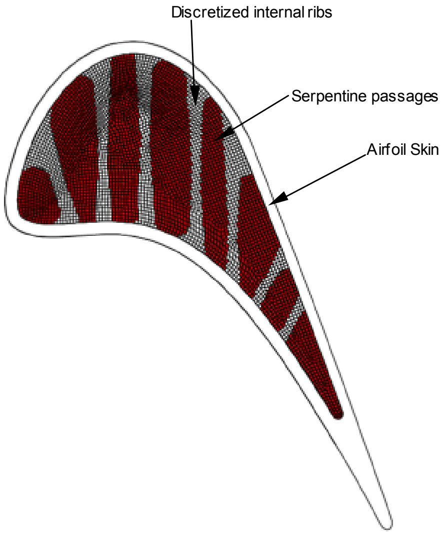

**Figure 4.2.2.1: Use of a discretized method to layout the internal chambers in an example serpentine blade.**

Step three was to build a conduction model to estimate blade temperatures. The pitchline section was extruded to form a 3D section that approximated the midspan of an actual blade (figure 4.2.2.2), and a partial-wrap TBC coating was added. The solid volume for the blade pitchline section was meshed using a fine enough grid for stress analysis (the same mesh was used for steps 3 and 4 – figure 4.2.2.3). Model boundary conditions were drawn from several sources: the external conditions were taken from a code which integrates streamline curvature aero results with film cooling effectiveness and heat transfer coefficient [HTC] correlations; internal conditions (HTC's and coolant temperatures) were taken from the 1D flow networks. Filmholes were added by using advection links that pierce through the metal at the correct location (figure 4.2.2.4). P/thermal was then used to run a steady state conduction analysis to calculate the blade temperatures.

**Figure 4.2.2.2: Solid model of the blade pitchline section after extrusion.**

The final step in the process was to estimate the thermally-induced stresses in the blade section. The mesh from the thermal analysis was transferred to Ansys, and the temperatures from the conduction analysis are mapped to the stress model. Initially, the model was constrained along the outer surface, and an analysis run. The resulting displacements along the bottom surface of the model were then mapped back to the model as constraints, and the upper surface constraints were removed. The final thermal stress model was then run with the displacement constraints to remove any radial growth stresses.

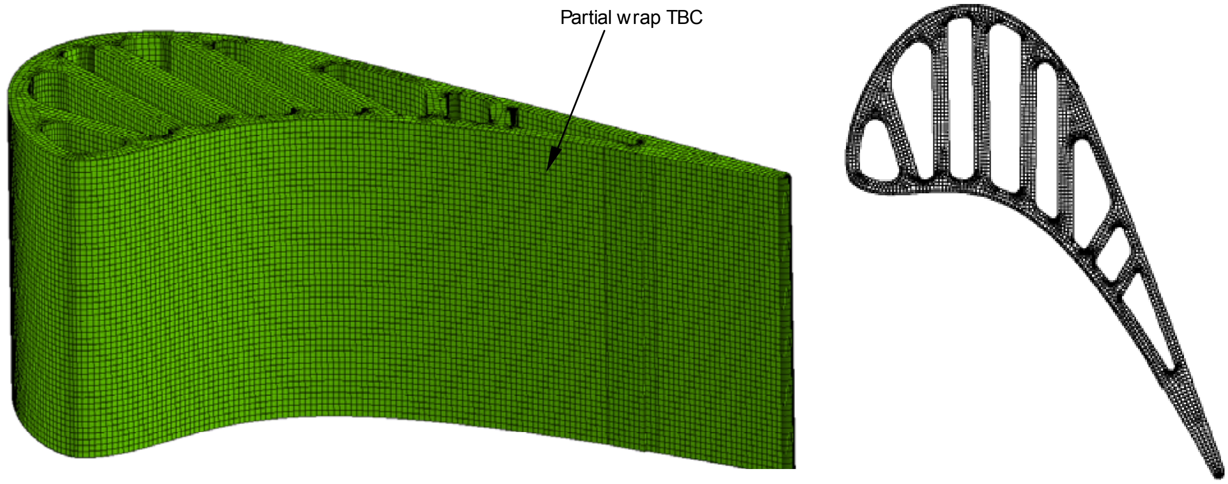

**Figure 4.2.2.3: 3D volume mesh of the pitchline section.**

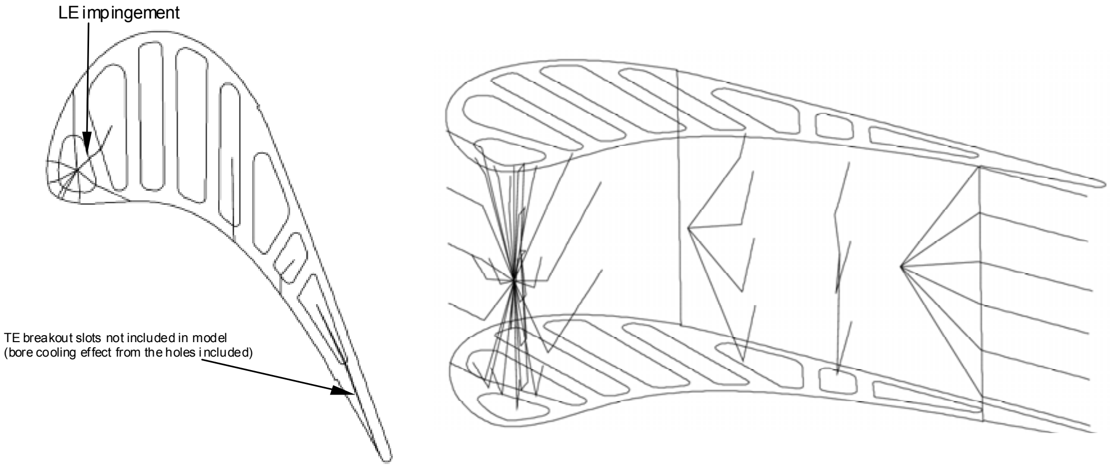

**Figure 4.2.2.4: Advection network for the pitchline section screening thermal analysis.**

## *Design Refinement Analysis of the Advanced Design*

The preliminary screening method simplifies the external thermal boundary conditions, to reduce the time required to assess a given design. To verify that the design selected with the screening approach is viable, a more detailed thermal analysis of the pitchline section was undertaken as a design refinement step. The internal and external conditions were coupled using a three-step process: first, the external heat load was applied using an adiabatic wall temperature and heat transfer coefficient distribution from a streamline curvature / 2D airfoil solution for the blade; second, an internal flow network of 1D elements was coupled to internal face boundary conditions (the flow network supplied air temperature and velocity data to correlations, which then estimated the heat flux to apply at each boundary patch); finally, the coolant exhaust temperature and momentum from the internal solution were used to estimate the film coolant temperature and coverage using film curves (film effectiveness versus distance downstream for a variety of blowing ratios). These steps were then solved iteratively to couple the external film coverage with the internal, back side heat extraction, and provided a higher fidelity thermal analysis than the fixed external heat load used in the screening step. The external boundary conditions from the converged thermal analyses were a combination of the fixed gas adiabatic temperature and heat transfer coefficient (HTC), with the film effectiveness and boundary layer restart HTC impact superimposed. In these detailed models, individual film cooling holes were "drilled" into the model: advection links were passed through the model from the internal air nodes at their correct location and angles. These advection bars were then linked to the local elements, and a bore cooling temperature and HTC were used to estimate the local cooling effect of the holes.

## *3D Baseline Blade Thermal Analysis*

To make a final assessment of the advanced cooling designs, three dimensional blade thermal analyses were used. First, the baseline, traditional serpentine blade was analyzed with the 3D methods. The advanced design blade was also analyzed using the same process as described here for the baseline blade, and a comparison of the results at the design cycle point was made.

The first step in the 3D thermal analysis process was to construct the mesh for the complete blade, including the platform, shank, airfoil and thermal barrier coating (TBC). The thermal solution methodology was similar to that used for the design refinement step (the pseudo-3D design refinement analysis was developed from the existing 3D analysis methodology). Boundary conditions were tagged to all of the exposed mesh faces, internal and external. The external gas temperature and HTC's for the 3D model were taken from several sources: uncooled CFD was used to supply the airfoil and tip gas temperature distributions; the uncooled CFD also provided the blade tip HTC's; a streamline curvature analysis provided the airfoil external HTC's; platform and shank external temperatures and HTC's were estimated from prior thermal analysis models. These external boundary conditions were then modified using the predicted film effectiveness that was solved as part of the thermal solution to provide a combined film temperature and external HTC. Airfoil surface pressures and boundary layer edge momentum were also extracted from the streamline curvature analysis, and were used as boundary condition data for the internal flow network (which models the internal coolant and film holes) and to compute the local blowing ratio for the film rows (used as part of the film effectiveness determination). A 1D internal flow network was constructed for the blade. The flow network modeled the coolant flow from the slot bottom supply through the serpentine passages (with friction factor models for the pressure drop due to the turbulators and tip turns), across the impingement arrays (at the LE) and out the film holes. Boundary conditions for the 1D flow network were the slot bottom supply pressure and temperature, and the airfoil external pressure distribution. The flow network provided input to the thermal model internal boundary conditions: passage HTC's were determined using correlations and the local flow network velocity. Correlations were also used to determine the heat transfer coefficients for surfaces that were impingement cooled. The resulting internal heat transfer coefficients applied to all of the internal cavity faces. For the blade external boundary conditions, the adiabatic gas temperature was modified to account for the film effectiveness of the film cooling holes. For the film effectiveness calculation, the film rows were simplified to lines that cover the same fraction of the span. The film effectiveness from upstream rows was added to downstream rows to establish a composite film effectiveness over the entire airfoil surface. As the thermal solution was iteratively solved, the exit temperature from each film row air node changed as the internal heat pickup varied, and this new film hole exit temperature was then used with the film effectiveness surface map and the adiabatic gas temperature to determine a local film temperature. A similar process was used to determine the airfoil external heat transfer coefficients. A cold-wind correction factor was applied downstream of each film row to account for the boundary layer re-energization caused by the coolant injection, and these factors were superimposed over the gas HTC maps to form a composite external map. Bore cooling effects from individual film holes were included by "drilling" through the thermal mesh (the physical film hole was not included in the geometry, rather, the effect of the flow through the hole was modeled with the drilling technique). First, an advection link was constructed for each film hole using its physical endpoint coordinates. Each advection link was then connected to the local metal elements using convective resistor links, and the heat pickup for the film hole modeled by determining an effective HTC (or resistance) for each link using correlations. The flow through the film holes created high HTC levels that showed up as localized peaks on the airfoil HTC surface map. All of the components of the thermal model (1D flow solver, boundary conditions and the conduction solver) were iterated until a converged solution was determined.

## *Blade Cooling Design Optimization*

Under this sub-task, a method has been developed to optimize blade cooling features and designs. The method was applicable to either sub-models or complete blade sections.

## *Internal Cooling Optimization Approach & Methodology*

A design of experiments (DOE) approach was selected to map the design space. Using DOE principles, a set of geometry and flow variables was determined. Thermal & thermal stress analyses were then performed on the DOE cases. Results from the DOE analyses were used to optimize the results. Initially, a response-surface optimization was used; the final design optimization used a neural network.

To support the DOE process, a news set of analysis tools had to be developed. The screening approach used fixed external conditions and fixed film hole locations and flows – these assumptions were too restrictive for the optimization procedure. The P/thermal coupled pseudo-3D analysis technique presented previously required extensive manual input for each case, which was unattractive for large DOE matrices. A new system was developed, using Ansys for both thermal and thermal stress analysis. The Ansys approach allowed the process to be scripted and largely automated, minimizing the time required to perform an optimization study. Initially, the script approach used several simplifications (such as fixed external boundary conditions), but, in its final form (documented below), the script was general, and accounted for coupled internal-external conditions, including bore cooling effects. Film locations and flows in the final script were completely arbitrary, allowing it to be used as a general design and optimization tool.

## *Optimization Method*

The analysis process was broken down into several steps, which were then automated. First was geometry generation: the Solidedge CAD package was used to construct parametric solid models of the blade section design of interest (approximately the center 20% of the blade). Values for variables were entered in tabular form, and the CAD package revised the geometry to the new parameters. The model cross-section surfaces were exported as iges files, which were then read into Ansys. A 3D mesh was created in the solid model section, and then extruded to form the thermal barrier coating (TBC) layer where appropriate (all cases used a partial wrap TBC). External boundary conditions were mapped to the outside of the TBC or metal volume – the current process uses the blade pitchline adiabatic wall temperature and HTC's (no radial variation) as a function of surface length from the stagnation point to define the external heat source. A spreadsheet adds the effects of film cooling to the external source profiles: film curves provide a distribution of film effectiveness versus surface length (along with cold-wind correction factors for HTC's), and the film effectiveness values for all of the film rows were then superimposed to generate the final external boundary conditions. The spreadsheet provides the external boundary conditions as table data for the Ansys models. By using the spreadsheet approach, the locations and layout of the film rows can be included as part of the optimization process. An internal flow network for the current design supplies data for HTC correlations on the interior surfaces (the flow network was re-run for each case, to account for any changes in the cooling chamber geometry). The Ansys model also includes an advection network, to track coolant air temperature changes in the thermal analysis. The advection network estimated the heat pickup that would occur in a full height blade by copying the temperature change across the model section (which was 20% of the blade height) to simulate the remainder of the blade. For example, for a serpentine passage, the pitchline model would have two chambers: the up-pass and the down-pass. The advection network temperatures were iteratively solved for by assuming that the blade had five identical sections hub-to-tip, so the air temperature in the up-pass chamber was set to the supply temperature plus twice the up-pass delta-T, and the down-pass air temperature was set to five times the up-pass temperature plus two times the down-pass temperature. It was assumed that there was no radial flow in the impingement and cross-over chambers.

A script was written to perform all of the Ansys functions (mesh generation, boundary condition tagging and application, advection network setup and connectivity, thermal solution and thermal-stress solution), to minimize the amount of user interaction during optimization runs. The script included error trapping and resolution to correct meshing difficulties with some of the DOE geometry variants. A flow chart describing the complete approach in more detail is presented below.

### *Optimization Method for a Complete Blade Pitchline Section*

The first step in optimizing the complete blade section was to update the Ansys script to include all of the geometry features and flow networks for the entire section. The approach taken to the section optimization was similar to the method used for the mid-circuit optimization (figure 4.2.2.5). Experience with the design screening effort and mid-circuit optimization yielded a 13 factor DOE matrix, which required 33 different runs to complete. Automation of the run setup and analysis was very important, so after Minitab was run to develop the matrix, a spreadsheet was developed to control all of the data required for each of the different runs. From the DOE matrix variables, the spreadsheet output a 1D flow network input deck, and the 1D flow solution returned aero data for each of the cooling passages to the spreadsheet. The spreadsheet also output a tabular set of geometry variables, which was read into the Solidedge CAD program and a section geometry generated (3D solid output as iges surfaces). The spreadsheet also contained the film row location information, which was output to a second spreadsheet, which integrated the external gas conditions with the film information and output the external boundary conditions for the Ansys model. Finally, the spreadsheet output a set of input data for the Ansys thermal analysis script, which was combined with the external boundary conditions and geometry file to run the script. The script then meshes the section geometry (20% of the blade height), extrudes and meshes the TBC layer, sets up and associates the advection network, tags the internal and external boundary conditions, runs the thermal analysis and then runs a thermal stress analysis. The script does not include the effects of bore cooling on metal temperatures, and does not iterate with the film temperatures (these items were added in the final script).

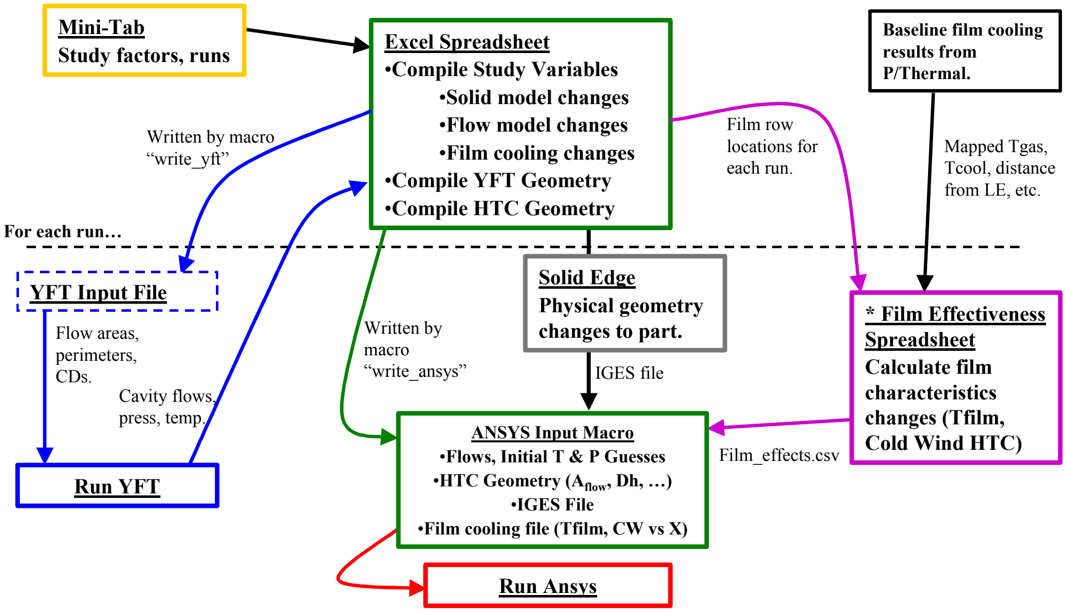

**Figure 4.2.2.5: Pitchline section optimization methodology (DOE optimization).**

The geometry factors for the DOE optimization required some experimentation to determine allowable ranges to create realistic geometries. The geometries for the 33 DOE cases were created, and the thermal / thermal stress analyses completed using the Ansys-based script.

One of the objectives of this study was to incorporate the impact of thermal stresses in the design process (previous studies had focused on bulk metal temperature as the measure of cooling effectiveness), so three optimization studies were completed. The first optimized the geometry attempting to minimize both Tbulk and maximum thermal stress; the second optimized to Tbulk alone, and the final case optimized to max thermal stress alone. Optimizing to both Tbulk and stress provided an improved bulk temperature level over the nominal case, and a max stress that was close to the result for the stress-only optimization (a ~10% reduction over the nominal case).

### *Neural Network Optimization*

To increase the robustness of the optimization procedure, the initial response surface methodology was replaced with a neural network process (figure 4.2.2.6). Using the limited results from the previously completed DOE matrix, the neural network optimization process optimized to a slightly different geometry than the response surface output. The neural network model provided slight improvements in bulk temperature and thermal stresses over the response surface results. The optimization space was limited in this initial study, so the neural network process was not expected to show significant differences from the response surface, but for larger scale, more complex design spaces (using the latest analysis script), the neural network optimization process should be more robust in finding the best solution than the response surface approach.

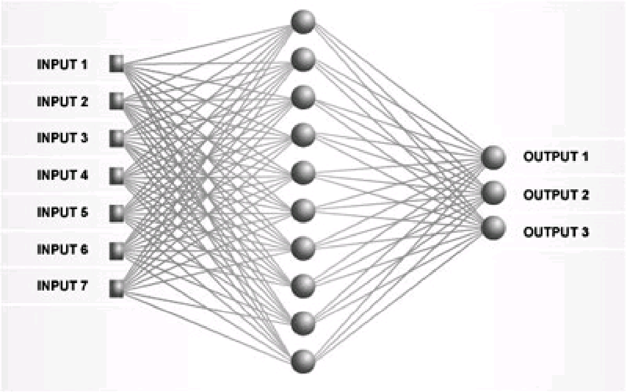

**Neural Network Characteristics**

- **13 Input Parameters**
- **2 Output Variables**
  - Max Stress
  - Tbulk
- **2 Hidden Layers**
  - 1st Layer
    - **Hyperbolic tangent sigmoid Transfer Function**
    - **10 Neurons**
  - 2nd Layer
    - **Linear Transfer Function**
    - **1 Neuron**

**Figure 4.2.2.6: Neural network optimization parameters.**

## *Including Bore Cooling in the Thermal Analysis Results*

Bore cooling effects can significantly affect the thermal response of the blade, so the Ansys-based analysis script was updated to include those effects. To provide an estimate of the bore cooling effects without having to design and map every filmhole, a simplified approach was developed. The pitchline cooling hole vectors (in terms of their Z-theta orientation) were constructed as lines in the CAD software as the model was being assembled. These line data were then output to the Ansys script, which used the “path” function to select a set of representative elements in the model. Correlations were used to estimate the heat extracted by the flow through the filmholes, and this heat was then extracted from the elements along the path. The source film temperature was also raised to maintain the energy balance in the model. At the same time as the bore cooling functionality was added, the script was modified to include an estimate of the trailing edge cooling slot effects, so the TE model should be more representative of the blade geometry. The final script contains all of the pieces required for non-traditional blade cooling design: arbitrary geometry inputs; internal heat pickup and correlations; film hole bore cooling; and coupled external film prediction. The process chart for the final script (figure 4.2.2.7) shows the steps required to include all of these items.

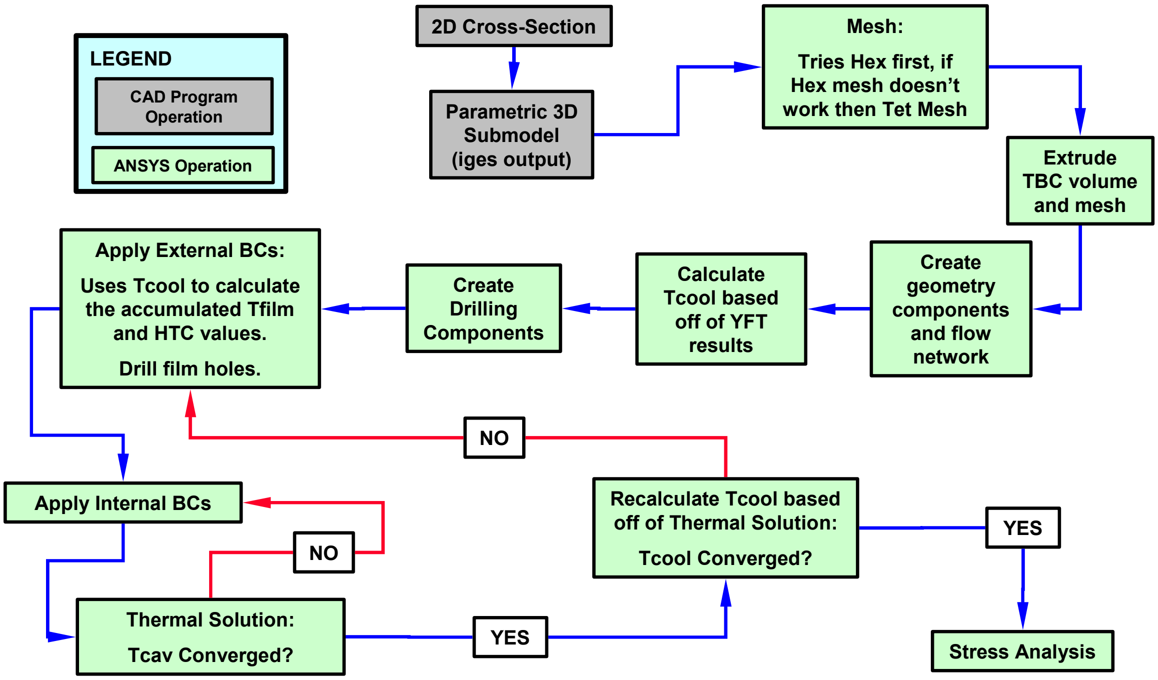

**Figure 4.2.2.7: Final Ansys-based thermal / thermal-stress blade pitchline analysis script flowchart.**

## ***Blade Modeling Summary***

The objective for the blade modeling task was to develop an advanced blade cooling design that would allow the blade to be sufficiently cooled with a ten percent reduction in cooling air. To accomplish that goal, several steps had to be taken. The first was to develop a method to screen through new concepts to identify designs that had the potential to meet that goal. A more detailed design system was then constructed that interfaced with optimization routines to provide further system performance improvements. The design work was mainly done on a pitchline section, so a method was established to build full 3D blade geometries with arbitrary cooling architectures (including the shank and supply plumbing), and an advanced cooling design was developed. An existing 3D thermal analysis tool was modified to handle the non-traditional design of the advanced blade, and the metal temperatures were compared to a traditional serpentine-passage-cooled blade. The results found that the advanced design was successful in matching the traditional blade cooling effectiveness with ten percent less cooling flow. The advanced design featured several flow circuits that were outside of the current design practice for turbine blade cooling, so to verify that they would perform as intended, a combined computational – experimental program was undertaken. Both the CFD analysis and the detailed flow visualization from the experiments demonstrated that the advanced design circuits functioned as designed. The 3D thermal and flow visualization results were evidence that the advanced turbine blade cooling system developed under this program was successful in generating an improved blade design.

## *Section 4.2.2 List of Figures*

### 4.2.3 Advanced Blade Mechanical Stress / Life Modeling (GE Aviation)

A basic mechanical assessment has been done of one advanced cooling concept blade. ASE Technologies created a 3D solid model of the blade from a preliminary solid model of the base serpentine blade and shank. Therefore, the model for the advanced cooling concept blade is externally identical to the base blade model, which enables a direct comparison of results between the two. It should be noted that the base serpentine blade used here was an early design iteration with a rather preliminary shank design. This was also the first pass at integrating the new cooling concept into blade and shank. The results should therefore be taken strictly on a relative basis.

In summary, the first cut at incorporating the advanced concept into a 3D blade model has shown us areas that need to be worked, but has not revealed any serious obstacles to a viable mechanical design.

### 4.2.4 3D UG-Based Flow Network Model

**Background**

GE's current cooled turbine thermal design system supports the generation of coupled heat transfer and 1D cooling flow models and analyses for conventional serpentine designs. Advanced designs outside the scope of our design system require a large investment in manual work to build and analyze models. Required for this model generation are both the geometry of the parts and the topology and geometry of the flow channels. There are commercial tools available for building the part geometry (Unigraphics, SolidWorks, ProEngineer), but not so for the flow networks (at least not in the same geometry modeling environment).

**Objectives**

The objective of this task was to demonstrate the feasibility of using UG (Unigraphics) as a base environment, enhanced by a set of tools, to build topology, geometry, and associated flow attributes of 1D flow networks in the context of the UG models of the cooled turbine parts. This allows the flow network to be visualized along with the surface geometry of the actual part for consistency. Further, geometric data can be computed from the surface geometry that is relevant to the flow network, such as flow areas and perimeters. Having built the flow network models in UG, the toolset will be able to create files which will make this flow network properties available to build 1D flow models in design tools like YFT (1D flow network solver) and pThermal (coupled FEM thermal solver coupled to YFT network flow solver).

**Technical Approach**

Flow networks are fundamentally represented by flow nodes and flow elements. We represent this in UG using points with the attribute called NODE to model flow nodes. Flow elements establish the topology of the network. UG cylinders were chosen to represent flow elements for ease of visualization in the UG 3D graphics display. Cylinders used as flow connectors are tagged with the attribute named "CONNECTOR". Attributes required to build flow networks (cross sectional area, discharge coefficients Cd, perimeter, tags to associate flow elements with geometry surfaces) are stored either on the NODES or CONNECTORS. Operators are available to the user to assign values to these attributes. Other operators are available to automatically compute quantities such as area and perimeter from the connectors and the part surface geometry.

**Results**

Figure 4.2.4.1 shows a 4 cavity simple airfoil with a flow network constructed in the context of the UG surface model of the airfoil cooling cavities.

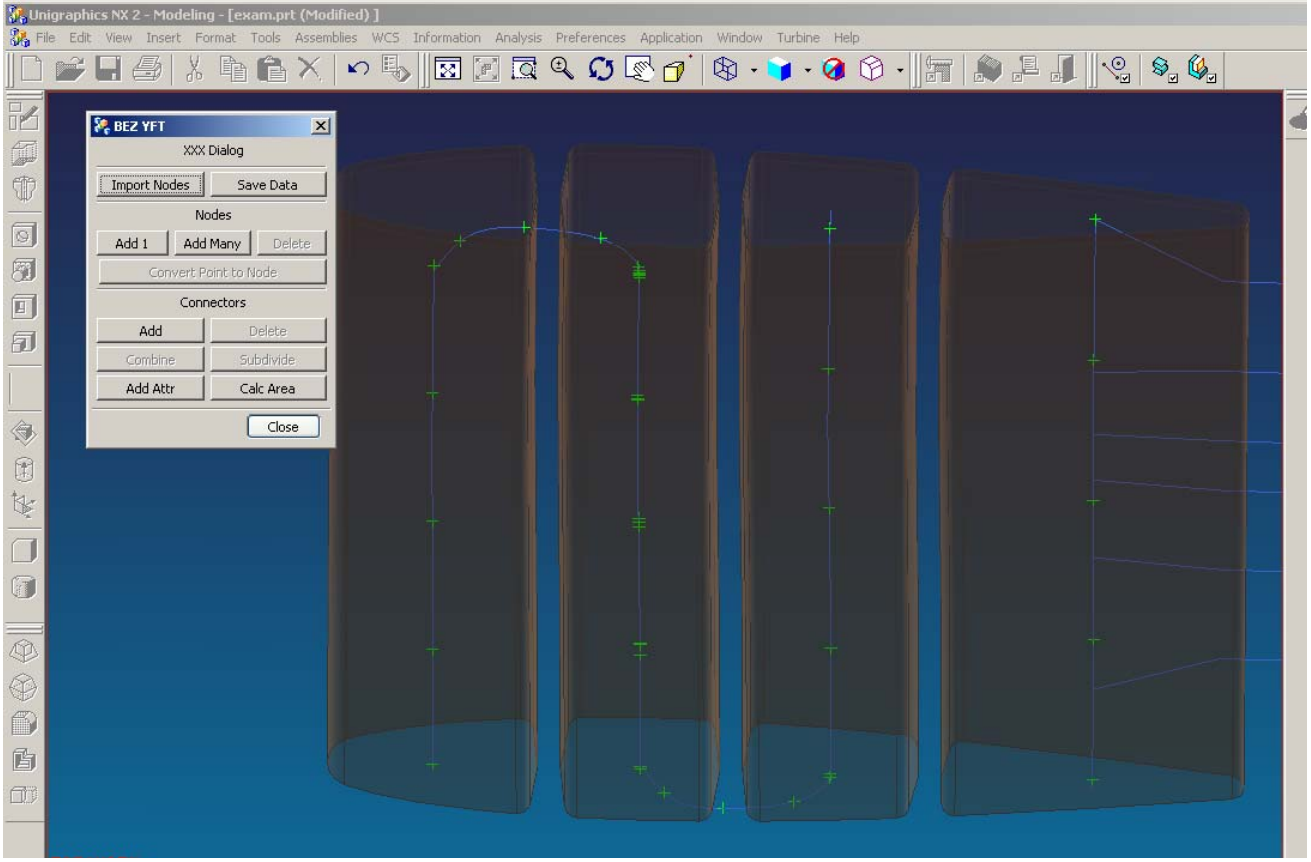

Figure 4.2.4.1 UG based flow network editing GUI

Operators are available to create flow nodes from points, to create connectors between flow nodes, to compute cross sectional areas and perimeters from a set of surfaces which surround a connector, and to create a set of flow nodes and connectors which follow the center of gravity of a set of surfaces which might represent a cavity. This tool set can be used to define arbitrary cooling networks in UG. With the extension to create a method to write out the geometry and attributes to text files (not yet implemented), data is available to build the analysis models that have previously had to have been built manually in prototyping the advanced cooling designs considered in other tasks of this work.

## **Conclusions**

The design structure developed, along with prototype tool set implementation, demonstrates the feasibility of a UG based approach to building 1D flow networks in the context of the UG models of cooled turbine blades (or any other aircraft engine component for that matter). The flow network models can be saved with the UG part file for reuse and archival with the product life cycle management system. This also opens the door for the standard design process for conventional designs to create these flow network structures in the conventional design UG Master Models.

Given UG models for advanced cooling designs, and the ability to define associated flow networks in UG with appropriate attribute data, we can accelerate the process of building the required data to build yft and pThermal analysis models both more accurately and more quickly. UG provides the visualization to validate the correct geometric orientation and layout of the material surfaces and flow network so the models meet the design intent. Tools which compute cross sectional areas and perimeters will take much less time than manual processes and produce more accurate results.

Building the flow networks as geometry with attributes is much like building geometry for the parts. The part geometry can then be meshed to varying levels of resolution. Similarly, by building geometric models of the flow network, it can also be meshed to 1D flow networks at varying levels of resolution.

### 4.2.5 Cooled Cooling Air Thermal Management System

**Air-Air Heat Exchanger System**

A preliminary thermal / mechanical design was developed for a dedicated Cooled Cooling Air (CCA) Thermal Management System (TMS). The intent of the TMS is to cool a small amount of compressor discharge (CD) air, remix it with another portion of W25 CDP air, and use this mixed air to reduce the overall cooling air flow to the high pressure turbine (HPT) blade. The system performance was analyzed and shown to produce the target cooling flow temperature reduction with a reasonable system weight.

### 4.2.6 Fluidic Flow Control and Film Cooling

#### Overall Objective

Investigations were conducted on cooling flow control based on methods such as fluidics and active flow area control. Proof-of-concept test were performed for selected concepts.

This subtask supported the development of concepts associated with active flow control by conducting analysis and tests at the GE Transportation-Aircraft Engine's (GET-AE) Heat Transfer Laboratory test facility in Evendale, Ohio. Three test programs were run. The first test investigated the use of pulsed vortex jets to improve the film cooling performance at low-external flow Mach number regions on the pressure-side of a turbine blade. The second test investigating the use of pulsed vortex jets to improve the cooling performance of trailing edge slots. The third program obtained flow data from a vortex valve designed to adjust the cooling flow supplied to the high pressure turbine blade during engine operation, increasing the flow during portions of the flight mission such as takeoff and climb when cooling is critical and decreasing the flow during cruise when performance is critical

#### Test Program 1 – Pulsed Vortex Jet Generators in Discrete Hole Film Cooling Applications

#### Objective

The forward half of modern, highly-loaded high pressure turbine blades are difficult to cool using film cooling for two reasons: 1) it is difficult to drill shallow film holes having a shallow surface angle ($25^o$ to $30^o$) into the blades due to the extremely small width of the internal cooling passage on the pressure side of the blade and 2) the axial component of the mass flux passing over the external surface is small, producing high blowing ratios as the film coolant is injected into the mainstream. The larger-than-desired surface angle and the high blowing ratio both promote blowoff of the film cooling flow, allowing the coolant to detach from the surface being cooled and more freely mix with the mainstream flow. This results in lower-than-desired film cooling effectiveness along the surface.

The first test program was run to determine whether pulsed vortex generator devices can successfully reduce the total pressure of the cooling flow exiting a film hole and reduce or eliminate blow off of the cooling film.

#### Approach

Film cooling tests were run on four film hole geometries. Sketches of the first three film holes are shown in Figure 4.2.6.1.

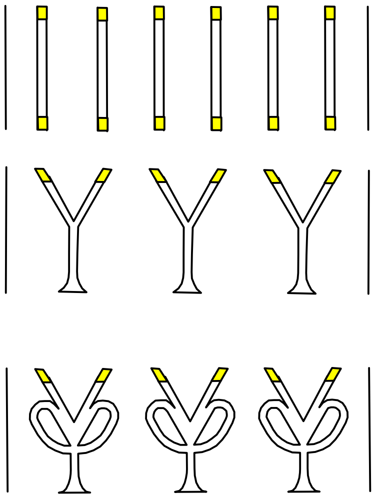

- Axial Hole – Both Square and Round Axial Holes Tested
- “Y” hole – similar to “X” and “V” holes tested in early 1990’s
- Pulsed Jet Vortex Hole

Figure 4.2.6.1 Discrete Film Hole Geometries

Configuration 1 is the baseline hole configuration; an axial hole inclined $30^o$ from the surface and oriented inline with the mainstream flow. Configuration 2 is a “Y” hole: a hole having a single inlet that then splits to form two exits. This hole was fabricated in a plane that was angled $30^o$ to the surface. Configuration 3 has a similar “Y” pattern plus the addition of two feedback loops to make it a pulsed vortex generator. This hole was also fabricated in a plane that was angled $30^o$ to the surface.

Each of the three hole configurations had the same hole cross-section and hole spacing. For fabrication simplicity, the cross-section of the hole was square. The holes were machined into an angled surface using an 0.0625 inch end mill and the machined surface was then glued to another angled surface. The resulting hole cross-section was an 0.0625 inch square, equivalent in flow area to an 0.0705 inch diameter round hole. The spacing between holes was 0.5 inches and the hole spacing-to-equivalent round hole diameter ratio was 7.09. This spacing ratio is consistent with the ratios used in gas turbine engine design, which can range from a low of three to a high in excess of ten.

A fourth test configuration was also fabricated and tested. This configuration consisted of axial round holes of diameter 0.070 inches inclined $30^o$ to the surface and spaced 0.5 inches apart, making it essentially equivalent to Configuration 1.

Each of the film hole configurations was installed in the test model shown in Figure 4.2.6.2. Mainstream flow entered the test model from the mainstream plenum through a round bellmouth and passed through a duct measuring 3 inches wide by 2 inches tall. The film hole configuration was installed on one wall of this duct. A film cooling plenum supplied cooling to the holes.

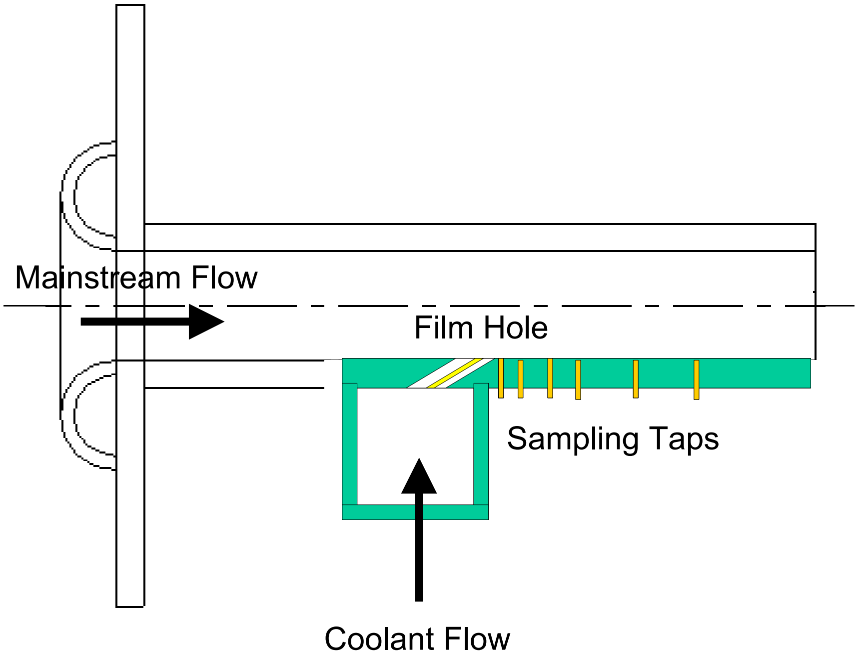

Figure 4.2.6.2 Discrete Hole Film Cooling Test Model

Film cooling tests will be run on these models using a gas analysis technique, the mass transfer analogy to the thermal 3-temperature film cooling condition. In this technique, the coolant consists in entirety or in part of a foreign gas. The film cooling effectiveness is determined from gas concentration measurements made along the wall of the test model downstream of the coolant injection. This method is valid because the differential equation that describes the mass diffusion process is virtually identical to the differential equation that describes the thermal diffusion process, the only difference being a single term in the equation where the thermal diffusion process has a ratio of turbulent Prandtl number to Prandtl number and the mass diffusion process has a ratio of turbulent Schmidt number to Schmidt number. Various researchers, foremost among them the University of Minnesota, have demonstrated that the gas analysis method produces reasonably accurate film cooling measurements over a wide range of Schmidt numbers. GE-Aviation has also validated the gas analysis technique against the results from a number of thermal film cooling tests.

The foreign gas used in the current tests was pure carbon dioxide, which produces a nominal coolant-to-mainstream density ratio of 1.52. This level is near the middle of the 1.4-to-1.6 range experienced during the film cooling of high pressure turbine blades during engine operation. Wall taps installed at various locations on the film-cooled wall were used to extract gas samples and the samples were then passed through a carbon dioxide analyzer to obtain the concentration of the foreign gas at each location. The film cooling effectiveness was then obtained from the equation

$$\eta = \frac{C_{mainstream} - C_{wall}}{C_{mainstream} - C_{coolant}}$$

where $C_{mainstream}$ is the mass concentration of the foreign gas in the mainstream flow, $C_{coolant}$ is the mass concentration of the gas in the coolant and $C_{wall}$ is the mass concentration of the gas measured along the wall. In the current tests, $C_{mainstream}$ was zero and $C_{coolant}$ was essentially unity.

The gas samples were read by bleeding off a portion of mainstream flow through a wall tap until a steady-state concentration reading was obtained. The samples were taken individually and the bleed rates regulated so that they were less than 10% of the mainstream velocity. This bleed rate is the level recommended by researchers at the University of Minnesota to produce acceptable measurement accuracy, a claim that has been validated in previous tests at GE Aviation.

## Results

GE Proprietary details about the test, including dimensional information on each of the film hole test configurations and tabulated results, may be obtained from the author.

## Summary/Conclusions

The improvement in cooling performance generated by the PVJ hole in the near-hole region is not large enough to excite cooling designers, especially in light of the difficult casting requirements for that hole. For this reason, no additional tests were run

## Test Program 2 – Use of Pulsed Vortex Jet Generators in Pressure-Side Bleed Film Cooling Applications

## Objective

The second test program investigated the pulsed vortex jet in a pressure-side bleed (PSB) slot application. PSB slots are the film cooling slots located along the trailing edge of turbine blades and vanes. The film cooling effectiveness obtained on the floor of these slots is usually equal to unity from the slot breakout until about halfway to the trailing edge. The effectiveness then decays significantly from that point to the trailing edge. The lower film effectiveness level at the trailing edge is the main reason why the trailing edge metal temperature is usually the hottest temperature on an airfoil. Numerical simulations of the pressure-side bleed slot film cooling flows generated using steady-state computational fluid dynamics (CFD) do not agree with the results obtained in PSB model tests and in engine applications, but instead predict that the film cooling effectiveness will remain at or near unity from the slot breakout to the trailing edge. Unsteady CFD simulations, however, predict that are much closer to the effectiveness levels observed in tests and in the engine. This suggests that the PSB film coolant flow field is unsteady and this conclusion has been supported by unsteady pressure measurements made on a PSB test model by the GET-AE Heat Transfer Lab. Film cooling results obtained at the GET-AE Heat Transfer Lab and plotted as a function of the blowing ratio ***m*** also indicate presence of a local minimum, i.e., the film cooling effectiveness measured on the floor of the slot near the trailing edge first rises with ***m***, then peaks, falls to a valley and then resumes rising. The minimum point has been shown to occur near a coolant-to-mainstream velocity ratio of one. One hypothesis of the cause of the minimum is that the mainstream and coolant flows are both unsteady and that the minimum occurs when the unsteadiness in both flows have the same forcing frequency and are in sync with each other. For simple Strouhal number wake shedding, this would occur at a velocity ratio of unity. If the hypothesis is valid, then we may be able to improve the PSB film cooling performance by modifying either the mainstream or coolant forcing frequencies. The objective of this test program was to see if was possible to improve the PSB film cooling effectiveness by modifying the coolant forcing function with the pulsed vortex jet.

## Approach

The pressure-side bleed tests also used an existing GE Aviation test model. A sketch of the test model is shown in Figure 4.2.6.3. The model's mainstream flow path consisted of a bellmouth inlet followed by a short straight mainstream duct. A constricting nozzle block was mounted on the top wall of the duct near the duct exit to match the pressure distribution present near the trailing edge of a blade during engine operation. The nozzle block was designed using one-dimensional isentropic compressible flow theory.

In all of the configurations, the floor/bottom wall of the slots was angled to meet the mainstream duct at the exit of the test model. The top of the lands extending downstream of the breakout that separated the slots was tapered to contour with the bottom wall of the mainstream duct. The duct bottom wall, the lands which defined the slots and the slot bottom wall were assembled together into a single component and could be removed from the rest of the test model and replaced with a similarly constructed component representing a different film slot geometry.

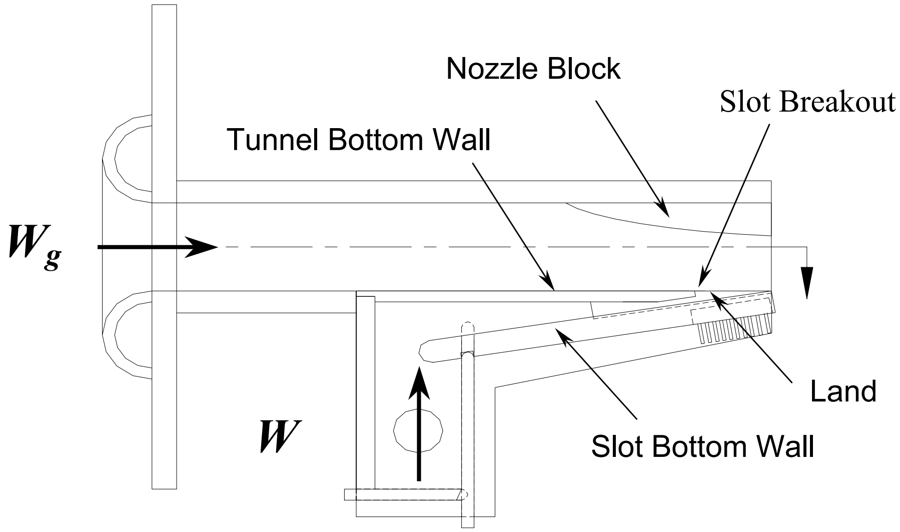

Figure 4.2.6.3 Cross-Section View of Test Model Used in Pressure-Side Bleed Film Cooling Test

Previous PSB tests run at GE-Aviation have been run on a nominal 10X scale model of the engine geometry. In all cases until now, the test modeled three PSB slots and all film cooling measurements were taken in the center slot and on the neighboring lands that separated the slot from the side slots. Modeling PVJ slots will require a test model having an even number of slots. Therefore, a new baseline slot configuration (Configuration 1) having four slots and representing nominal 7.5X engine geometry was fabricated.

Two additional PSB slots were tested. The second configuration was a Y slot and the third configuration was a PVJ slot. Both slots have one inlet and two exits and had the same slot exit area and land geometry downstream of the slot breakout as the baseline slot. The PVJ slot also a two fluidic feedback loops. The feedback loops are intended to divert a portion of the slot flow back and forth between the two exits.

The film cooling effectiveness in the PSB tests was measured using the gas analysis method described in the previous section. Instrumentation taps were installed in each of the test models at six difference spanwise locations: 1) the slot centerline, 2) midway between the slot centerline and the slot edge, 3) the slot edge, 4) the side of the lands, 5) the edge of the top of the lands and 6) the land centerline.

**Results**

GE Proprietary details about the test, including dimensional information on each of the pressure side bleed test configurations and tabulated results, may be obtained from the author.

### Summary/Conclusions

The Y slot produced better film cooling effectiveness on the side and top of the lands than the baseline slot, but at a price of decreased performance on the slot floor. The resulting area-weighted average of the slot, land side and land top results for the three slots were nominally equivalent, with the Y slot being slightly superior to the other two slots for X/S < 9 and the baseline being superior for X/S > 9.

The Y slot and PVJ slots did not significantly improve the pressure-side bleed film cooling performance over the baseline slot. This, coupled with the additional casting complexity of the PVJ slot, helped terminate the test program after the completion of the three tests.

## Test Program 3 – Use of a Vortex Valve to Control Cooling Flow During Engine Operation

### Objective

An aircraft engine experiences different conditions during its flight mission. During takeoff and climb, the engine is generating the most power and its hot section parts, especially in the high-pressure turbine, are experiencing the most severe thermal conditions. The mainstream temperature and flow is at its maximum level and the cooling flow temperature also is at its maximum level. Later, during the cruise part of the mission at high altitude, the temperature and flow levels are lower, reducing the heat flux through the hot section components. Historically, the cooling flow delivery to the high-pressure turbine rotor has been sized for the severe takeoff and climb conditions. This flow level is usually much higher than required to cool the turbine at the cruise condition. This reduces the engine’s efficiency during the performance-critical cruise portion of the mission. Previous efforts to introduce valves to control the cooling flow delivered to the HP turbine have not succeeded because of the mechanical complexity of the proposed system -- the design community is very reluctant to rely on mechanical-actuated components on a mission-critical part of the design such as the HP turbine cooling flow.

A new control valve has been proposed that does not rely on mechanically actuated components. Instead, the valve design is static, i.e., it does not have any moving parts. The flow through the valve is controlled in two ways: 1) the relative difference in thermal growth of valve components fabricated from different materials and 2) a vortex swirl introduced inside the valve to lower the pressure leaving the valve.

A test program was run to obtain flow data to support the design of the new vortex valve.

## Approach

A sketch of the test model used in the test is shown in Figure 4.2.6.4. The test model did not directly model the thermal growth attributes of the proposed design, but permitted testing of the thermal growth effect through the insertion of washers between the adjustable piston and the fixed shaft at the centerline of the valve. The flow through the valve is partially controlled by changes in flow area caused by shifting of the adjustable piston. Additional control is provided by a swirl vortex produced by a pair of swirl jets introduced at $180^{\circ}$ opposing locations in the gap between the piston and the outer wall of the valve.

Flow was introduced into the test model through the ports indicated on the left side of Figure 4.2.6.4 and exited out of the single port on the right side of the model. A portion of the flow is bled out of the plenum and reintroduced through two swirl jets inside the model, simulating the proposed engine application. Additional tests were run with an independent swirl jet supply. Pressure measurements were taken at a number of locations inside the model.

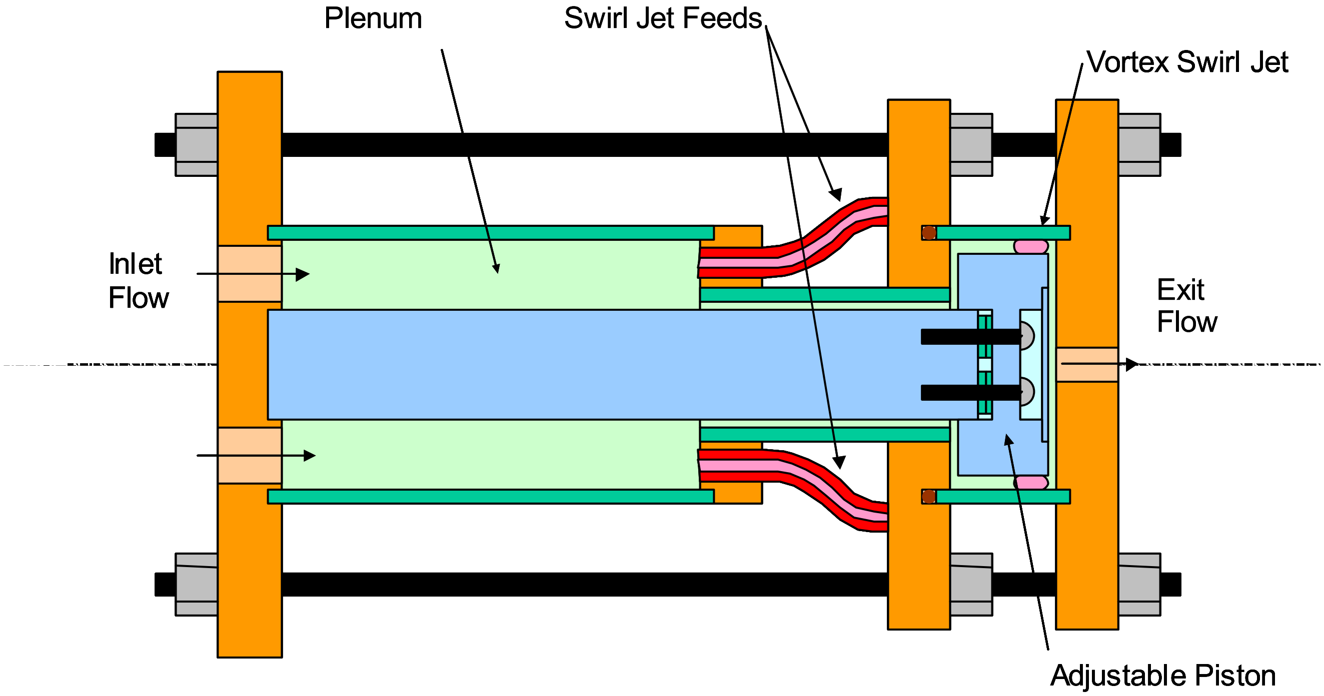

Figure 4.2.6.4 Sketch of Cross-Section of Vortex Valve

## Results

Additional GE Proprietary details about the test, including dimensional information about the design of the vortex valve and tabulated flow and pressure results, may be obtained from the author.

## Summary/Conclusions

A test was run to get flow and pressure data on a vortex valve designed to control the cooling flow supplied to the high-pressure turbine rotor.

## Overall Summary/Conclusions

Three test programs were run to investigate the potential use of fluidic and active flow control devices in the cooling design of the gas turbine engine. A film-cooling test investigating the use of Y holes and pulsed vortex jet (PVJ) holes on the forward half of the pressure-side of a highly loaded turbine blade where intrinsically high blowing ratios promote blow off indicated that at best the benefit that they would provide was small. A second film test investigating the use of Y slots and PVJ slots to improve the film cooling performance of pressure-side bleed slots at the trailing edge of a turbine airfoil also showed little if any benefit compared to the baseline slot. In both cases, the PVJ hole/slot also may be difficult to fabricate. Finally flow and pressure data were obtained on a vortex valve intended to control the cooling flow delivered to the turbine rotor at different periods during the fight mission. This proposed design shows promise.

## List of Figures

### 4.2.7 Active Component Cooling Development Tests (GE Global Research)

GEGR conducted several bench-scale tests of potential actively cooled components to support the individual cooling technology features developed under GE Aviation task 4.2.1. These included: 1) directed jets (swirl flow) into an internal cooling cavity to increase overall heat transfer coefficient and reduce wall thermal gradients, 2) alteration of the trailing edge slot hole geometry to reduce heat loading on the trailing edge slot floor, and 3) pulsed jet impingement to explore the entitlement of unsteady impingement heat transfer that might be obtained with controlled flow devices, such as fluidic oscillators. The purpose of these tests was to prove the concepts and to explore the operating envelopes and entitlements. Details of these efforts are given below.

#### 4.2.7.1. Swirl Flow Development Tests

The objective of the present work is to explore the effect of the swirl flow cooling and compare it against impingement cooling flow, in other words, is to investigate the effect of jet position, jet angle, and swirl cavity shape on enhancing the forced convection heat transfer inside internal cavity.

One basic type of directed-impingement jet configuration was explored under previous Propulsion 21 funding. In these tests, 20 jet holes equally spaced were aligned in a row along the side of a tube at an angle of 30-degrees tangent to the tube surface. The tube was closed at one end and opened at the other. Cooling air was blown through the 20 jet holes into the tube creating a swirling flow enhancing the heat transfer on the inner surface of the tube. Electrical heaters were used to provide a constant heat flux boundary condition on the internal surface of the cylinder, and the applied heat flux was used with thermocouple temperature measurements of the surface and the air to provide measures of average heat transfer coefficient for different airflow rates. These results were compared to a base case of airflow straight through the tube. An enhancement of was observed over the range of flow rates tested. The swirl chamber test apparatus from the previous effort is shown in Figs. 4.2.7.1.1(a), (c), and (d).

In order to provide a more applicable and appropriate baseline for establishing the degree of heat transfer enhancement for directed-impingement jets compared to traditional impinging jets, and to further provide validation data for CFD models, another test has been completed. The test was performed in the same experimental rig used previously. In this test, the jets were oriented normal to the tube surface, as opposed to 30 degrees from tangent, to represent traditional cross-over hole jets impinging on the far wall of a turbine blade leading-edge passage without inducing a consistent swirl. This configuration is depicted in Fig. 4.2.7.1.1(b).

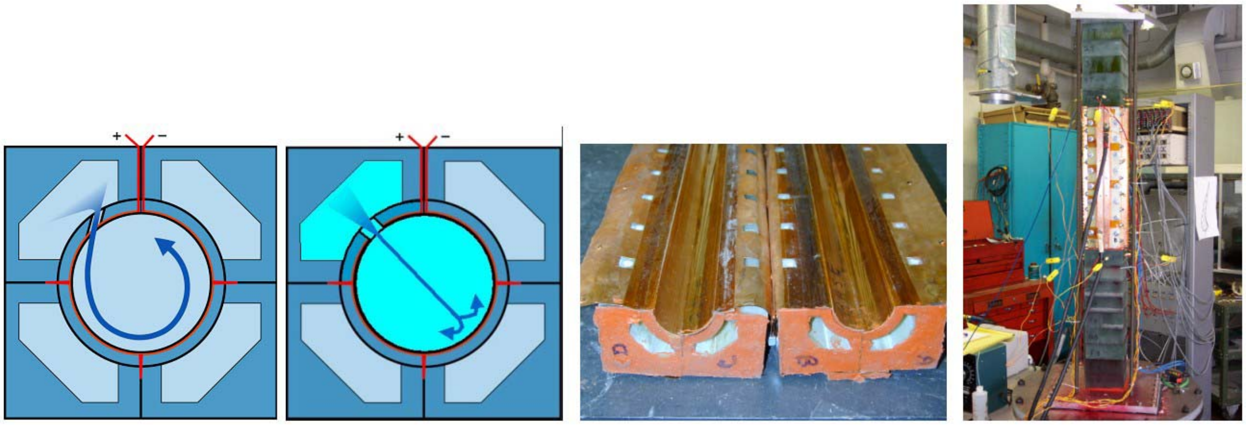

(a) (b) (c) (d)

Figure 4.2.7.1.1 (a) A cross-sectional diagram of the swirl chamber test section showing the center test chamber and four side plenum chambers. A swirl jet is depicted as entering the test chamber from the top left side plenum chamber. The red line depicts the path of the foil heater circuit around the center test chamber. (b) The same cross-section showing a normal-oriented jet. (c) A photograph of a test chamber split in two, with the two halves lying side-by-side. (d) A photograph of the experimental apparatus mounted on the testbed plenum before wrapping with a thermally insulating blanket.

The results show that, for same Reynolds number based on channel diameter, the swirl jets provide better cooling than the normal jets. The strong generated tornado inside the hot chamber will increase the average velocity near the wall, increasing convective heat transfer. It should be noted that the normal jet will produce higher local heat transfer coefficients at the point of impingement, and therefore may reduce the temperature in that particular spot, while the swirl flow will provides a more distributed or diffuse effect, potentially reducing thermal gradients in the wall.

It is believed that a better understanding of swirl flow will lead to designs with better cooling (higher average heat transfer coefficient), allowing for lower temperatures and thermal gradients in the metal wall, or allowing for a reduction in required cooling flow while maintaining the same cooling thermal protection. The experimental effort was therefore expanded to include the other test rig shown in Fig. 4.2.7.1.2, with the test cavity configurations shown in Fig. 4.2.7.1.3.

In these tests, 5 jet holes equally spaced where aligned in a row normal to a flat plate. The flat plate was used to hold the swirl cavities shown in Fig. 4.2.7.1.3. By controlling the cavity location, one can generate swirl flow and direct impingement flow.

These tests are being performed using clear acrylic models with a liquid crystal temperature diagnostic technique that enables measurement of the local temperature, and therefore local heat transfer coefficient, over the internal chamber surface. In all these cases the flow is introduced into the swirl cavity through the jets and allowed to exhaust out of the two open ends.

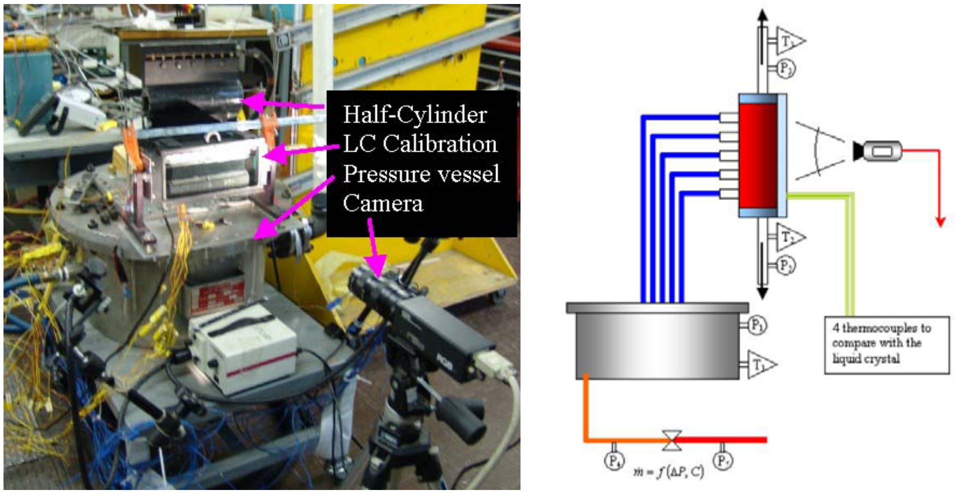

(a) (b)

(b)

Figure 4.2.7.1.2 (a) Current test setup for the three different chamber configurations under investigation. This picture shows the half-cylinder chamber, the calibration device for the liquid crystal, the camera used to capture the liquid crystal pictures, the pressure vessel, pressure gages, and thermocouples. (b) Schematic diagram of the test setup.

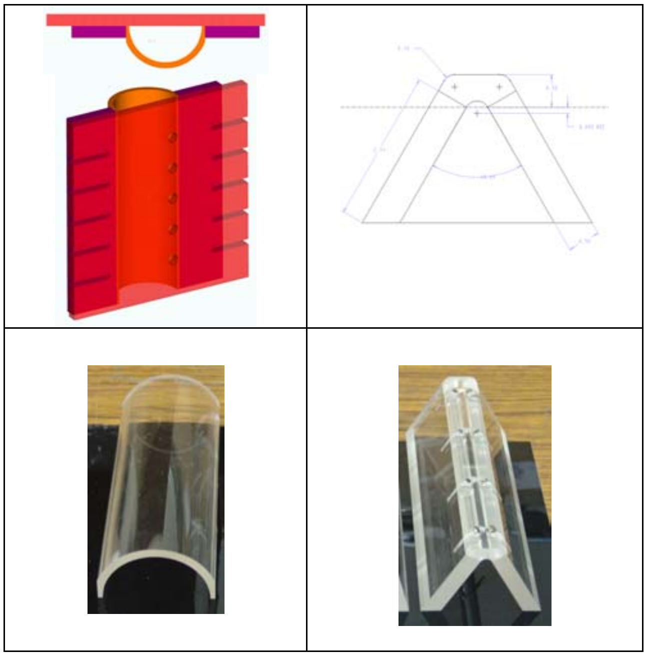

Figure 4.2.7.1.3 The two different test configurations being explored to enable better understanding of the swirl jet flow. (a) Half-circle cavity was mounted to 5 jets flat plate structure. (b) 60-degree triangle mounted to 5 jets flat plate structure.

The location of the cavity will be used to generate the swirl and direct impingement flow. Thin electric heater sheet was used to generate uniform heat flux at the wall cavity.
Internal surface of the swirl cavity was covered by three layers consist of one adhesive sheets, one liquid crystal sheet, one thin electric heater sheet, as show in Fig 4.2.7.1.4.

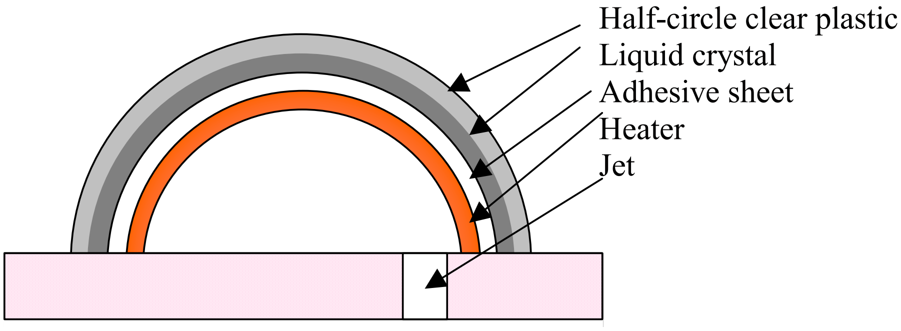

Figure 4.2.7.1.4: Cross section of the assembled heater, liquid crystal, and adhesive sheets

For the half-circle swirl cavity different airflow rate were used to compare swirl and impingement jet flow. For each flow rates, around 8-14 heat loads are used to generate same amount of colored thermal liquid crystal images. These images were processed using MathCAD program that was developed in GRC. The images were captured using digital camera with (320x240) pixel resolution. The camera, the image processor, the light setting, and thermal liquid crystal were calibrated with thermocouples and an assumed second order relation between each thermocouple, as show in Fig 4.2.7.1.5. The calibrated thermocouple uncertainty was found to be ~$2^0$ F. In order to generate the Temperature-Hue curve, the temperature at different locations was measured using thermocouples and was plotted in the x-axis. The corresponding Hue value plotted in the y-axis was calculated using a monotonic tangent inverse relation that depends on the measure RGB values. The colored image was captured using the digital camera. The uncertainty of camera was assumed very small which will not affect the measured RGB values and hence the calculated Hue value. In order to reduce the uncertainty of measured data, one should keep the test light intensity, saturation, and angle the same through the calibration and the experiments; otherwise a calibration curve is needed for each test. Keeping this in mind, calibration was done once for random selected thermal liquid crystal sheet and that calibration curve was used to analyze the presented data.

The presented data analysis was corrected for heat loss and optical distortion. A steady state heat loss test was performed to relate the natural convection heat loss to room temperature and the heater temperature. The optical correction was achieved by comparing the distortion of an image before and after being viewed by 0.25” thick acrylic half-cylinder, Fig 4.2.7.1.6.

Figure 4.2.7.1.5: A photograph of the calibrated thermal liquid crystal pictured as capture with digital camera and thermocouples.

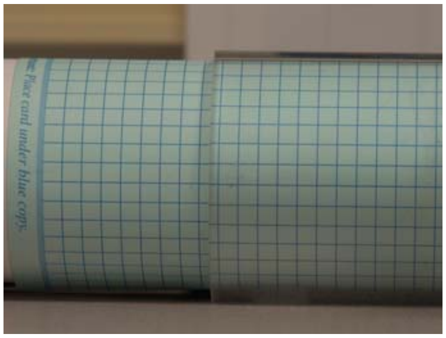

Figure 4.2.7.1.6: Effect of light distortion due to acrylic is function of the thickness and light direction.

The data reductions of the half-cylinder swirl cavity configuration for four flow rates and two jet arrangements are show in Fig 4.2.7.1.7 and Fig 4.2.7.1.8. Fig 4.2.7.1.8 shows local convection coefficient map variation with flow rates for both jet positions. Swirl flow is generated when the jets are located to the edge of the half circle cavity. Impinge flow is produced when the jets are located to the center of the cavity. By comparing the convection coefficient map, one finds that the swirl cooling with less mass flow rate can generate similar cooling effect as impingement. Similar conclusion can be drawn from the temperature map show in Fig 4.2.7.1.8. The figure shows that for same mass flow rate, the swirl flow is more effective in cooling than impingement flow. The data shows that as mass flow rate decrease then swirl flow cooling become more effective relative to impingement flow cooling. Therefore, as expected as mass flow increase, a little distinguish can be observed between both type of flow type and the percentage of mass reduction will decrease. As mass flow rate increase then more fluid will wash the surface and the jet position will have less impact on the flow cooling effect.

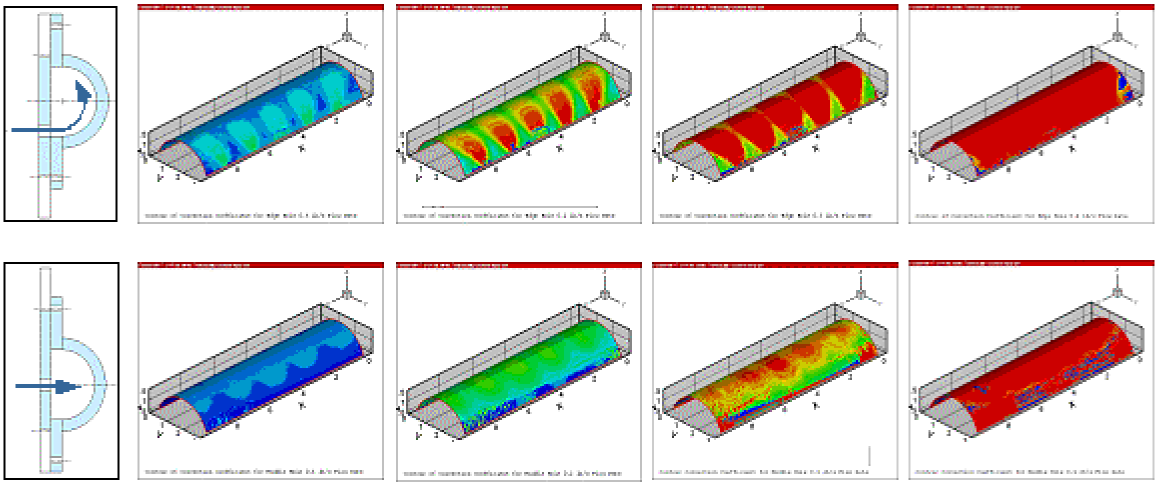

Figure 4.2.7.1.7: The local convection coefficient is calculated based on the liquid crystal tests for the swirl and the direct impingement cooling inside the half-cylinder swirl cavity.

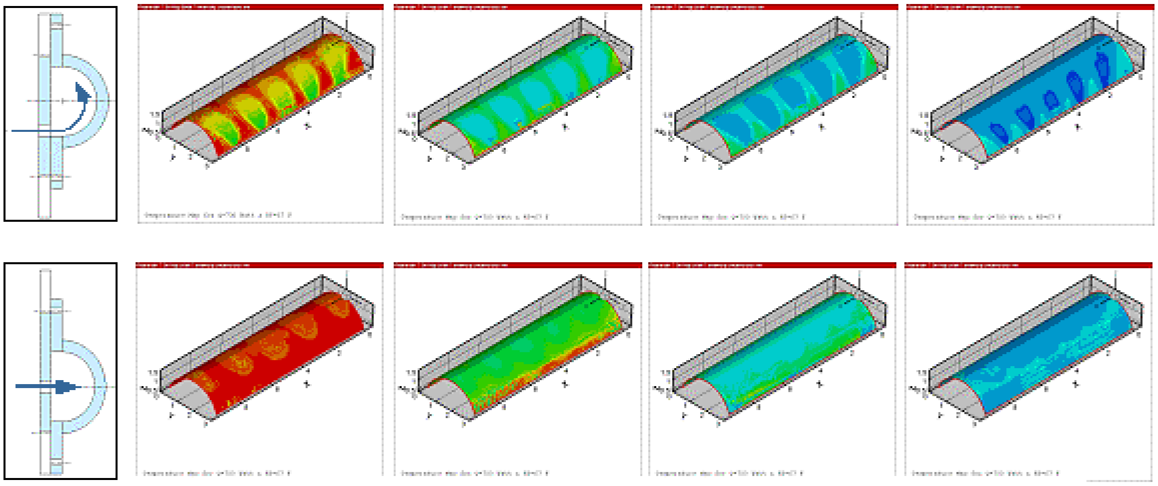

Figure 4.2.7.1.8: The temperature map is calculated based on the liquid crystal tests for the swirl and the direct impingement cooling inside the half-cylinder swirl cavity.

The local convection coefficient map is calculated, from different heat loads and the corresponding colored thermal liquid crystal images, using the following equation:

$$h_i = \frac{Q''}{(T_i - T_{in})}$$

Then the calculated matrices of the local convection coefficient value are combined and averaged based on the number of heat loads. The heat loads number was selected by making sure that every portion of the liquid crystal get colored image as heat load change.

The local temperature map is calculated based on the local convection coefficient map generated in the previous step. Using next equations, one can generate the repressive temperature map and average surface temperature.

$$T_i = T_{in} + \frac{Q''}{h_i}$$

$$T_{avg} = \frac{\sum_i T_i \ \Delta A_i}{A_{total}}$$

Using next equation, the temperature map is used to calculate the average convection coefficient of the half-circle cavity for same heat load of 700 Watt and air temperature of 70 $^0$F.

$$h_{avg} = \frac{Q''}{(T_{avg} - T_{in})}$$

The cavity shape effect was explored using 60-degree triangle swirl cavity shown in Fig 4.2.7.1.9 for local convection coefficient map and Fig 4.2.7.1.10 for temperature map. Similar to the half-cylinder swirl cavity, three layers including the electrical heater sheet, the liquid crystal, and the adhesive sheet were used.

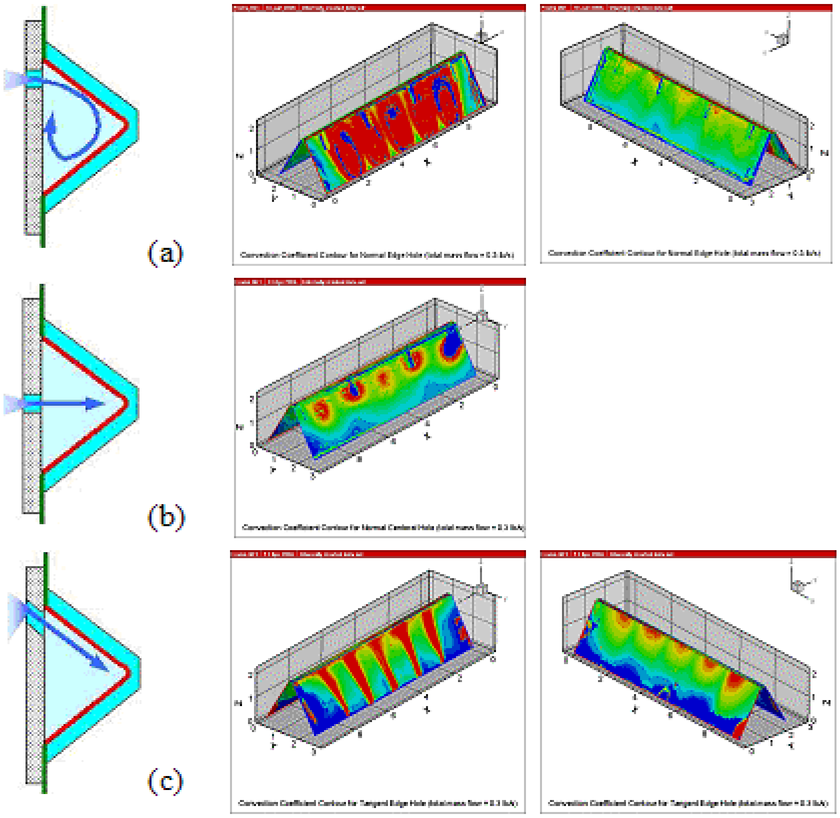

Figure 4.2.7.1.9: The local convection coefficient calculated based on the liquid crystal tests for the 60-degree triangle and the three jet locations; (a) Normal edge jet. (b) Normal center jet. (c) Tangent edge jet.

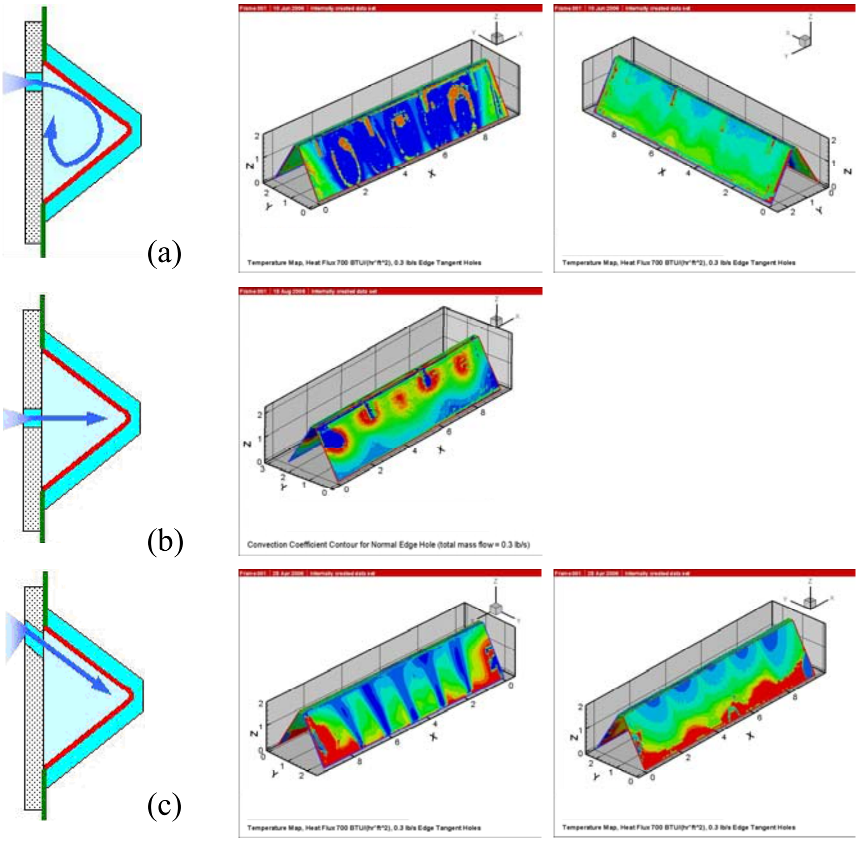

Figure 4.2.7.1.10: The temperature map calculated based on the liquid crystal tests for the 60-degree triangle and the three jet locations; (a) Normal edge jet. (b) Normal center jet. (c) Tangent edge jet

The local convection coefficient map data showed as expected that the edge jet (case (a) and (b)) will generate swirl flow which have higher average convection value compared to the central impingement jet (case (c)). Also, having the jet impinged to one side of the triangle before it start to reflect and swirl (case (a)) will generate stronger swirl than sending the jet tangent to the wall until it strike the other side of the triangle where it start turning to generate the swirl flow. Case (a) is combining the effect of impingement with strong swirl flow while case (b) utilizes part of the impingement but still it lost most of the momentum needed for the swirl flow. In case (b) the flow have to travel tangent to the side of the triangle wall loosing most of the energy before it hit the other side wall where it start to turn and form the swirl flow.

### 7.2.7.2 Trailing Edge Film Cooling

**Background**

A row of discrete film cooling slots is commonly found in the trailing edge region of high-pressure stage turbine airfoils to offer thermal protection from the high gas temperatures exceeding the metal temperature limits. Low temperature flow, bypassed from the compressor, is ejected from the slots providing a buffer between the hot mainstream and a small portion of the blade pressure surface at the blade trailing edge region. Adequate cooling of this region is imperative when considering the loss penalties associated with excessive cooling or the reduction in blade life due to inadequate cooling. Cooling of the TE region is evermore complicated by the fact that it is structurally the thinnest and weakest part of the blade. Figure 7.2.7.2.1 shows a drawing displaying some of the nomenclature commonly used in the published literature and adopted in this report.

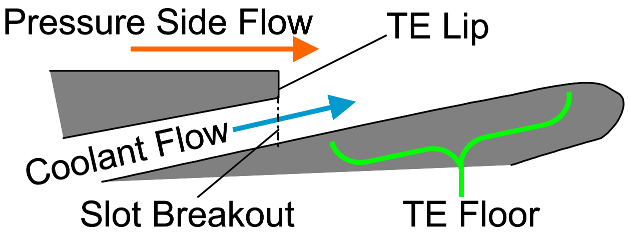

Figure 7.2.7.2.1 - Blade trailing edge cooling slot nomenclature.

Currently, there is limited amount of data available in the published literature in this area; however, in recent years there has been an increase in the number of studies conducted. Holloway et al. [1, 2] looked in great detail at the flow physics involved in the TE cooling slot region with an experimentally validated 3-D numerical model at transonic engine conditions. Results from the steady simulations revealed vortex structures behind the trailing edge lip, which were seen to be dependent on blowing ratio. A dip in effectiveness as a function of blowing ratio was observed in their experimental results. These were explained by unsteady simulations carried out, which showed the vortex shedding off of the trailing edge lip to be a key mechanism.

Martini et al. [3] measured film cooling performance downstream of various trailing edge cooling slots with varying internal geometries using IR thermography. Results revealed a region extending from the slot breakout where the film effectiveness is strongly influenced by the internal cooling design followed by a region of relatively fast decay in film effectiveness further downstream. Unsteady numerical flow simulations reported in Martini et al. [4] were used to associate the fast decay in film effectiveness to the flow instabilities generated in the wake of the TE lip.

Uzol et al. [5] looked at varying the cutback length on the pressure side and showed that increases in cutback length led to decreases in discharge coefficient and higher losses, which were associated with the increasing free-stream interaction length. Telisinghe et al. [6] investigated the difference in aero performance between a conventional trailing edge and a trailing with a sharp cut-back, both of which included film cooling. Larger discharge coefficients were measured for the cut-back configurations, which were attributed to the coolant flow being shielded from the free-stream and not being affected by the “capping” effect. Their loss measurements indicated little difference between the two test geometries. Cakan et al. [7] measured heat transfer on the TE floor, land surfaces (vertical walls adjacent to TE floor) and the breakout plane for cases incorporating an outward step using naphthalene sublimation technique. Interesting trends were revealed for a variety of Reynolds number and blowing ratios, and higher heat transfer coefficients on the land surfaces were reported 9 to 14 percent higher than the TE floor.

## Objectives

This study aimed at measuring the effects of incorporating variation in the shape of the slot geometry as a possible source of countering or delaying the rapid decay in film effectiveness seen by Holloway et al. [1, 2] and Martini [3]. It was envisaged that by measuring heat transfer coefficients on the TE floor for two different geometries, a difference in the performance of the geometries could be discerned.

## Technical Approach

To assess the effect of slot geometry on heat transfer to the trailing edge floor, two simplified models of trailing edge cooling slots were manufactured using SLA technique. The models were designed by extracting a section from a design blade CAD drawing (Figure 7.2.7.2.2a), which included a single slot (away from the endwalls) and the neighboring lands. A simplified CAD drawing was generated from the original section, which had a flat upstream surface and a total of three cooling slots (Figure 7.2.7.2.2b). These CAD drawings done in Unigraphics were used to generate SLA models. The SLA models (Figure 7.2.7.2.2c) were designed with a missing rectangular volume in the center, which covered the center TE slot floor. Rectangular acrylic pieces, instrumented with an Inconel heater and a sheet of steady-state liquid crystals were fitted into the missing space.

The experiments were designed to match the flow physics in the region of the TE cooling slot as closely as possible. The parameters matched in the bench-scale experiments were blowing ratios, velocity ratios, pressure side flow Reynolds number and cooling slot Reynolds number. The matching conditions, available testing capabilities and budget constraints resulted in a scaled-up model of several times that of the engine case. The scaled-up length of the trailing edge floor (from slot breakout to trailing edge in actual blade) was slightly increased. This allowed for an extra bit of length for measurements. Figure 7.2.7.2.3 illustrates the experimental setup, made of a channel with square cross-sectional area and the SLA model attached to an acrylic sheet, which extends upstream to the channel inlet.

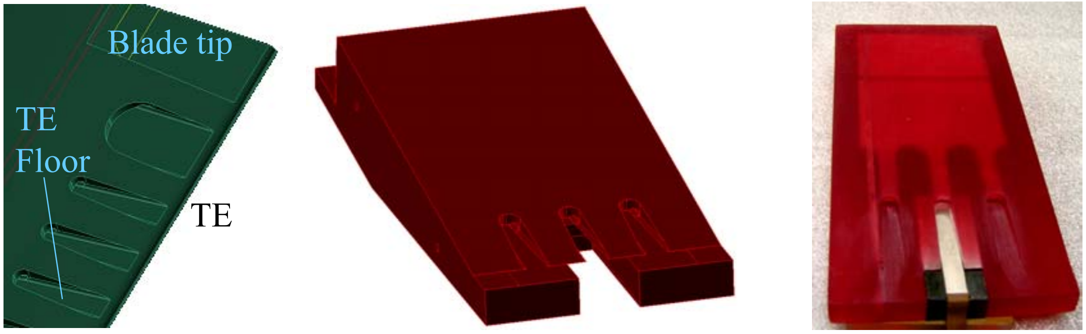

(a) (b) (c)

Figure 7.2.7.2.2 - (a) Unigraphics CAD drawing of design blade model, (b) Unigraphics CAD drawing of simplified TE cooling slot model, (c) SLA model instrumented with heater and wide-band liquid crystals.

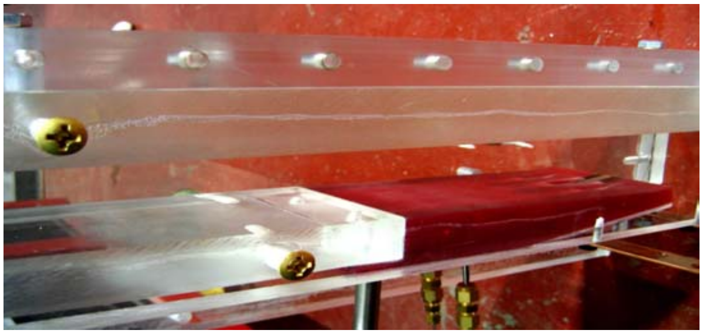

Figure 7.2.7.2.3 - Experimental Hardware.

A schematic drawing of the experimental setup is presented in Figure 7.2.7.2.4. Flow enters the main channel flow, which is representative of the pressure side flow in the engine, through a pressure plenum fixed to the inlet and is exhausted to atmosphere. A wire trip was placed upstream of the trailing edge cooling slots at a distance equivalent to the scaled-up blade chord length. Thermocouples are placed in the main channel and in the cooling slot model cavity for free-stream temperature measurements. Static pressure tappings are located at approximately 1 inch upstream of the slot breakout, 1 inch downstream of the slot break out and inside the slot model cavity. An orifice meter is used to measure the mass flow through the channel and a sonic venturi meter is used to measure the mass flow through the cooling slot models. The static pressure readings taken just upstream of slot breakout are used along with the channel flow temperature and mass flow to compute channel velocities. The static pressure readings just downstream of the slot breakout are used along the channel flow temperature and the cooling slot mass flow for cooling flow velocities. Another important feature displayed in the schematic is the fact that the cooling slots are angled relative to the channel flow, as in the engine case.

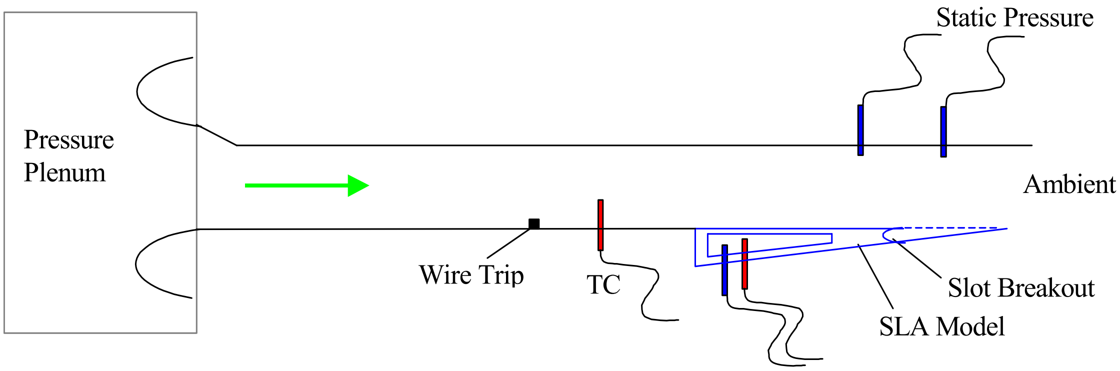

Figure 7.2.7.2.4 – Schematic drawing of experimental setup.

The experiments consisted of capturing steady-state liquid crystal temperature maps with a CCD camera for a sequence of power settings, which allowed for all the areas of the liquid crystal sheet to pass through the temperature band and produce a temperature map. At the beginning of each test, the mass flow rates were set to the desired conditions. For each run, steady state conditions were achieved at approximately 15 to 20 minutes after setting the power requirement. For each test, the channel flow and coolant flow temperatures were set to similar values. The heat transfer coefficients were computed using Eqn. (7.2.7.2.1), where $T_s$ is the liquid crystal temperature and the conduction loss $Q_{cond}$ was approximated by a power law function fitted to the a number of data sets. It was thought that this function approximated the losses due to conduction better than assuming a constant value for all cases, although the conduction loss only account for a few percent of the power at most. Experimental uncertainties for *h* were derived by the method proposed by Moffat [8]. Uncertainty in h was computed to be less than 10% for all cases.

$$h = \frac{Q_{heater} - Q_{Cond.}}{D \cdot L \cdot (T_S - T_f)} \qquad \text{Eqn. (7.2.7.2.1)}$$

## Results

Heat transfer coefficient maps are presented in Figure 4.2.7.3.5 for the baseline shape. The direction from left to right on the maps coincides with the direction from slot breakout to the trailing edge. Presented are results for coolant flow only at matched Reynolds number and the three blowing ratios, where Blowing ratio Case 3 is equivalent to case of blowing ratio equal to zero. The case with only main flow clearly reveals a stagnation region where peak *h* values are present at around 40% of the measurement length. A small enhancement in *h* is seen for all the cases with cooling flow. This is attributed to a small step at the slot breakout present in the model. The coolant flow, however, does have a higher convective heat transfer as it exits the slot and this in turn can be interpreted as better film cooling. A trend of increasing heat transfer with blow ratio can be seen by comparing blowing ratio cases 1, 2 and 3.

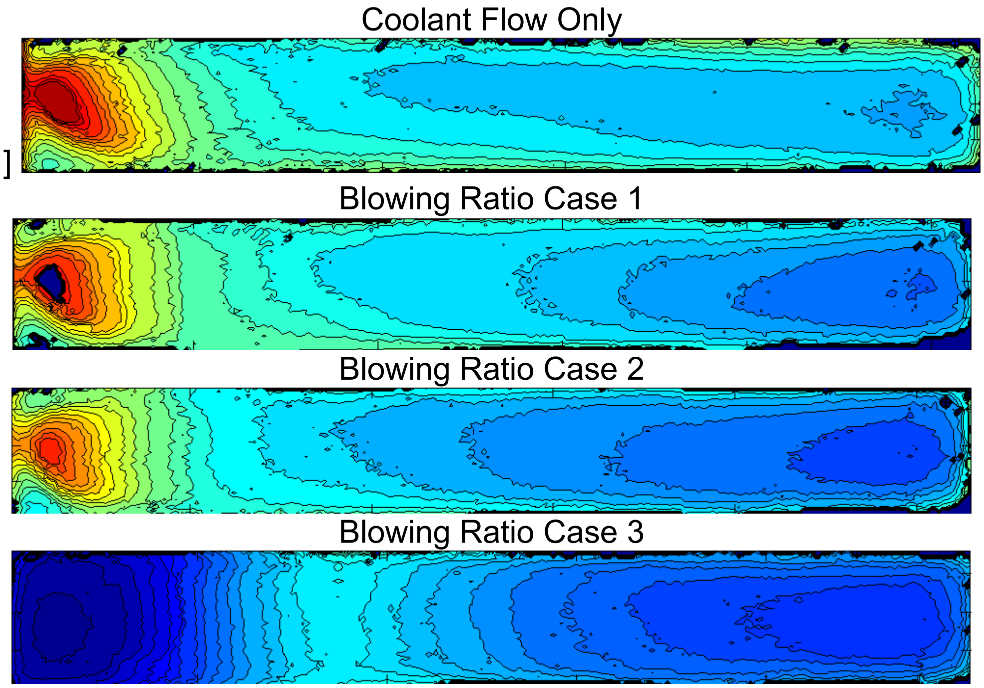

Figure 4.2.7.3.5 – Heat transfer coefficient maps for BASELINE shape slot.

Heat transfer results for the alternate shape geometry are presented in Figure 4.2.7.3.6. Presented are the cases with coolant flow only at matched Reynolds number and for 4 blowing ratios. An interesting trend of decreasing heat transfer coefficients with decreasing blowing ratio can be observed leading down to the lowest blowing ratio, which reveals a higher heat transfer region at approximately the same location where the baseline geometry experiences main flow stagnation, for the case of no coolant flow. Thus one can expect the main flow to penetrate deeper into the coolant flow and be more influential with lower blowing ratios, getting closer to the case where there is no coolant flow. Another interesting observation is the difference in the distribution of heat transfer coefficients, in comparison to the baseline geometry, specifically in the region of the first half of the TE floor. This could be the effect of vortical flow features developed from the alternate shape geometry. The latter parts of the TE floor seem to have somewhat similar heat transfer coefficient distributions to the baseline cases.

Centerline heat transfer coefficient signatures are analyzed for both geometries. The higher heat transfer coefficient signatures are seen to behave similarly for a given geometry after the region of main flow stagnation. In other words, the cases with no or low coolant flow have similar patterns to the cases of higher coolant flow (higher blowing ratios) after around 40% of the TE floor. This could suggest a dominant influence by the separating pressure side flow in the latter part of the TE floor.

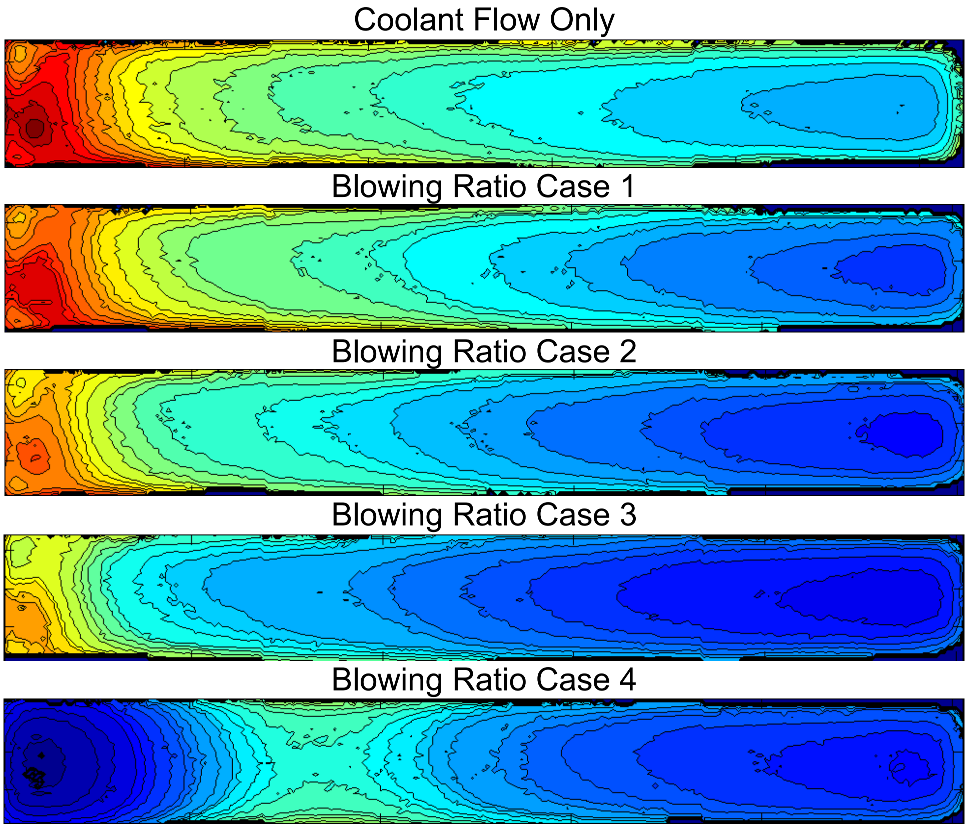

Figure 4.2.7.3.6 - Heat transfer coefficient maps for Alternate shape slot.

Cases with similar blowing ratios and mass flow ratios are compared. For the cases with similar blowing ratios, the alternate shape case are seen to have higher heat transfer coefficients at around 35% from the breakout. This difference is larger than the associated uncertainty in the measurements. If this difference is within the region where the main flow has not mixed significantly with the coolant flow, this can be a benefit in cooling performance. Although not as great, there are differences in *h* as early as 15% from the slot breakout where one can expect no influence by the main flow. However, these differences are small in comparison to the associated uncertainty. Looking at the cases with similar mass flow ratios, the differences are noticeable in at around 30% from the breakout. It is worth noting that mass flow ratio for the alternate shape is smaller than that of the baseline case and one can expect the difference in *h* to be greater at more similar mass flow ratios. Again, this difference in *h* can be beneficial to the cooling performance depending on the influence by the main flow.

Lastly, the heat transfer coefficient signatures at the centerline for both geometries at equal Reynolds number, which matched the engine Reynolds number, are compared. These are for experiments with no main flow present, just coolant flow. Here the difference in *h* signatures is very clear and significant for a large portion of the TE floor. It is important to realize that in the absence of the main flow, these two data sets are representative of the cooling performance of the geometries. Thus, the alternate shape provides better cooling to the TE floor surface. It is worth pointing out that these Reynolds numbers are computed from the true cross-sectional area of each of the geometries.

## Conclusions and suggestions

The current study looked at assessing any possible improvements on the cooling performance due to variation of the slot geometry. Although the experiments carried out were unable to clearly discern the effects of the main flow interaction with cooling flow, the results did reveal differences that could be beneficial to the cooling performance of these slots.

Suggestions of follow up work include the actual measurement of film effectiveness for both geometries. A very common method of measuring film effectiveness involves a higher temperature coolant or gas flow, which was not possible in the present study due to the temperature limitations of the SLA models. The measurement of static pressures along the TE floor could also reveal useful data. Flow visualization, possibly the use of PIV, would yield incredible insight to the flow behavior. Other things that may be worth looking into are effects on film effectiveness from a complete cut-back as that reported by Telisinghe et al.[6], where improvements in $C_d$ were noticed. Effects of slot geometry on heat transfer to the walls adjacent to the TE floor should also be investigated. Numerical modeling carried out in parallel with experimental work on the alternate slot geometry would be favorable.

## Nomenclature

| | |
|---|---|
| BR | Blowing ratio ( $\frac{\rho_{Cool}u_{Cool}}{\rho_{PS}u_{PS}}$ ) |
| C | Blade chord length |
| CAD | Computer Aided Design |
| $C_d$ | Discharge Coefficient |
| D | Heater width |
| h | Heat transfer coefficient, (Eqn. 1) |
| H | Slot max height |
| L | Heater length |
| Ma | Mach number |
| MR | Momentum Ratio |
| MassR | Mass flow ratio ( $\frac{\dot{m}_{Cool}}{\dot{m}_{PS}}$ ) |
| $\dot{m}$ | Mass flow |
| $\mu$ | Viscosity |
| P | Pressure |

| | |
|---|---|
| $Q_{heater}$ | Heater power |
| $Q_{cond}$ | Conduction losses |
| R | Statistical parameter |
| $Re_{Cool}$ | Reynolds number of coolant flow ($\frac{\dot{m}}{\mu W}$) |
| $Re_{PS}$ | Reynolds number of pressure side flow($\frac{\rho \cdot u_{PS} \cdot C}{\mu}$) |
| ρ | Density |
| SLA | Stereo Lithography Apparatus (rapid prototyping technique) |
| TE | Trailing Edge |
| TC | Thermocouple |
| T | Temperature |
| u | Velocity |
| VR | Velocity Ratio ($\frac{u_{Cool}}{u_{PS}}$) |
| W | Slot max width |

subscripts

| | |
|---|---|
| Cool | Coolant flow parameter |
| PS | Pressure side flow parameter |
| F | Fluid Property, equal to average of $T_{cool}$ and $T_{PS}$ |

## References

[1] Holloway, D.S., Leylek, J.H. and Buck, F.A., 2002, “Pressure Side Bleed Film Cooling, Part 1: Steady Framework For Experimental and Computational Results,” ASME Paper GT2002-30471.

[2] Holloway, D.S., Leylek, J.H. and Buck, F.A., 2002, “Pressure Side Bleed Film Cooling, Part 2: Unsteady Framework For Experimental and Computational Results,” ASME Paper GT2002-30471.

[3] Martini, P., Shulz, A., and Bauer, H.J., 2006, “Film Cooling Effectiveness and Heat Transfer on the Trailing Edge Cutback of Gas Turbine Airfoils with Various Internal Cooling Designs,” ASME Journal of Turbomachinery, Vol. 128, pp.196-205.

[4] Martini, P., Shulz, A., Bauer, H.J., and Whitney, C.F., 2005, “Detached Eddy Simulation of Film Cooling Performance on the Trailing edge Edge Cut-Back of Gas Turbine Airfoils,” ASME Paper No. GT2005-68084.

[5] Uzol, O., Camci., and Glezer, B.,, 2001, “Aerodynamic Loss Characteristics of a Turbine Blade with Trailing Edge Coolant Ejection – Part 1: Effect of Cut-Back Length, Spanwise Rib Spacing, Free-Stream Reynolds Number, and Chordwise Rib Length on Discharge Coefficients,” ASME Journal of Turbomachinery, Vol. 123, pp. 238-248.

[6] Telisinghe, J.C., Ireland, P.T., Jones, T.V., Barrett, D., and Changmin, S., 2006, “Comparative Study Between a Cut-back and Conventional Trailing Edge Film Cooling System,” ASME Paper GT2006-91207.

[7] Cakan, M. and Taslim, M.E., 2006, “Experimental and Numerical Study of Mass/Heat Transfer on an Airfoil Trailing-Edge Slots and Lands,” ASME Paper GT2006-91201.

[8] Moffat, R.J., January 1988, “Describing the Uncertainties in Experimental Results,” Experiment Thermal and Fluid Science, Vol. 1, pp. 3-17.

### 4.2.7.3. Unsteady Impingement Heat Transfer Tests

#### Background

Direct impingement cooling of heated engine surfaces (turbine blades etc) is frequently employed through the use of a cooler higher pressure fluid (as would typically be provided by a compressor stage). Recent research in this area has indicated that unsteady or periodic application of this impingement cooling may result in increased heat transfer coefficients for a given mass flow. A preliminary investigation has been accomplished to study the effect of impingement air cooling, against a heated surface, for steady and periodic flows of varying frequencies.

#### Objectives

To explore entitlements due to flow oscillation relative to steady flow for a given set of flow conditions. Steady flow cooling performance (using air against a heated surface) is to be directly compared against pulsed flow cooling (equal time on equal time off) over varying frequencies. Evident and promising trends will be identified and suggested for possible future work.

#### Technical Approach

Traditional impingement cooling is comprised of steady flow; with heat transfer coefficients primarily a function of nozzle hydraulic diameter, Prandtl number, distance from heated surface (L/D) and Reynolds number. Periodic flow comparisons would match all of these parameters as closely as possible during “on” periods of operation.

Steady flow was to be accomplished using two stationary round nozzles situated at a fixed distance apart with a predetermined nozzle diameter. These two nozzles strike a heated flat surface at an angle of $90^o$ (I.e. normal to the surface). Both nozzles are fed shop air from the same uniform low velocity source and should exhibit identical behavior. In this configuration, duplicate sets of data can hopefully be realized and also any interaction between jets identified. For all cases investigated, air used was at or slightly higher than ambient temperature.

The heated flat surface is comprised of a thin film electrical heater bonded to a thin liquid crystal sheet. The liquid crystal is then covered with a thick acrylic plate. The acrylic plate serves two purposes; first to allow visual access to the liquid crystal sheet, and second to provide an insulating barrier between the heated sheet and the atmosphere.

Power is supplied to the heater using a DC power controller in levels sufficient to excite the liquid crystal sheet over its calibrated temperature range.

Liquid crystal data is collected via an RGB camera and processed digitally to arrive at corrected temperatures and local heat transfer coefficients. Main flow jet data is collected automatically using a computerized data acquisition system once steady state (or quasi steady state for pulse flow) conditions are reached.

Pulsed flow operation is attained by introducing a periodic blockage over the path of the nozzle. This periodic blockage is accomplished by spinning a partially open plate at a prescribed RPM through the use of a precise stepper motor. For the configuration tested, each nozzle was pulsed “on” or “off” at the same time.

Figure 4.2.7.3.1 depicts the test arrangement used. Figure 4.2.7.3.2 depicts the flow oscillator details.

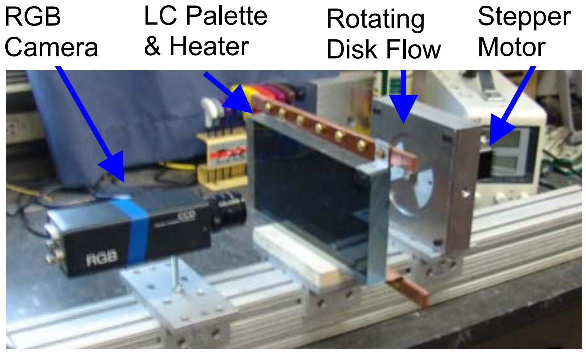

Figure 4.2.7.3.1 Test Arrangement

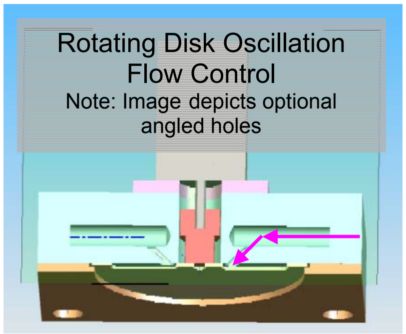

Figure 4.2.7.3.2 Flow Oscillation Control

Data sets were collected for three jet flow regimes: No flow (to document static heat losses to the environment), steady flow, and pulsed flow.

RGB data was collected over several power levels (for each jet flow condition) such that overlapping rings of excited crystal could be summed to arrive at calculations of heat transfer coefficient over the area of interest. During pulsed flow operation numerous RGB images were collected over a prescribed time period and then averaged to provide a time averaged result.

## Results

One steady flow test condition was selected to be used to baseline performance. The condition chosen provided a fixed Reynolds number with a fixed L/D ratio. These values are typical average values for impingement cooling applications. Several rotational RPM's were chosen to document frequency response based upon a time averaged heat transfer coefficient.

Figure 4.2.7.3.3 provides a color surface plot of generalized heat transfer coefficients for the baseline (steady flow) case, while Figure 4.2.7.3.4 provides a color surface plot for a typical pulse flow under the same conditions.

For all cases it has been shown than pulse cooling provides a lower overall heat transfer coefficient (based upon a contact area average), though these values are accomplished using only 50% of the flow. Taking mass flow into account, a net gain in overall heat transfer coefficient is realized as the decrease in local (and area averaged) heat transfer coefficients was less than 50%.

Pulse frequency has been shown to have an effect on the overall heat transfer coefficient.

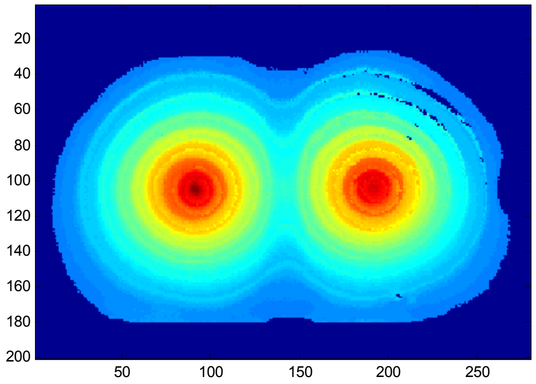

Figure 4.2.7.3.3 – Steady Flow "h"

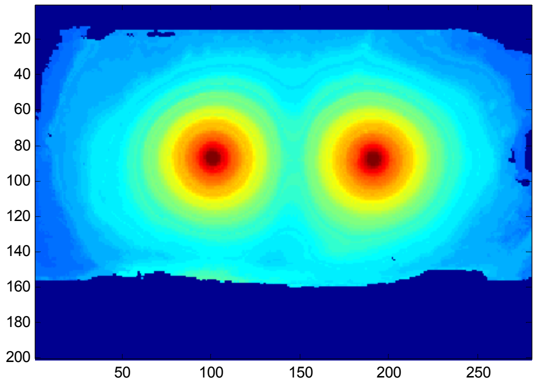

Figure 4.2.7.3.4 – Pulse Flow "h"

## Implications for Active Cooling Control

Increased heat transfer coefficients have been identified while using pulse flow in lieu of steady flow for impingement cooling (on an averaged mass flow basis). Implementing pulse flow cooling is more complex than steady flow, but if properly applied measurable savings in chargeable cooling air could be realized.

## Conclusions

On a mass averaged basis, pulse impingement cooling has been shown to provide higher overall heat transfer coefficients that traditional steady flow impingement cooling.

The above represents a proof of concept evaluation at a fixed set of conditions. Increasingly valuable information could be obtained through continued research in this area. Influencing factors such as distance between jets, alternating verses parallel pulsing, Reynolds # and L/D are just a few of the parameters that could be readily adapted to the current test apparatus to obtain much needed information to effectively exploit this phenomenon.

### 4.2.8 Expendable and Closed-Loop CCA Systems (Parker Hannifin)

In concert with GEA, Parker Hannifin engineers developed concepts on how water injection could be applied for cooling hot compressor discharge air.  Parker designed and fabricated a test model of one concept that was tested in the GE Global Research high-temperature combustor test cell.  Parker also conducted a series of design studies on alternate CCA system designs for turbine cooling applications.

### 4.2.9 Expendable CCA Model Tests (GE Global Research)

**Objective**

Experiments were performed for water injection configurations dedeveloped in Subtask 4.2.8. These tests were completed by GEGR in one of their high-temperature, high-pressure test facilities. The purpose of these tests was to prove the performance of these spray nozzles for water injection into a high pressure and high temperature air stream. Such water injection could be supplied by a finite reservoir of water to provide a near step reduction in air temperature.

The test hardware was supplied by Parker Hannifin and consisted of a 3-passage linear cascade. Two spray bars, one with 5 nozzles and one with 7 nozzles, were provided by Parker Hannifin to inject water, at different prescribed distances upstream of the vanes, into air flowing through the cascade.

**Conclusion**

Experimental tests show that water injection into high temperature and pressure air streams will indeed lower the air temperature within a short distance from the injection location.

### 4.2.10 Simulink/FlowSim Models of Cooled-Cooling Air Schemes

#### 4.2.10.1 Objectives

Objectives are to develop Simulink/FlowSim models of air cooling schemes, namely:

a) Air-to-air cooling
b) air cooling with previously mist cooled air
c) air-mist cooling inside the heat exchanger

These models are intended to be used as sub-models of a larger engine model. They would enable evaluation of the performance of different types of air cooling schemes and their impact on the system level performance.

#### 4.2.10.2 Technical Approach

Air cooling is done using a cross-flow heat exchanger (single pass, unfinned with cold side mixed and staggered arrangement). The effectiveness-NTU method is used in modeling the heat exchanger. As described above three different cooling schemes are modeled at steady state conditions.

#### 4.2.10.2.1 Air Cooling

The FlowSim interface for the air cooling scheme is shown in Figure 4.2.10.1. Starting from the left side in Figure 4.2.10.1 with two FlowSim library components “IN” (fluid supply components) the fluid type, mass flow rate [lbm/hr], temperature [F], and pressure [psi] for the hot air (cooled air) and cold air (secondary air) are specified. However, due to incorrect fluid properties for full range of temperatures and pressures new fluid property functions are developed and embedded into the model making air the only fluid that can be used (not other fluid should be chosen in “IN”). From there the secondary air stream flows directly to the heat exchanger. The cooled air stream is first divided into two streams; the first bypasses the heat exchanger and the second flows through it. Icon “Air Splitter” is a renamed FlowSim library component that divides the inflow into two streams according to specified percentage and assumes no pressure loss. The “Cross-Flow HX” component is developed to model cross-flow heat exchanger (single pass, unfinned with cold side mixed and staggered arrangement) with two air streams using the effectiveness-NTU method. Variables used to size and define material of a heat exchanger are defined in this component.

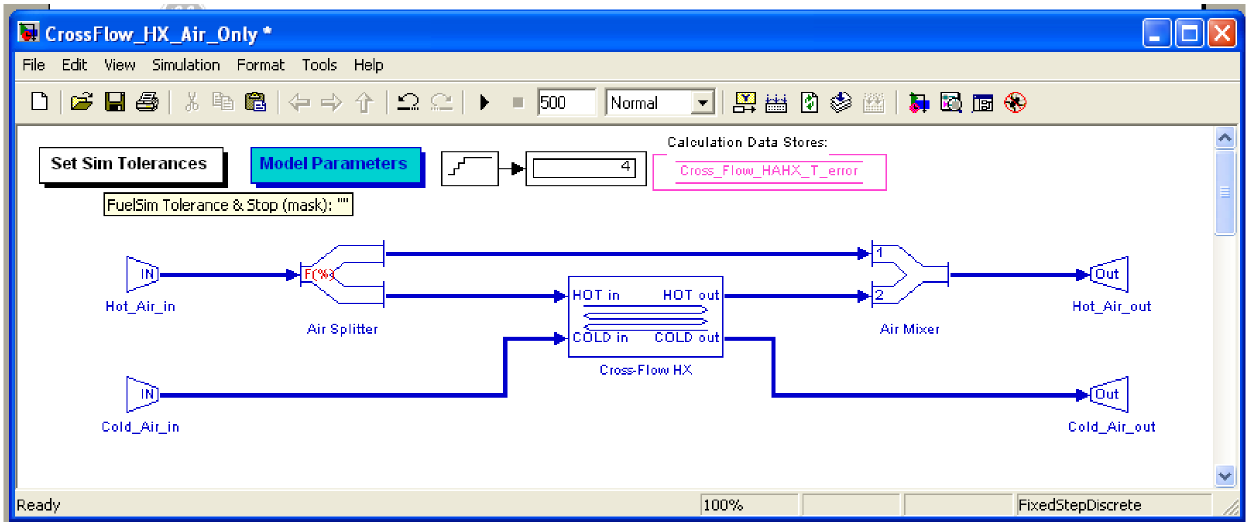

Figure 4.2.10.1 Air cooling FlowSim interface

The Gnielinski correlation is used for calculating the Nusselt number inside the tubes, while the Zhukauskas correlation is used for calculating the Nusselt number across tube bundles. Temperatures used in evaluating fluid properties (average mean temperature, film temperature, etc.) when calculating the Nusselt numbers are determined according to Incropera and DeWitt ("Fundamentals of Heat and Mass Transfer" 4th edition). The Petukhov correlation is used for calculating the Darcy friction factor inside the tubes, while diagrams are used for flow across tube bundles. Fluid properties are evaluated according to Incropera and DeWitt ("Fundamentals of Heat and Mass Transfer" 4th edition). The cooled air stream flowing out of the heat exchanger is then adiabatically mixed with the bypassed stream in a developed component called "Air Mixer". Temperature of the mixture is calculated from the mixture enthalpy. No pressure drop is assumed in this process; the mixture pressure is equal to the air stream pressure coming from the heat exchanger. After that the combined stream is directed to the FlowSim library component "Out" to end the code. The same procedure is followed for the secondary air directly from the heat exchanger.

#### **4.2.10.2.2 Air Cooling with Previously Mist Cooled Air**

Figure 4.2.10.2 shows the FlowSim interface for the air cooling with previously mist cooled air scheme. The only difference to the air cooling scheme is that the secondary air stream is cooled by injecting water droplets into its stream, which is modeled with "Air Mist Cooling" component. Temperature of the air/water vapor mixture is calculated from the mixture enthalpy. Assumptions made are that all water droplets completely evaporate before reaching the heat exchanger, no pressure drop occurs in the air flow, and water vapor fraction does not noticeably change velocity or properties of the air/water vapor stream compared to the secondary air stream alone. Relative humidity display with red background has to be checked at each simulation. In case it exceeds 1 the water mass fraction must be reduced. Water is supplied from the FlowSim library components "IN" in the same manner as air. Water mass flow rate is defined as a fraction of the secondary air mass flow rate. Due to incorrect steam properties new steam property functions are developed and embedded into the model making water the only fluid that can be used as the air coolant. After the “Air Mist Cooling” component the model is identical to the air cooling scheme model.

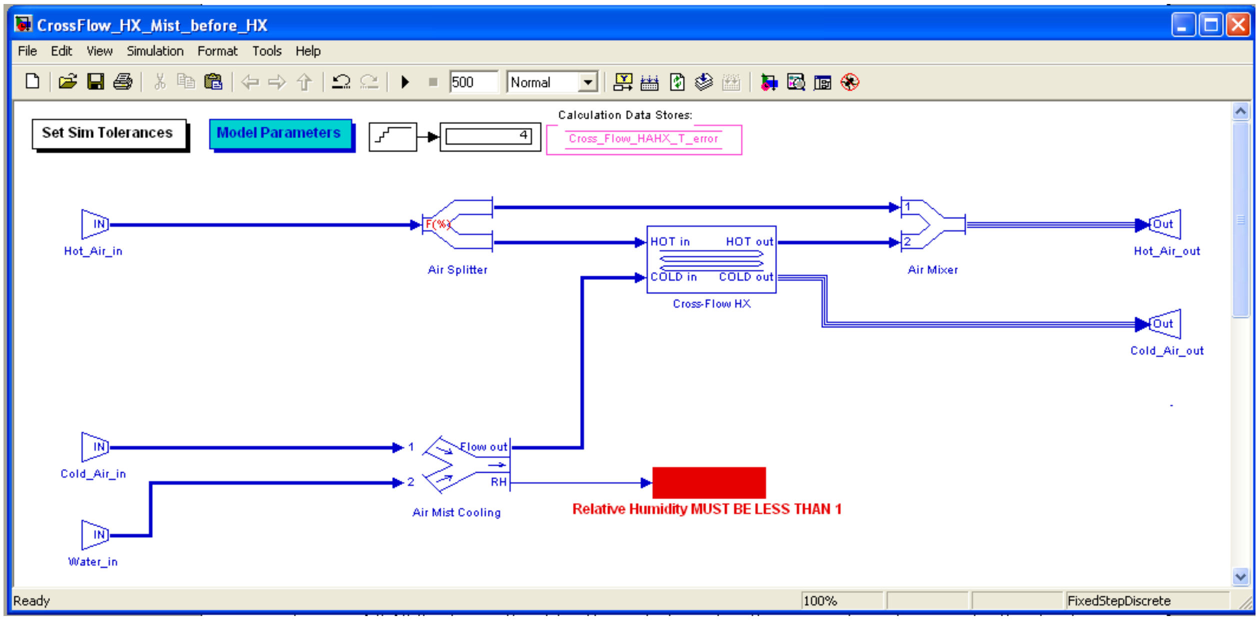

Figure 4.2.10.2 Air cooling with previously mist cooled air FlowSim interface

#### <u>4.2.10.2.3 Air-Mist Cooling Inside the Heat Exchanger</u>

Figure 4.2.10.3 shows the FlowSim interface for the air-mist cooling inside the heat exchanger scheme. The only difference to the air cooling scheme is that water droplets are injected directly into the heat exchanger at the secondary air side. This is modeled with the “Cross-Flow HX with Mist” component. Assumptions made in this model are: injected water droplets deposit onto the core tubes and the droplets mass flow rate and deposition are high enough to ensure significant wetting of the core tubes essentially removing thermal resistance on the outer tube surfaces, temperature of the injected droplets is equal to the inlet cold air stream temperature, all droplets completely evaporate before exiting the heat exchanger, and water vapor fraction does not noticeably change velocity or properties of the air/water vapor stream compared to the secondary air stream alone. If the thermal resistance assumption is not valid the heat exchanger predicted performance is considerably overestimated. Relative humidity display with red background has to be checked at each simulation. In case it exceeds 1 the water mass fraction must be reduced. Water droplets mass flow rate is defined as a fraction of the secondary air mass flow rate. Due to the same reasons as in the air cooling with previously mist cooled air scheme only water can be used for core tubes mist cooling since the properties of water are embedded into the “Cross-Flow HX with Mist” component. Apart from the heat exchanger this model is identical to the air cooling scheme model.

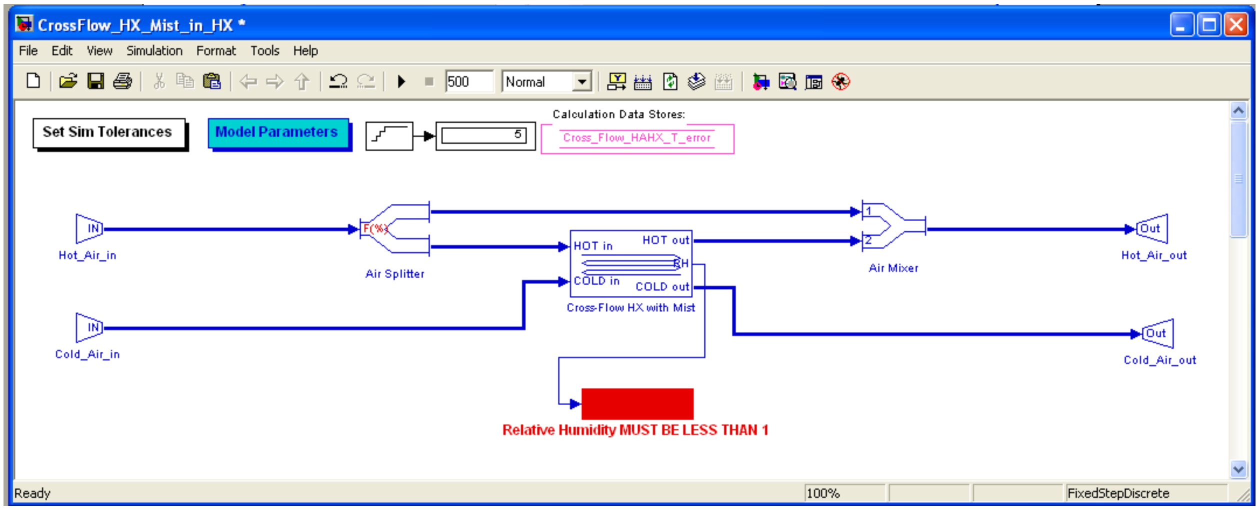

Figure 4.2.10.3 Air-mist cooling inside the heat exchanger FlowSim interface

## 4.2.10.3 Summary / Conclusions

Three different Simulink/FlowSim models of air cooling schemes are developed (i.e. air-to-air cooling, air cooling with previously mist cooled air, and air-mist cooling inside the heat exchanger). These models can be used as sub-models of a larger engine model to enable a performance evaluation of different types of air cooling schemes and their impact on the system level performance.

## Subtask 4.2.11 Enhanced Cooling Experiments

### 4.2.11.1 Boundary Layer Modifying Surface Dimples

#### Background

In 1994, as part of the inlet guide vane validation program for an engine, GE Global Research performed a series of film cooling studies in a high-speed linear airfoil cascade. During these tests, data was obtained with film holes on the suction side of the airfoil with and without flow of coolant through the holes. Unexpectedly, in the case of non-flowing film holes placed on the suction side, the downstream heat transfer coefficient distribution on the airfoil was reduced by approximately 20% compared to an airfoil with plugged film holes. This reduction in heat transfer coefficients was seen over a wide range of airfoil Reynolds numbers. The data showed that the effect of the non-flowing film holes began after the location of the film rows on the suction side (labeled in figures).

Subsequent to this discovery, GE applied for and obtained a US patent, “Airfoil with Reduced Heat Load”, #6,183,197 B1, issued Feb. 6, 2001. This patent teaches the use of one or more dimples or depressions on a turbine airfoil for the purpose of modifying the boundary layer to reduce heat transfer coefficients. Based upon the earlier cascade data, it is thought that dimples of similar size and shape to film hole footprints serve to modify the hydrodynamic and/or thermal boundary layers.

#### Objectives

The present feasibility study carries on the earlier research to provide clear evidence of heat transfer distribution reduction on an HPT blade model using a single row of dimples.

#### Technical Approach

For the present work, a high-speed linear airfoil cascade representing a HPT blade is used. The blade cascade is shown in a schematic cross section in Figure 4.2.11.1, including the current Infrared viewing window location to the suction side of the center airfoil. A complete description of the facility and operating conditions is provided in the publication by Bunker et al. “Heat Transfer and Flow on the First Stage Blade Tip of a Power Generation Gas Turbine Part 1: Experimental Results”, *Journal of Turbomachinery*, Vol. 122, pp. 263-271. The cascade operates at a nominal overall airfoil pressure ratio of about 1.4, but can be extended to higher levels. As depicted in Figure 4.2.11.2, the single row of dimples (shown as elliptic depressions in this example) is located in the so-called high curvature region of the airfoil suction surface. This is the vicinity where the boundary layers are expected to be most sensitive to any surface modifications. Figure 4.2.11.3 shows the dimensional layout of each row tested. The dimple depth at the center in the example shown is .050 inches. This depth was maintained constant for each shape of dimple tested, with the location of maximum depth dependent on the specific shape.

Four blades were manufactured using a 3D printing technique known as Fused Deposition Modeling. The photos in Figure 4.2.11.4 show the result of one rapid prototyped airfoil manufactured with thermoplastic material. The airfoil is constructed as a thin shell with internal cross webbing to reduce the layered deposition time. The interior cells of the airfoil are then filled with either a low thermal conductivity, pourable silicon RTV material, or with an epoxy resin. The fill material provides thermal insulation capability, but more importantly is required to strengthen the weaker shell structure. The external surface of the suction side downstream of the dimple row is recessed from the original aerodynamic shape to allow the attachment of a heated surface layer. The airfoil test is run as a steady-state flow condition with a constant heat flux generated on the suction surface in the area noted. The recessed surface region is fitted with a layer of hard rubber sheet of 0.125-inch thickness as a compliant and electrically insulating layer. A thin foil inconel heater is then adhered to the surface of the rubber. The heater is a composite of .0005 inches inconel deposited on about .0035 inches of Kapton, with copper foil buss bars attached on the ends (top and bottom of test airfoil). The adhesive is simple double-sided photo mounting film. The result is a constant heat flux surface over the entire suction side aft of the dimple row, with excellent thermal insulation underneath to reduce backside losses to a negligible level. Thermal radiation losses from the heater surface are also negligible.

As noted in Figure 4.2.11.1, an Infrared camera (FLIR Thermovision A40M) views the airfoil surface of interest through a window in the cascade tailboard. The window is a 3-inch diameter disk of Calcium Fluoride chosen for its very high and constant transmissivity over the 3-5 micron wavelength range of the camera. The camera is positioned to see most of the surface downstream of the dimple row. With the airfoil unheated, the camera records the surface map of recovery temperatures for the airfoil under adiabatic conditions. The mainstream air of the cascade is then left to run at room temperature, while the airfoil surface portion is elevated in temperature by the heater. The temperature map of the surface is again recorded with the IR camera to obtain the non-adiabatic response. The heat flux is known, so the local heat transfer coefficients can be calculated from

$Q/A = H\,(T_{surface} - T_{recovery})$.

Any modification of the boundary layers will result in some change to the heat transfer coefficient map. The correct recovery temperature distribution to be used for each dimpled surface test is actually that of the non-dimpled airfoil. Any changes in test-to-test mainstream air temperature are scaled to obtain consistent recovery temperatures for each test.

## Results

Due to the time constraints on this task, only two tests were completed, that of the baseline non-dimpled blade, and the blade with diffuser shaped dimple row. Figure 4.2.11.5 shows the side-by-side heat transfer coefficient maps for both test conditions. Each blade was tested with an overall airfoil pressure ratio of 1.6. For simplicity, the heat transfer coefficient results are based on the inlet air temperature to the cascade as the reference temperature, not the local recovery temperatures as originally noted. The inlet air total temperature was the same for each test at 97-deg F. The dimple row itself is not viewed in the images shown, but is just out of view along the lower edge of the images. Mainstream flow is from bottom to top in these images.

The applied heat flux over equal surface areas for each test was the same at 280 W. As indicated in the results, the surface temperature of the diffuser shaped dimpled row blade was higher, leading to a lower heat transfer coefficient. Discounting the extreme edge regions of the window viewing, the broad portion of the downstream surface from the dimple row location experiences heat transfer coefficients about 15% less than those of the smooth, non-dimpled surface. This result is in agreement with the cascade test data from several years ago, but is now achieved on an unambiguous airfoil surface with dimple features that do not penetrate to an internal chamber. The 15% difference in heat transfer coefficients is just outside the typical experimental uncertainty for such tests, which is about 10% for these steady-state flow conditions using an IR camera.

## Implications for Active Cooling Control

The main implications for any form of active cooling control come with the overall reduction in heat load for a turbine airfoil in as much as the active cooling control would require less capability, or alternately could be more effective.

## Conclusions

This short feasibility study has provided unambiguous confirmation that heat load reduction can be obtained on high-pressure turbine airfoils through the use of correctly sized and placed rows of dimples on the exterior surface. The range of potential magnitudes in heat load reduction must yet be determined by parametric studies. Interaction with other cooling mechanisms such as film cooling and active cooling control will also need further study.

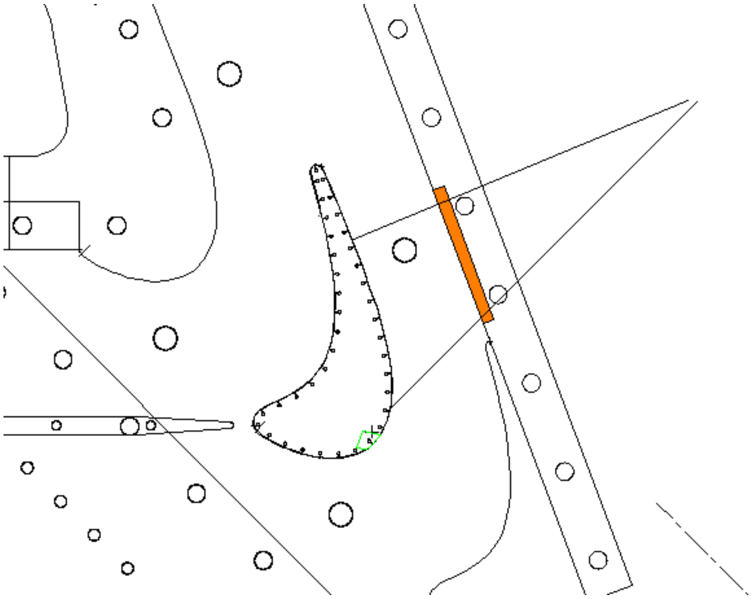

Figure 4.2.11.1 Current HPT Blade Cascade with IR Window View

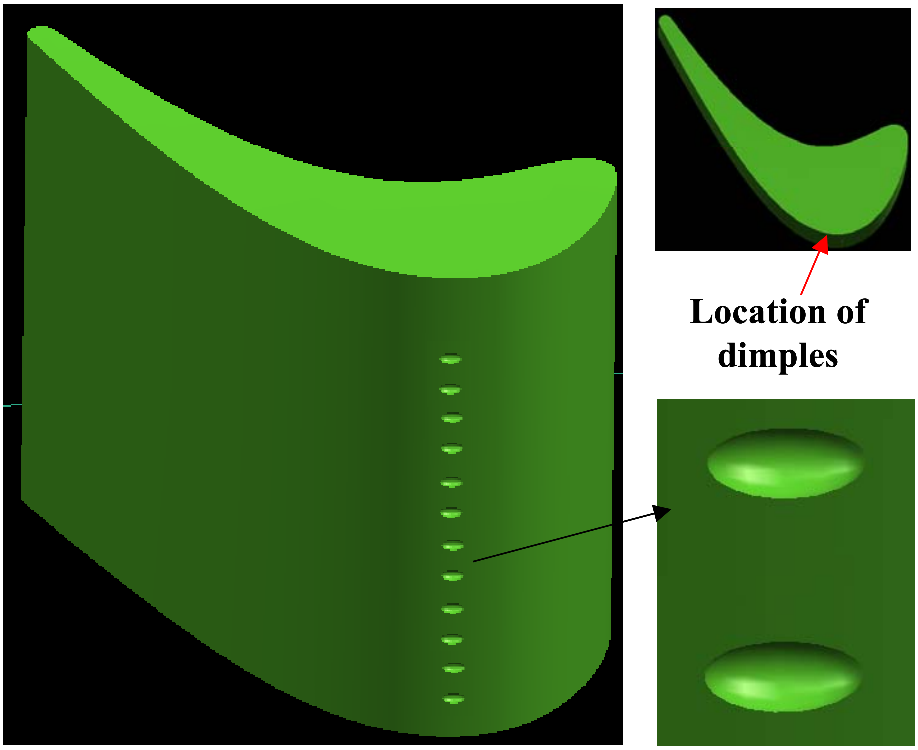

Figure 4.2.11.2 Blade with Modeled Elliptical Dimple Row on Suction Side

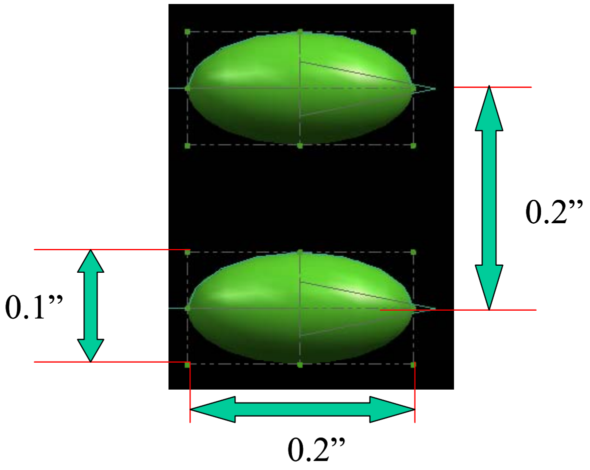

Figure 4.2.11.3 Elliptic Dimple Dimensions

Figure 4.2.11.4 Test Airfoil with Dimple Row (heater not installed)

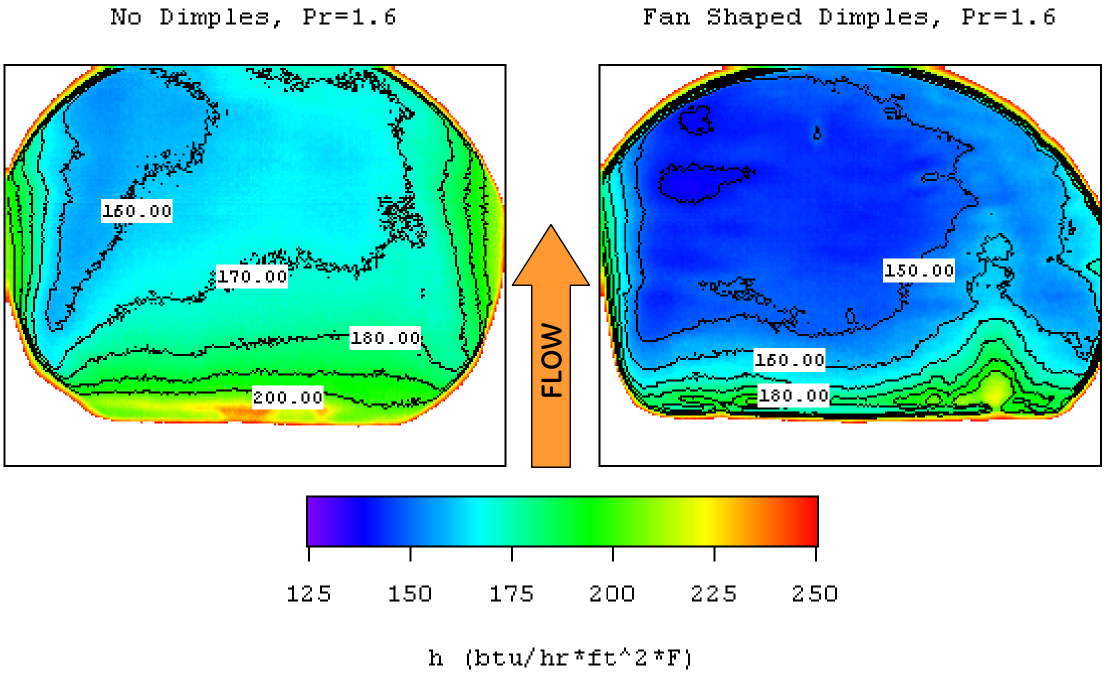

Figure 4.2.11.5 Experimental Heat Transfer Coefficient Distribution Comparison

### 4.2.11.2 Dual-Swirl Cooling

#### Background

During the last few years, GE Global Research has been performing research on various alternative turbulated channel geometries with the goals of higher heat transfer coefficients and/or lower effective friction coefficients. One class of turbulated surfaces in these studies concerned the use of broken and staggered chevron strips to generate secondary near-surface flows in at least two opposing directions. These strips are the result of removing the apex of a series of chevron turbulators, leaving opposed 45-degree strips. Staggering of the rows of strips provides additional flow mixing. Several examples of studies with some form of these broken chevron strips are present in literature from various researchers.

In 2005, GE applied this geometry in a non-square channel to deliberately take advantage of the angled strips to return directed flows back to the center of the channel. The 2005 tests were aimed at a purely convective passage with very high Reynolds number flow on the order of 300,000. Shown in Figure 4.2.11.6 are some of these earlier test results for the chevron strips as well as a smooth channel and a channel with transverse turbulators. The laterally averaged heat transfer coefficients plotted along the length of the channel show the chevron strips to provide a far more uniform distribution compared to the periodic nature of the transverse turbulators.

#### Objectives

The dual-swirl behavior resulting in higher heat transfer uniformity is studied in the present research under two flow conditions, one of convective channel flow with Reynolds numbers of 30,000 to 70,000 (more indicative of aviation engine blades), and the other with distributed impingement cooling jets having jet Reynolds numbers of 10,000 to 22,000.

#### Technical Approach

The test channel from the earlier GE study is used, but flow is scaled to the new requirements. It is scaled up many times to provide good full-surface detail in heat transfer coefficients. A steady-state liquid crystal technique is used to detect and record internal surface temperatures at several constant heat flux conditions. The model is constructed of acrylic to provide thermal insulation for the heat flux condition, and also to allow backside viewing of the liquid crystal response with a CCD camera. The interior surface of the test section is covered with a thin layer of liquid crystals, then a Kapton-backed thin-foil heater and its thin copper buss bars. Any turbulation features such as the broken chevrons are applied using semi-rigid foam material, hence these are not thermally participating features in this test. In the present series of experiments, the flow development region of the channel is also heated. Insertion thermocouples along the test channel monitor the bulk coolant temperature.

The test channel has been modified for the current tests to allow coolant introduction either as purely convective flow from a large plenum at the base, or as impingement jet flow through a series of sixteen nozzles. For the impingement flow, each supply jet has a nominal diameter of 1-inch. The jet centerlines are spaced 2.5 inches apart. The jets are aligned to target the center of the channel where the division of the broken chevrons occurs. Each jet is supplied via a flexible tubing section. To assure that flow is evenly distributed among all sixteen jets, each line also contains an upstream choked orifice. The assembly is supplied with a common coolant header that feeds all of the impingement lines. Exhaust air is allowed to flow to ambient. The total model flow rate for these tests ranges from 0.13 to 0.27 lbm/sec.

## Results

The baseline smooth impingement surface heat transfer coefficients are shown in Figure 4.2.11.7. Again, these are for jet Reynolds numbers of 10,000, 15,000, and 20,000, where each of the sixteen jets is the same flow rate. In these images, flow is from left to right, the left end of the channel being the plugged end. In each test result, the second impingement jet is seen to provide the strongest heat transfer surface response, which is essentially that of a free jet without crossflow or other encumbrance. In general, impingement jet Nusselt number in the peak region can be expressed by $Nu = 0.18*Re^{0.7}$, though specific cases vary. This relationship would lead to present impingement heat transfer coefficients of about 20.5, 27.2, and 33.2 Btu/hr/ft2/F, which agree quite well with the results on the second jet. Subsequent impingement jet heat transfer is reduced downstream as the crossflow effects build from total channel flow rate. At the end of the channel, the flow is nearly that of pure channel flow, with little impingement character.

Figure 4.2.11.8 shows the same impingement jet row with the broken chevron turbulated arrangement described earlier. Because the chevron strips are of square cross section 0.25 x 0.25 inches, and spacing of 2.5 inches, their relative positioning is the same for each impingement jet (the relative geometry is repeated along the channel length). In the present tests, each jet axis is aligned with the center region containing two opposed turbulator strip ends. This is the most disruptive region for jet impingement in this case. A comparison of Figures 4.2.11.7 and 4.2.11.8 appear to indicate a substantial decrease in overall heat transfer with the chevron strips, but this is misleading in two respects. First, the turbulators have not been masked out in these results, leaving very low heat transfer strips in the images that do not exist in reality. Second, since the turbulators are not thermally participating in this model, they do not show the significant surface area and fin effect addition to heat transfer that a full metallic model would indicate. Together, these two factors will replace 10% very low heat transfer with about 25% high heat transfer in the results. This will put the chevron strip impingement heat transfer on par with that of the smooth surface. In the end, this is not an improvement. It may be speculated that the initial choice of relative impingement location on the turbulators has badly disrupted any potential synergy with the dual swirl intent of the angled strips. It is also likely that some impingement angle for the jets will help in the interaction with the turbulator strips.

While the foregoing tests represent one limit of the flow model for a cooling passage, the other limit is that of purely convective flow without impingement or film extraction. Figure 4.2.11.6 showed the potential of the geometry at very high Reynolds number channel flows. Under such high Reynolds number conditions the heat transfer enhancement factors are only about 1.6 relative to a smooth channel. Figure 4.2.11.9 shows the heat transfer distributions for more moderate Reynolds numbers that represent air-cooled, open-circuit airfoil designs. Overall, the average channel heat transfer coefficient is about the same as that for the impingement cooled version with increasing crossflow. Looking at the middle result for channel flow Reynolds number of 53,000, a standard fully developed channel heat transfer coefficient in this model would be about 6 Btu/hr/ft2/F (per the Dittus-Boelter correlation). The broken chevron configuration results in about 13 Btu/hr/ft2/F in the fully developed region after three or four repeated chevron strip pairs. Keeping in mind that the turbulators are again not thermally active surfaces in this test model, the corrected heat transfer coefficient enhancement will be about 2.5. This is certainly very much in line with expectations for high performance turbulators in channel flows.

## Implications for Active Cooling Control

Like the external airfoil dimples, the active cooling control implications of using broken chevron strip turbulation in a non-square passage of an airfoil are not direct. An alternate cooling configuration of this type can be used to lessen the sensitivity of the cooling circuit to changes in flow rates imposed by active control.

## Conclusions

The use of a dual swirl type cooling passage configuration, as imposed by repeated sets of broken and staggered chevron strips, has shown no definitive benefits in tests of impingement cooling or convective cooling.

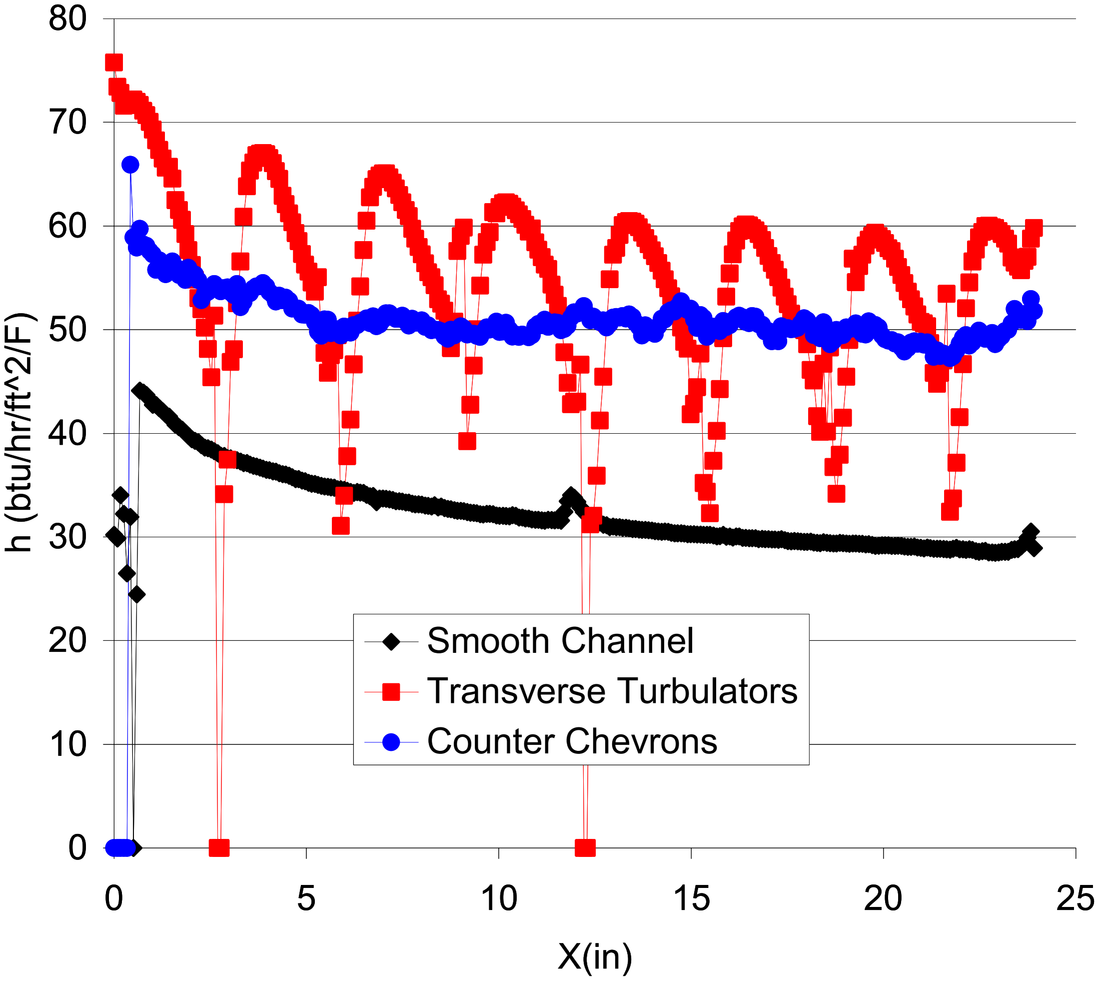

Figure 4.2.11.6 Prior High Reynolds Number Dual Swirl Channel Heat Transfer

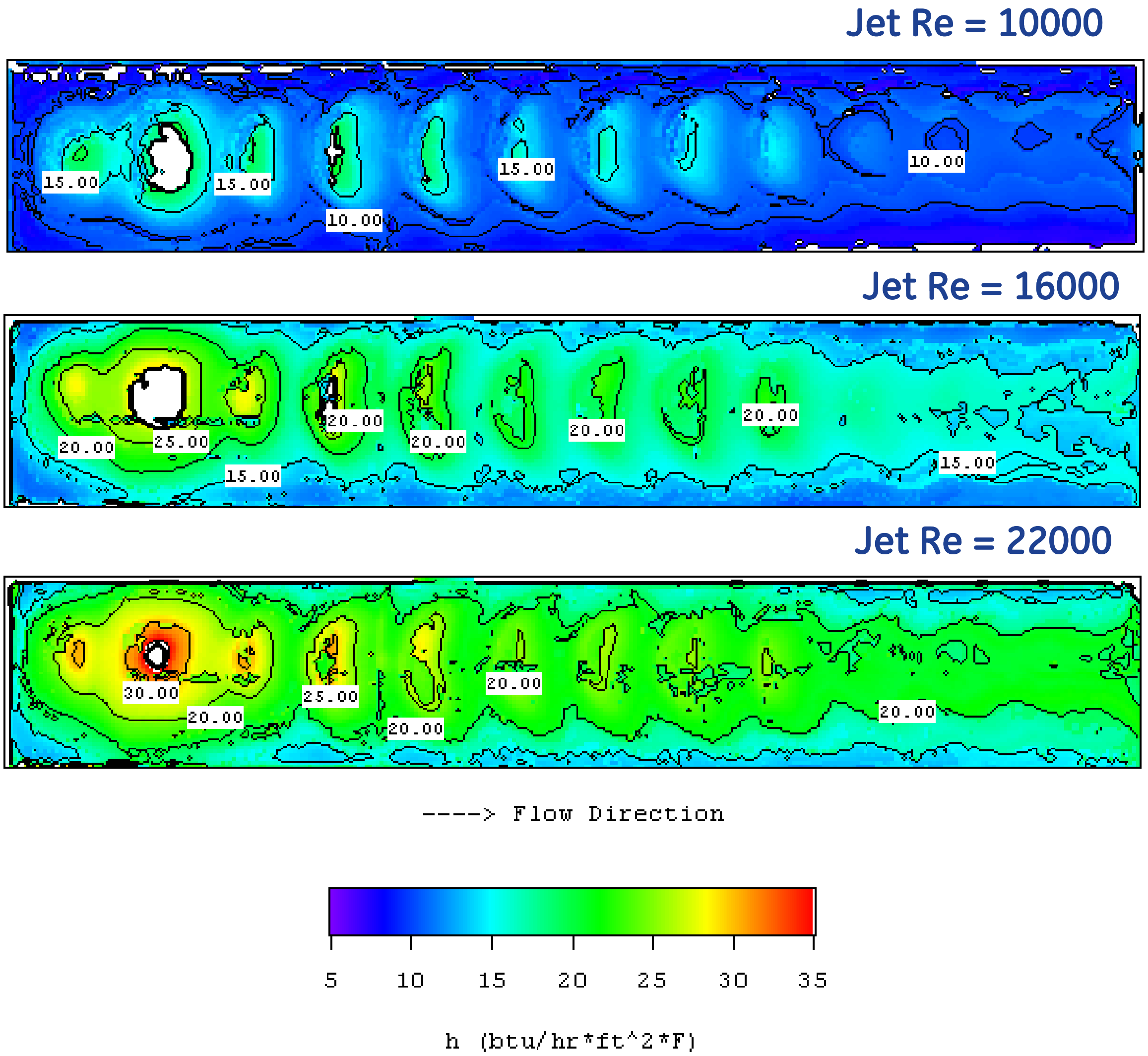

Figure 4.2.11.13 Smooth Channel Impingement with Jet Reynolds Numbers of 10000, 16000, and 22000.

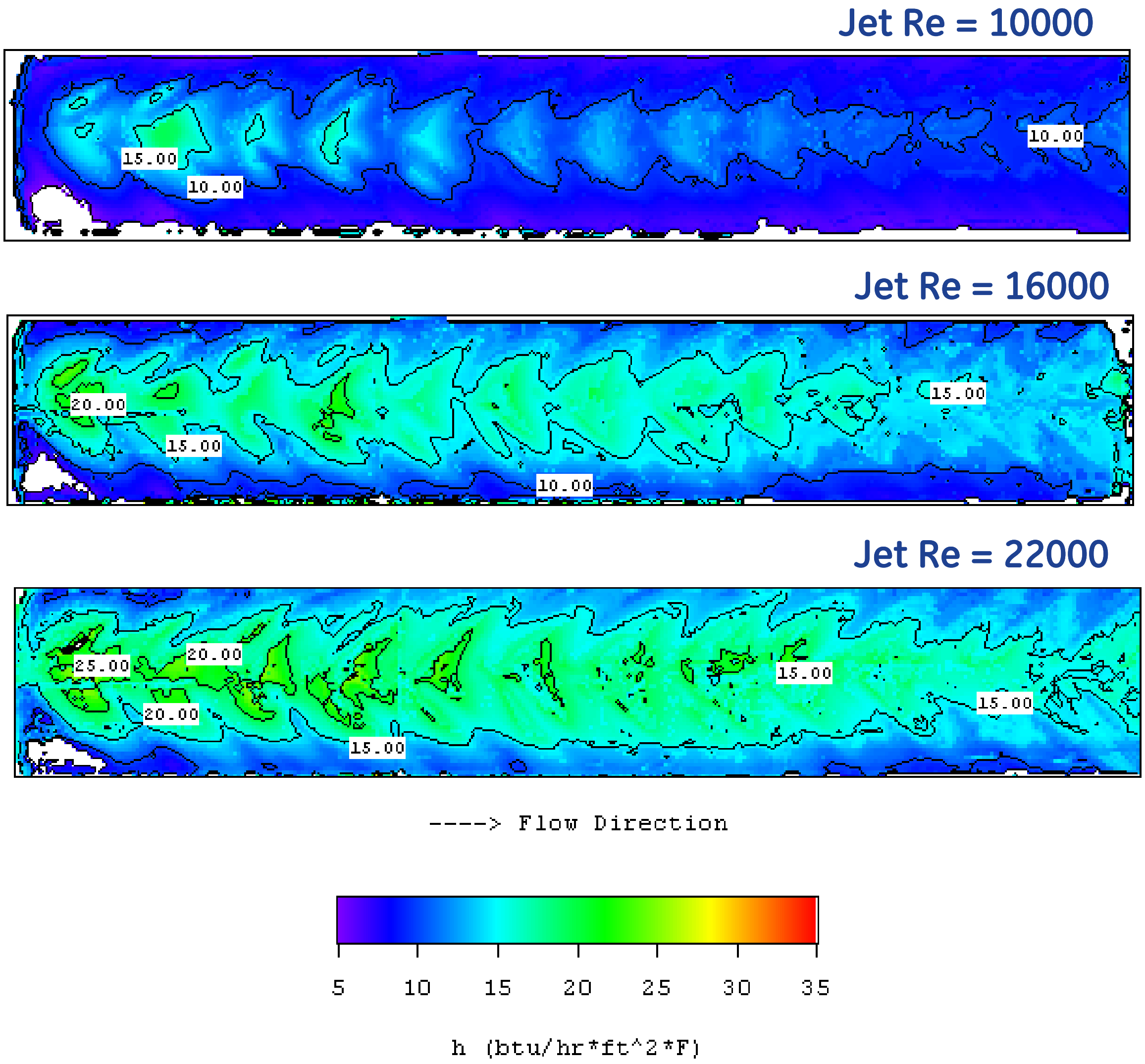

Figure 4.2.11.14 Impingement onto Chevron Surface

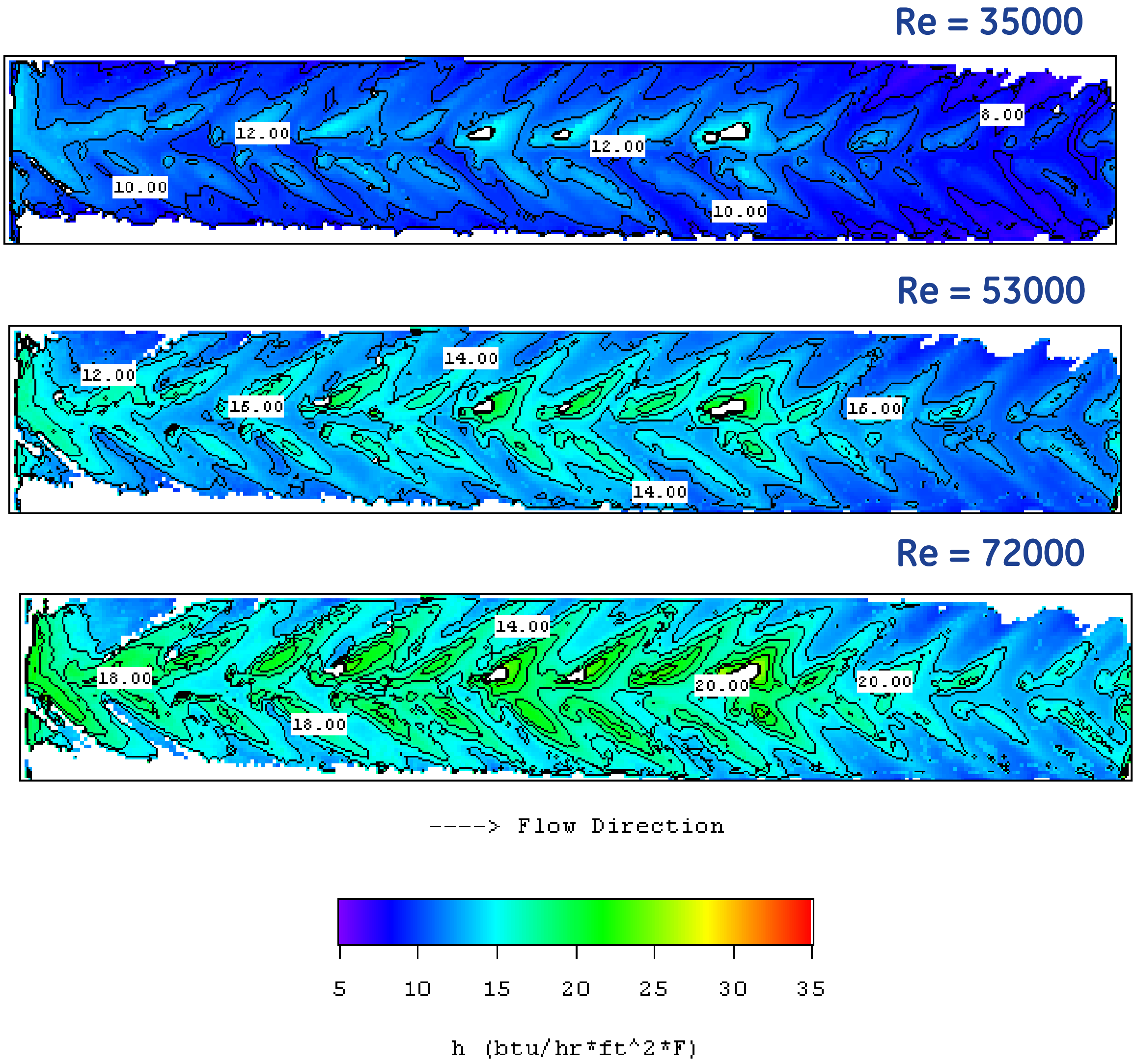

Figure 4.2.11.15 Channel Flow over Broken Chevrons for Reynolds Numbers of 35000, 53000, and 72000

## Subtask 4.2.12 High-Temperature Imaging Pyrometry

### Objectives

The objective is to improve optical high-temperature engine diagnostic capability. GEGR will conduct a detailed analysis of optical properties of thermal barrier coated (TBC) blades.

### Technical Progress

Development of advanced turbine blade cooling requires having advanced methods to measure the blade temperatures during operation. Validating turbine airfoil temperatures is a critical, yet challenging task for any gas turbine engine manufacturer. Temperature measurements of this kind are difficult to obtain due to the rotating geometry, and high thermal and structural loads. Optical temperature measurements, such as IR pyrometers, are a preferred method for making turbine blade temperature measurements. IR Pyrometry non-intrusively measures the temperature and temperature profile on each blade of an entire rotor stage.

Current on-engine pyrometry measurements on thermal barrier coated (TBC) surfaces show increased uncertainties relative to measurements on metallic surfaces. Standard TBC is translucent in the 1-5 $\mu$m region and depending on the optical properties of TBC, radiation emanating from the coated blade is the result of different effects. The metal emitted radiation can be attenuated by absorption and scattering effects while it can be enhanced by emission and in-scattering of TBC. One possible alternative is the use of long wavelength (8-12$\mu$m) pyrometry for TBC surface temperature measurement. At long wavelengths, the TBC is opaque and behaves as a blackbody. However, at these wavelengths, gas emission/absorption is important and one must account for its contribution. This requires knowledge of the pressure and temperature profiles between the TBC target and the pyrometer. Though still useful for component test applications outside a high-pressure engine environment, this makes the long wavelength pyrometry very dependent on the analytical gas model in the high pressure turbine environment. Moreover, the intensity is less sensitive to temperature variation at these wavelengths. Literature on short and long wavelength data taken on real gas turbines were reviewed. Conclusions from these works indicate that airfoil temperature data (corrected for all effects discussed above) at the short wavelength compares much better with expected temperature profiles. Hence, it is anticipated that measurements made at the short wavelength are more accurate than at the longer wavelengths.

At short wavelength around 1.6 $\mu$m, gas emissions are negligible. Preliminary results show that Electron Beam Physical-Vapor-Deposition (EB-PVD) yttria-stablized zirconia (YSZ) coating is totally scattering (not absorbing). The detected radiation is emitted by the surface metal only after being scattered by TBC. By measuring the effective emissivity, one can estimate the metal temperature. This effective emissivity is highly dependent on the coating thickness, which requires a uniform coating over the blade surface or thickness measurement map to achieve good accuracy. In addition, evolution of coating optical properties with turbine engine exposure needs to be considered. Accumulation of dirt on the surface tends to increase the emissivity where the radiation emanates now from TBC surface only. Due to these transition at short wavelength, multi-color pyrometry can be a suitable alternative. To realize this, we need to have a better understanding of the optical properties of TBCs (emissivity, phase function at the various wavelengths of interests) and analyze the radiative transfer within TBC.

### 4.2.12.1 Optical properties of TBCs at room temperature

Usually, TBC specimens are applied on typical opaque airfoil coupons; but in order to measure the optical properties, it is advantageous to apply them to a transparent material. Specimens of TBC have been applied to sapphire and a few samples have been obtained for initial trial experiments.

Figure 4.2.12.1.1 shows the set-up used to measure the diffuse reflectance and transmittance at ambient temperature. The sample beam leaving the integrating sphere is directed to an infrared spectrometer with a spectral range of 0.5 μm – 2.5 μm. Figure 4.2.12.1.2 shows the results for a standard EB-PVD coating. The sample is not emitting in the displayed spectral range. The coating is totally scattering. In this situation, multi-color pyrometry can account for the TBC scattering effect to obtain the metal temperature.

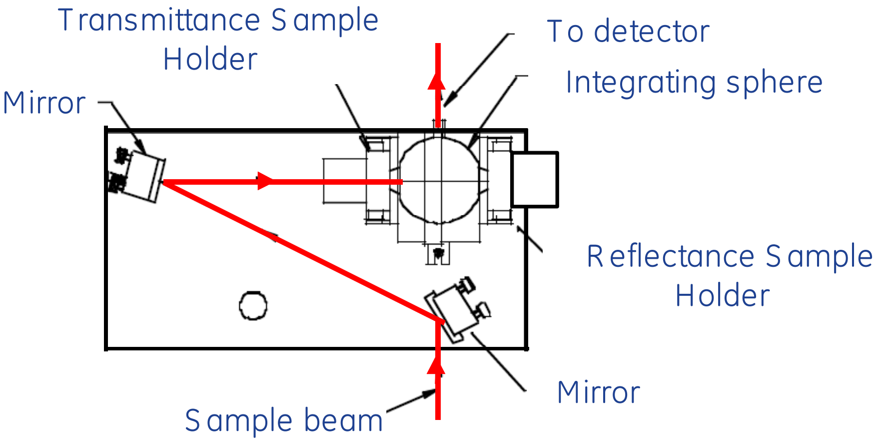

Figure 4.2.12.1.1. Experimental set up for transmittance and reflectance measurements

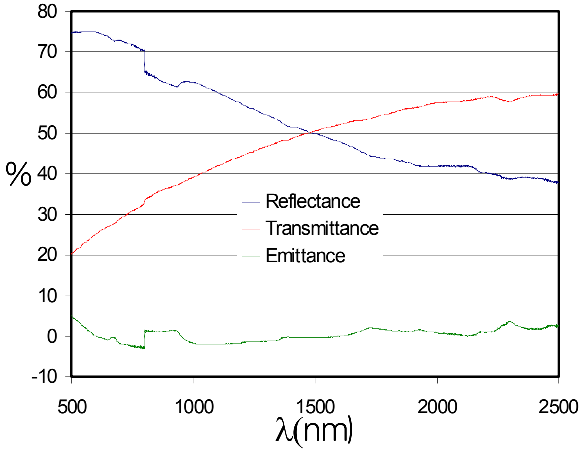

Figure 4.2.12.1.2. Reflectance, transmittance and emittance measurement

Figure 4.2.12.1.3 shows a comparison between the diffuse and the total reflectance. A difference of 7% is observed. This means that the coating is either specularly reflecting or highly forward scattering. By analyzing the TBC sample, it was observed that the TBC is not specularly reflecting. The coating is then highly forward scattering which can be attributed to the columnar structure of the EB-PVD coating. This quality improves the spatial resolution and reduces the effect of the thickness on the effective emissivity as will be shown next section.

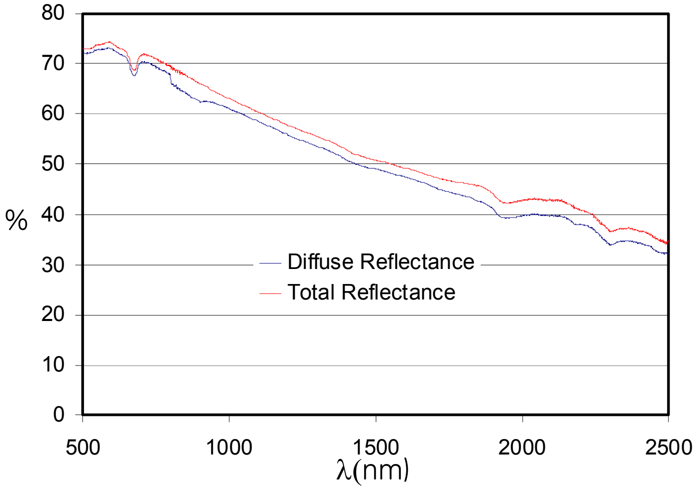

Figure 4.2.12.1.3. Comparison between diffuse and total reflectance

Other measurements were done on free standing TBC. They were coated on carbon. After heating them in an oven for 8 hours at around 1000$^o$F the carbon was burnt out. Total transmittance and total reflectance were measured for free standing TBC using an integrating sphere. These measurements were used to calculate the emissivity of TBC at room temperature. The results are shown in Figure 4.2.12.1.4.

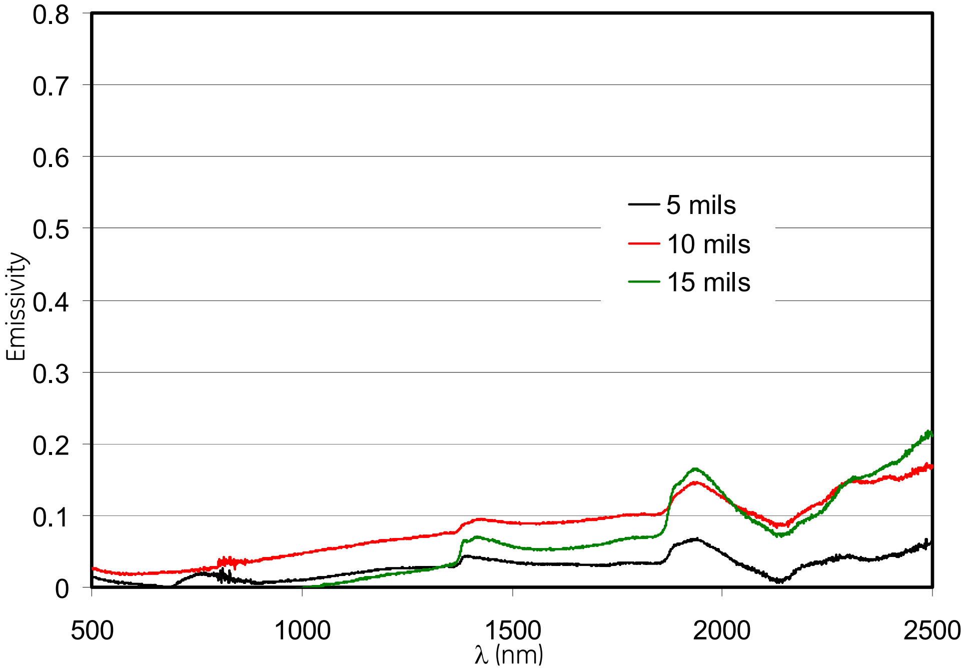

Figure 4.2.12.1.4 Emissivity of EB-PVD thermal barrier coating at different thickness at room temperature

### 4.2.12.2 Optical properties of TBCs at high temperature

TBC coated on Sapphire substrate

The emissivity measurements at high temperature were conducted using a $CO_2$ laser as a heat source. The $CO_2$ operates at wavelength of 10.6 μm where TBC is highly absorbing. At this wavelength, 95% of the incident energy is absorbed by the coating to generate the increase in temperature. The experimental set-up is shown in Figure 4.2.12.1.5. The $CO_2$ laser is incident on the sample at an angle of 45 degrees and the optical system is collecting radiation at a normal direction. The laser spot on the target has a diameter of 4 mm. A Zeiss spectrometer is used to analyze the data in the spectral range 0.9 μm-1.7 μm.

Figure 4.2.12.1.6 shows the radiances measured for 3 plasma sprayed TBC samples (not clean) and one EB-PVD sample. No emission was observed for the EB-PVD sample in the spectral range of interest. The emission observed for the plasma sprayed samples is due to the bond coat. Multicolor pyrometry was used to estimate the temperature of the surface. The average temperature is around 2400°F. It was not possible to obtain the surface temperature for the EB-PVD sample since no signal was detected. This means that at high temperature, the EB-PVD TBC is totally scattering. The detected radiation is emitted by the surface metal only after being scattered by TBC. Thus, the apparent emissivity of the surface airfoil depends on the metal emissivity, scattering coefficient, the scattering phase function and the coating thickness and surface deposition. However, due to the high temperature gradient within the sample, cracking was observed after few seconds of irradiation. We need to do more measurements to confirm our conclusion. (Note: Multi-color pyrometer was used in this case assuming a grey surface over the wavelength region. Since this assumption not entirety correct, this plot is only used to show the conclusion reached above).

<u>Free- standing TBC</u>

Some new freestanding specimens were received from Jeff Eldridge (NASA) and new tests were conducted. Figure 4.2.12.1.7 shows the radiance measured for a 15 mil thick EB-PVD TBC sample for two configurations. One where the sample is sitting on a piece of metal (stainless steel) and one where the sample is free. For the first case, the metal serves as a heat sink and most of radiative heat is wasted by conduction to the metal. That’s why the radiance signal is lower when compared to the free standingTBC sample. Multicolor pyrometry was used to calculate both temperature and emissivity. For free standing TBC, the emissivity was about 0.04 and the temperature was about 1498°C (2728°F). For the TBC placed on a metal, the calculated emissivity was about 0.11 with a temperature of 1087°C (1989°F). This is due to the contribution of metal emissivity, which was attenuated by TBC.

This means that at high temperature, the EB-PVD TBC is mainly scattering. The detected radiation is emitted by the surface metal only after being scattered by TBC. Thus, the apparent emissivity of the surface airfoil depends on the metal emissivity, scattering coefficient, the scattering phase function and the coating thickness.

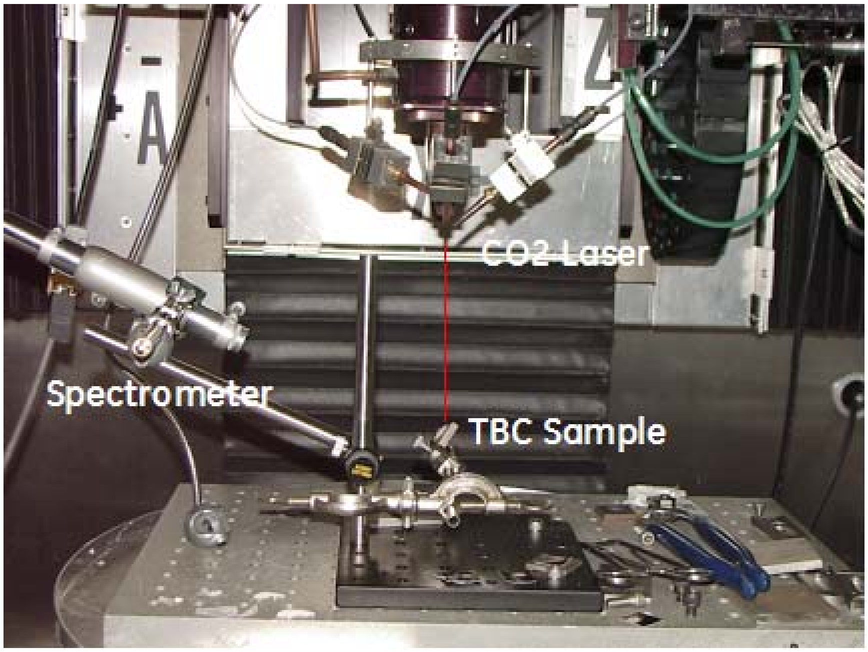

Figure 4.2.12.1.5. Experimental set up for emissivity measurement using a $CO_2$ laser

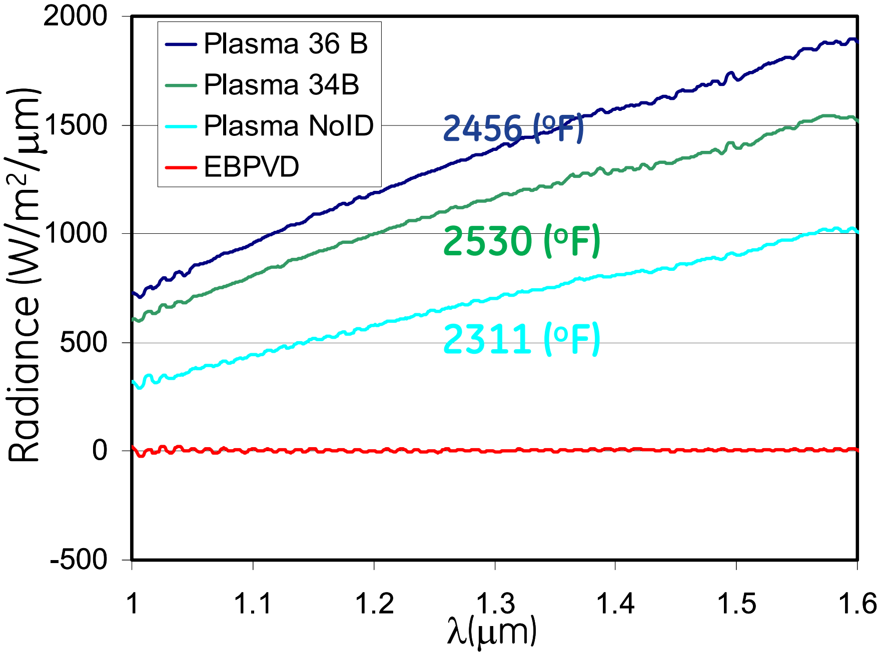

Figure 4.2.12.1.6. Radiances of TBC samples

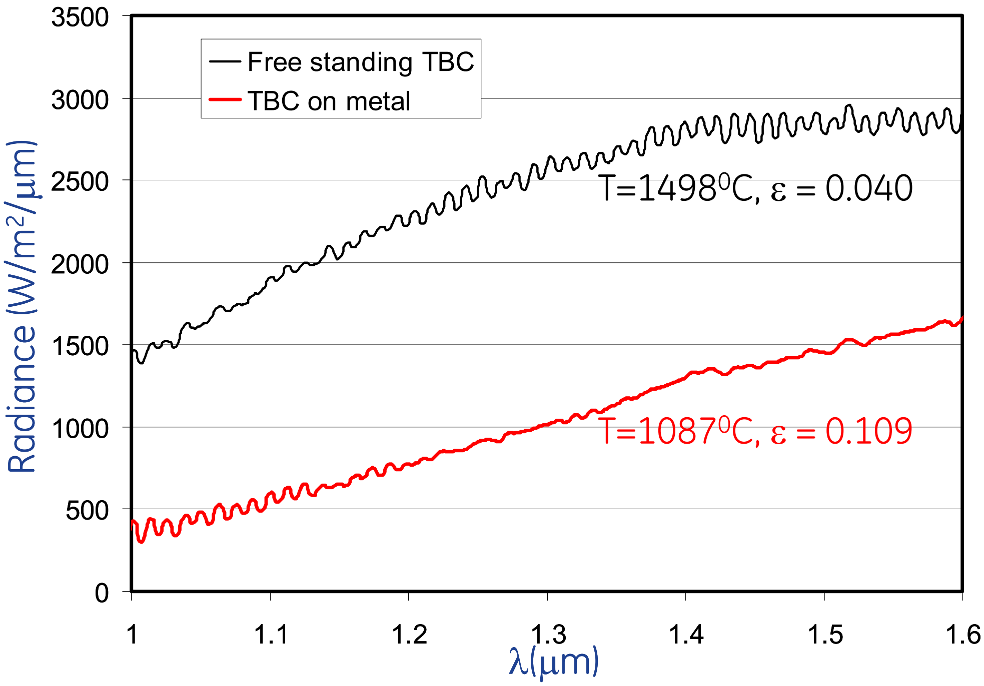

Figure 4.2.12.1.7. Radiances of TBC samples

### 4.2.12.3 Radiative Physics in TBCs

A numerical model was developed to solve the radiative transfer equation (RTE) to analyze the effect of the optical properties and the thickness on the effective measured emissivity. The radiative transfer equation is shown below:

$$\mu \frac{\partial I(x, \mathbf{\Omega})}{\partial x} = -(\sigma + \kappa)\, I(x, \mathbf{\Omega}) + \kappa I_b(x) + \frac{\sigma}{4\pi} \int_{4\pi} P(\mathbf{\Omega}, \mathbf{\Omega}')\, I(x, \mathbf{\Omega}')\, d\, \mathbf{\Omega}' \tag{4.2.12.1.1}$$

where $I$ is the radiance, $P$ is the scattering phase function, $\kappa$ and $\sigma$ are the absorption and the scattering coefficient respectively.

By solving the RTE, one can obtain the radiance emerging from the TBC and thus evaluate the apparent emissivity. Figure 4.2.12.1.8 shows the apparent emissivity as function of thickness for different types of scattering (isotropic scattering for g=0 and highly forward scattering for g=0.95). It is seen that for a highly forward scattering medium, the thickness has an effect less important than for an isotropic medium. This variation means that to get accurate temperature measurement, emissivity needs to be measured at different thicknesses. Unfortunately, this is far from being a controllable variable. The thickness is not known with good accuracy especially on actual turbine parts.

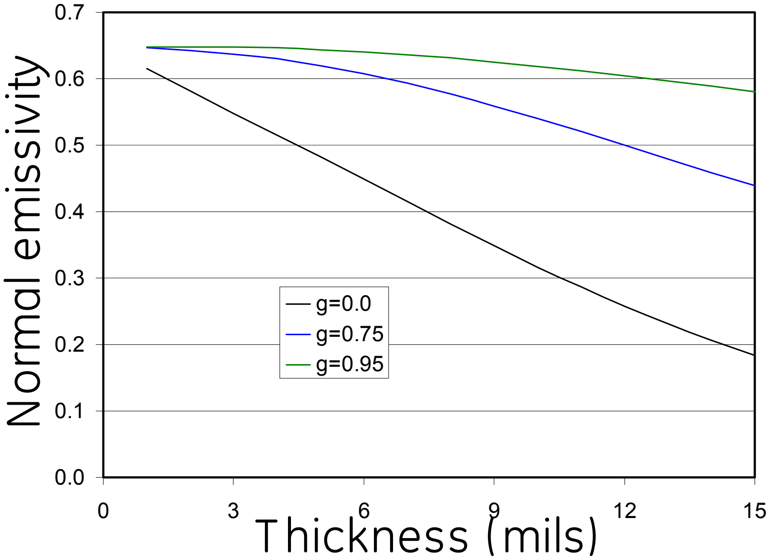

Figure 4.2.12.1.8. Variation of emissivity with thickness and scattering phase function

To evaluate the effect of the variation of the TBC thickness on the sensed temperature, an effective emissivity was calculated for a sample with a thickness of 5 mils and used to obtain the temperature for samples with different thicknesses using one-color pyrometry. Figure 4.2.12.1.9 shows the deviation from the true temperature for different thicknesses were reflections from surrounding was neglected.

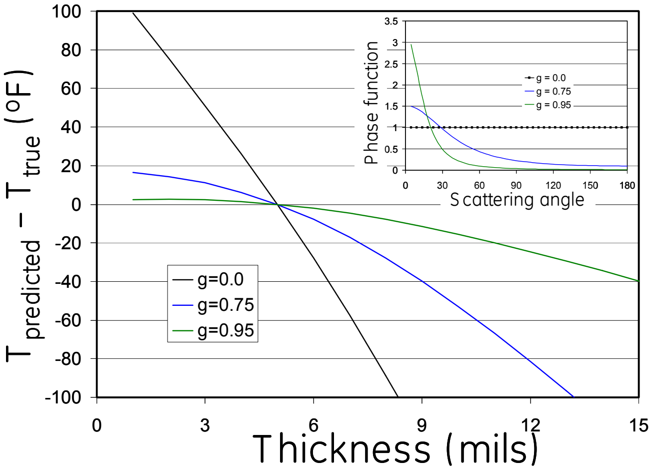

Figure 4.2.12.1.9. Error temperature variation with thickness

Considering reflections from the surrounding helps to reduce the effect of the thickness variation.

The detected signal measured by the pyrometer is due to the airfoil emission and to the reflection from the surrounding hot areas. This detected signal can be given as:

$$I^{meas} = \varepsilon(\lambda) I_b(T,\lambda) + [1-\varepsilon(\lambda)] * I^{surrd}(T_{surrd},\lambda) \qquad (4.2.12.1.2)$$

This equation shows that the reflected radiation from the surrounding can help to compensate for errors in emissivity. For instance, for a case where the target has the same apparent temperature as the surrounding, the emissivity has no effect on the target temperature. Also, it can be seen that errors in emissivity generates higher errors in temperature for a cold surrounding than for a hot surrounding. The case with no reflection from surrounding shows large error as shown in 4.2.12.1.10 for g=0.95.

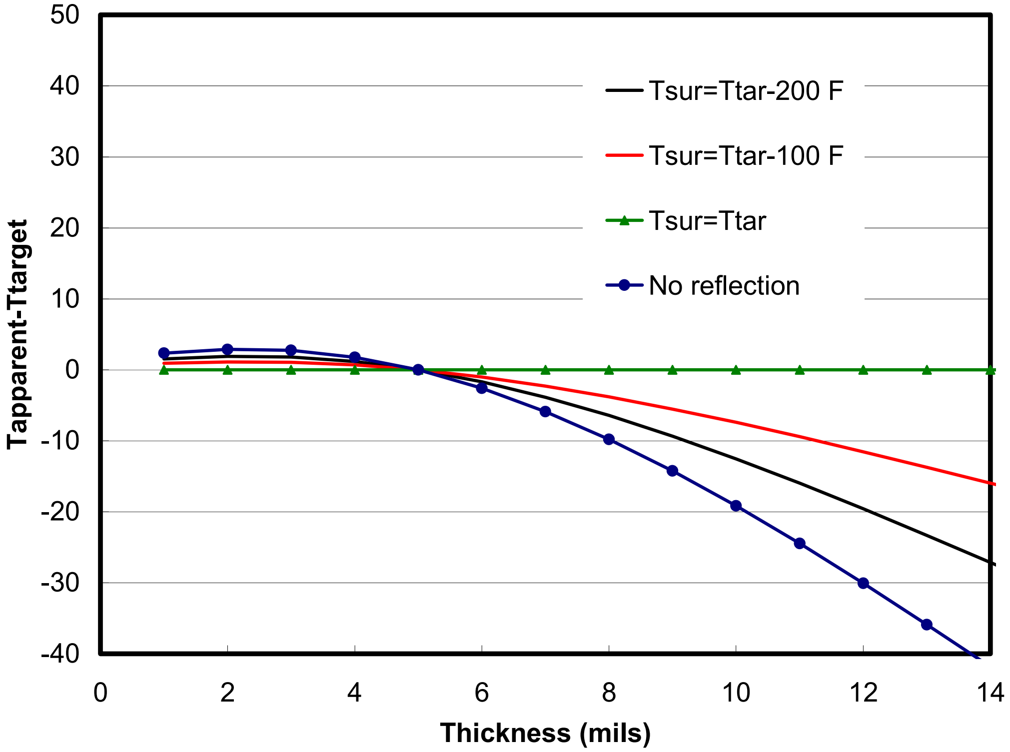

Figure 4.2.12.1.10. Error temperature variation with thickness

As an alternative, multi-color pyrometry may be a solution to overcome the effect of the emissivity variation and TBC thickness. Different multi-color pyrometry algorithms were developed. It showed that using a spectral range of 0.5 $\mu$m –2.5 $\mu$m (where the gas emission is negligible) an accuracy of ± 25 $^{o}$F can be achieved. Preliminary multi-color pyrometer measurement on TBC showed good agreement with thermocouple measurements at the surface metal.

A qualitative comparison was done between a prediction model based on the solution of the radiative transfer equation and some collected experimental measurement for total reflectance. The total reflectance from a one dimensional TBC slab is calculated and displayed in Figure 4.2.12.1.11 for different asymmetry factors g (isotropic scattering for g=0 and highly forward scattering for g=0.995).

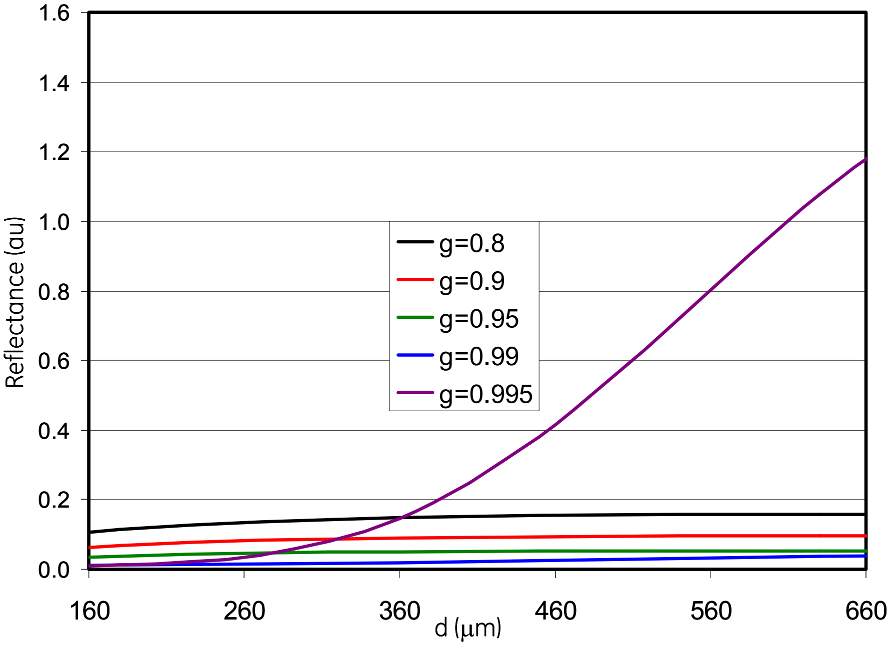

Figure 4.2.12.1.11. Variation of predicted total reflectance with sample thickness

A qualitative comparison between the predicted and the measured reflectance (Figure 4.2.12.1.12) shows that the experimental one has the same shape as the one with higher g value (g=0.995). This means that TBC is highly forward scattering and thus, as previously reported, the effect of thickness on emissivity and on the sensed temperature is not significant.

As was shown in some results at high temperature, TBC has a very low emissivity (about 0.05) at around 1.6 μm. Simulations were run by assuming an equivalent absorption coefficient for TBC (k=212 $m^{-1}$) and compared the contribution of TBC emission signal to the metal signal. This is shown in Figure 4.2.12.1.13 . For a 5 mils thickness, 95% of the emission is from the metal surface. This means that for fresh TBC most of the radiation is emanating from bound coat surface.

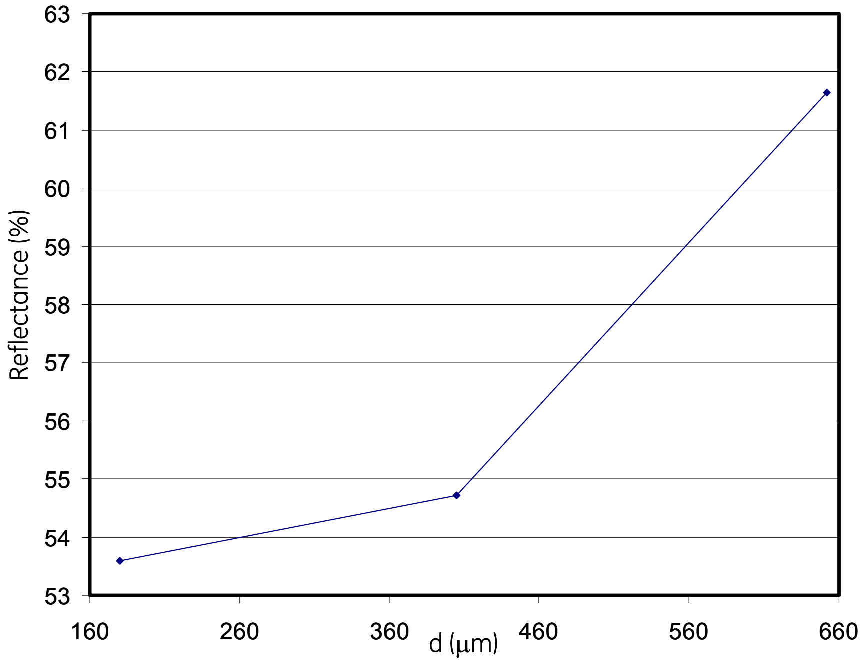

Figure 4.2.12.1.12. Variation of measured total reflectance with sample thickness

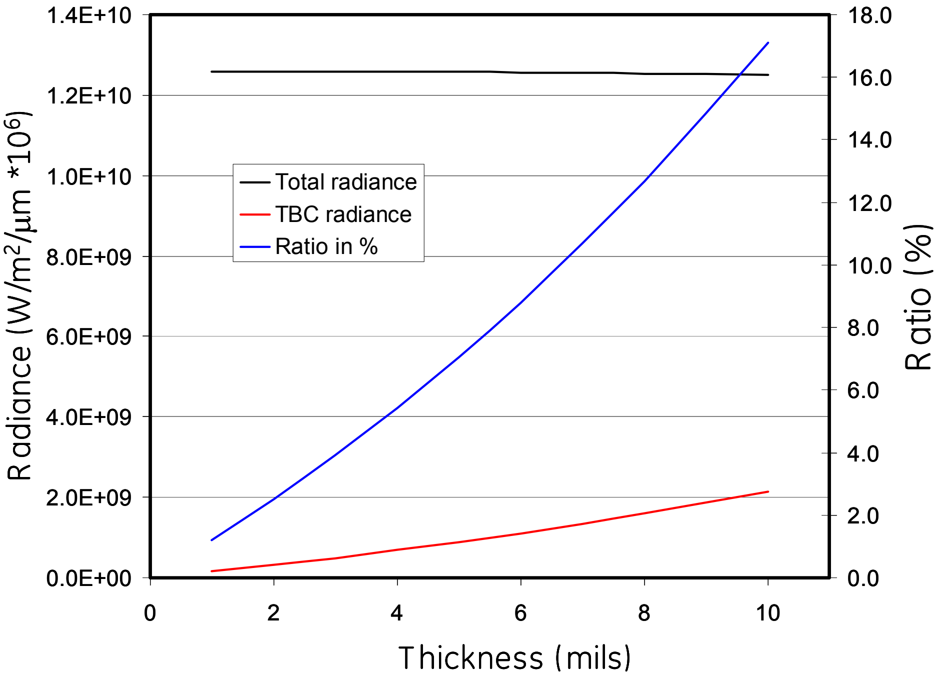

Figure 4.2.12.1.13. Comparison between metal and TBC contributions

### 4.2.12.4 Determination of sensed points for TBC airfoils.

Recent attempts have been made to determine the sensed point for TBC airfoils with different age. As shown in Figure 4.2.12.1.14 a thermocouple was welded to the bound coat to measure the metal temperature while a long wavelength pyrometer was measuring TBC surface temperature. A multicolor pyrometer was used to compare with the two mentioned measurements and thus determine the sensed point obtained by the MC.

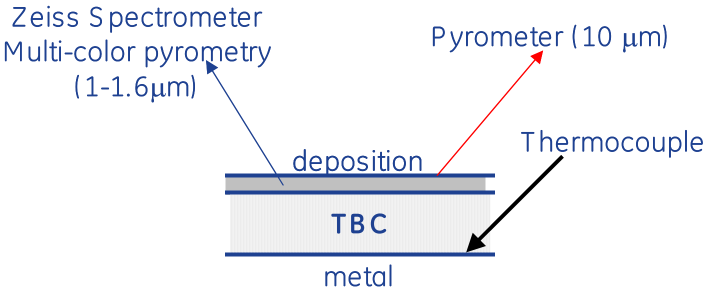

4.2.12.1.14. Sensing point determination

The experimental set up is shown in Fig. 4.2.12.1.15 where the airfoil is heated by an induction oven.

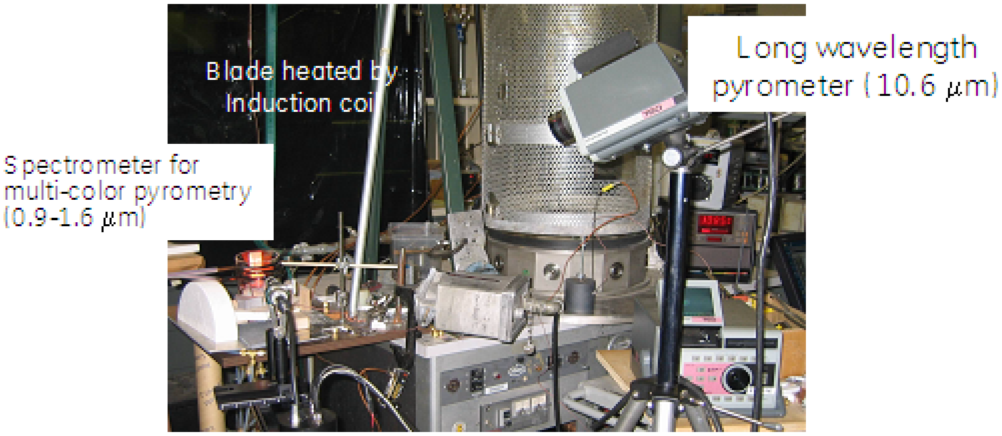

Fig. 4.2.12.1.15. Experimental set-up to determine the sensed point

Fig. 4.2.12.1.16 shows a comparison between the three methods of measurements. Long wavelength (LW) pyrometer and thermocouple show comparable temperatures while the multicolor (MC) pyrometer shows lower temperature. It was expected to have the temperature obtained by the MC pyrometer in the interval defined respectively by the LW pyrometry temperature and thermocouple temperature. These were preliminary measurements. Further efforts are needed to calibrate the LW pyrometer and to increase the spatial resolution of the MC pyrometer in order to gain the sensed point with good accuracy.

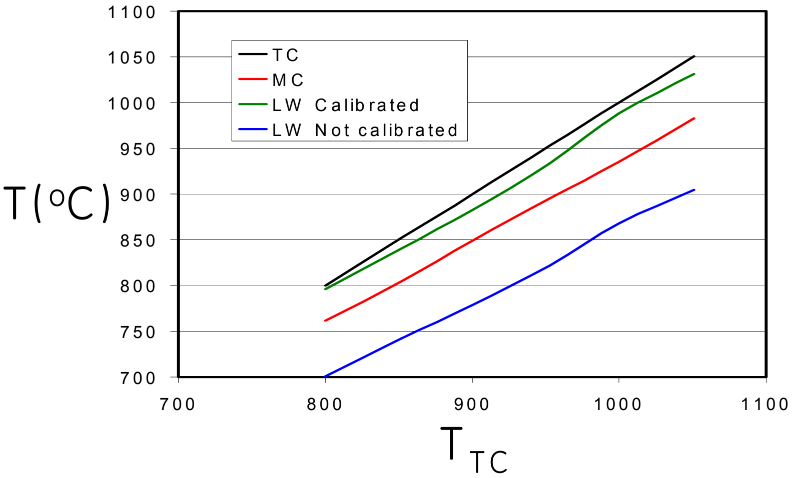

Fig. 4.2.12.1.16 Comparison between thermocouple, long wavelength pyrometer and multicolor pyrometer

## Conclusions

In this project, an analysis of radiative physics in TBC airfoils was pursued.

It was shown that TBC is translucent in the 1-5 μm region. The Electron Beam Physical-Vapor-Deposition (EB-PVD) coating is highly scattering (not absorbing). For fresh blades, the detected radiation is emitted by the surface metal only after being scattered by TBC. By measuring the effective emissivity, one can estimate the metal temperature. However, this effective emissivity is highly dependent on the coating thickness, which requires a uniform coating on the blade surface to achieve good accuracy. The effect of thickness variation on the pyrometer accuracy was shown. A highly forward scattering coating will have less error than an isotropic scattering one. The reflection from the surrounding can help to reduce this error. Multi-color pyrometry can be a suitable alternative to the current detector capabilities potentially eliminating complications associated with TBCs.

In addition, evolution of coating optical properties with turbine engine exposure has an effect on optical properties. Accumulation of dirt on the surface may increase the emissivity where the radiation may emanate now from TBC volume and surface. In our recent efforts, determination of sensed point was executed for different blades with different lives. This is a continuing work as more improvements are needed for our experimental rig. The columnar structure and the directional effects of the coatings are of a big interest, but was not considered in the optical properties measurements under this program and will be pursue in a following program.

### 4.2.13 Complex Core Prototype Producibility Assessment

#### 4.2.13.1 – Objective & technical approach

The goal of this subtask effort is to lay the foundation to determine the practicality of manufacturing the sorts of complex core geometries that have emerged from the main design tasks. In short, will it be possible to build what can the airfoil design community can imagine and create in the CAD environment? The results of the major airfoil feature design, performance simulation and thermal characterization tasks were advanced to such a promising extent that it was appropriate to begin to consider the issues associated with manufacturing such airfoils, which must first address the need to manufacture the complex ceramic cores that will be required in future casting trials. Prior to considering the mass production casting of actual in-service hardware, it is desired to test and evaluate several potential design alternatives, and the ability to rapidly manufacture casting cores for different designs is a key enabler of this phase of the study. This subtask was initiated in the final few months of the Phase II effort with the objective of identifying the most promising option (or options) for rapidly prototyping a series of casting cores of different geometries. This effort provides a head start on addressing challenging manufacturing issues for future phases of the program.

The approach followed in this subtask focused on currently available rapid prototyping (or solid freeform fabrication) methods for direct layer-by-layer manufacture of ceramic parts without the need for a support mold of any type. Rapid prototyping represents significant advantages with respect to turnaround time and economy when compared with methods such as injection molding that are used for mass production of ceramic casting cores. Rapid prototyping offers the potential to produce parts within a few days of completing the CAD model, so it would be possible consider many different design concepts, as well as subtle iterations on those concepts, in the several months it would take to produce a single core using conventional processes.

From the broad range of available rapid prototyping or solid freeform fabrication methods, this effort has concentrated on reviewing those that have been employed successfully for ceramic applications, including laminated layer manufacturing, 3D printing, stereolithography and laser sintering. From this evaluation, direct laser sintering emerged as a leading candidate for net shape manufacturing of advanced casting cores. Given the short time frame of this subtask, with only a few months available at the end of the program, the choice was made to focus all efforts on a direct laser sintering process. Previous efforts at GE had established the promise of this process for other ceramics applications, supporting the conclusion that direct laser sintering presented the most capable option currently available.

#### 4.2.13.2 – Background

Rapid Prototyping:

Rapid prototyping (RP), also referred to as solid freeform fabrication (SFF), has developed into a broad field with a myriad of commercial systems and services are available for many different methods, materials and applications. The RP community also is focusing beyond strictly prototyping applications to the realm of ‘rapid manufacturing’, deploying the various SFF methods for small lot manufacturing runs. Entire texts have been devoted to rapid prototyping, so an exhaustive review of the subject is beyond the scope of this discussion. However, it is useful to note a few unifying themes that are applicable to any RP method.

The principal advantage of any rapid prototyping method is the capability to manufacture parts of complex geometry directly from the CAD solid model, without the need for additional tooling. This is accomplished by building the workpiece up, in an ‘additive’ manner, one layer at a time, starting from a substrate that provides the support for creating the first layer.

It is worthwhile to preface this discussion with a summary of the major process steps that are generic to any SFF method. The first step is to provide (or create) the 3D CAD solid model of the part to be manufactured. The solid model is then processed via the appropriate software to reproduce the part geometry as a stack of parallel 2.5D layers, each representing a slice through the part at a particular build height. This collection of electronic slices comprises the input geometry to the RP machine to determine the orientation of the successive layers as the part is built. The RP machine deposits the first layer of the build material and then fuses, or solidifies this first layer over a region corresponding to the definition of the 1st slice in the processed CAD model. The second layer of build material is then distributed on top of the first, and the RP machine solidifies the material in this layer and fuses it to the first layer. These steps are repeated over and over, building the part up layer by layer until the final slice in the part geometry is deposited and fused. Once the part is completed, there is often some additional post-processing required to improve the surface finish, reduce internal porosity, or otherwise improve the part condition beyond the as-deposited case.

For commercial RP processes, the slicing of the CAD geometry into appropriate layers generally has been automated and integrated into the software that is packaged with a particular machine. The layer thickness used to build the part is the key manufacturing parameter, in turn determining the parameter settings for the machine operation necessary to produce that thickness. Maintaining uniform thickness within a given layer and accurately depositing the thickness specified in the slice geometry are essential for reliable reproduction of the desired geometry. In general, minimizing the layer thickness will minimize the ‘stair-stepping’ effect evident on the part surface to produce the best surface finish, so layer thicknesses are often kept to < 0.010” in high resolution RP processes. This improved resolution comes at the expense of longer total build times associated with using more slices to represent the part geometry.

The nature of the RP process, involving the need to deliver or distribute the build material in a layered form and subsequently bond successive layers to one another, places some restrictions on the form and composition of practical build materials. Options that have been developed for commercial processes include powders, liquids (polymer resins), and thin solid foils. Various polymers in either liquid or powder form have seen the broadest deployment.

Processes using various metals and ceramics in powder form are also available, and are of great technical significance since they expand the options for manufacturing functional engineering components.

Specific to ceramic materials that are the focus of this effort, several RP processes have been previously demonstrated for various applications. Those methods considered for this effort differ according to solidification mechanism, and include laminated object manufacturing, 3D printing, stereolithography, and laser sintering. Some features of these various techniques are included for reference.

Laminated Layer Manufacturing:

Laminated layer manufacturing is an RP process that operates by gluing together successive foil layers that are cut in patterns that match the individual layers created in the slicing of the CAD model. Paper or plastic foils coated with thermally activated adhesive are the typical build materials, such that successive layers may be bonded together with a hot rolling or hot pressing operation. Laminated layer manufacturing has also been applied to ceramic fabrication using tape-cast ceramic sheets [Cawley, et al. – 1995, Cawley, et al. – 1995, Klosterman, et al. – 1995, Klosterman, et al. – 1996, Liu, et al. – 1996]. A post-build furnace sintering step is necessary to consolidate the finished part from the green state.

3D Printing:

Three dimensional printing is a RP method that utilizes ink-jet printing to deposit the geometry for each layer in the part being manufactured. The 3D printing process was developed in the early 1990’s [Cima, et al.–1991, Sachs, et al.-1992] and has since been applied to a number of materials, including metals and ceramics. The 3D printing process builds the part in a powder bed (a build chamber filled with the particular build material in powder form). The layer formation sequence begins with the deposition of a fresh layer of loose powder across the build chamber. A roller is then swept across the build chamber to spread and level the powder layer to ensure uniform layer thickness. Finally, an ink-jet print head ‘prints’ a coating of liquid binder over the powder surface according to the pattern defined by the particular layer. The binder acts to fuse the powder in that layer and bond it to the preceding layer. As with any of the powder bed SFF methods, the unbound powder surrounds the part as it builds, forming an effective support structure. When the build is finished, the ‘green’ part undergoes a furnace sintering step while still surrounded by the unbound powder. The sintering step burns off the binder to create a strong bond between the powder layers, after which the unbound powder is cleaned away, leaving a functional engineering component.

3DP is currently licensed to several companies for various commercial applications. Relative to this effort, the most promising of these licensed applications reports the capability for 3D printing of ceramic casting molds [Uziel – 1999]. The gating and risers for the mold assembly can be produced during the build process, and there is also the option of building in an integral core for creating a hollow component. To date, this process has been used primarily for aluminum castings, and the build tolerances are reported to be in the range of +/- 0.020” to +/- 0.025”. Also, the as-printed process yields a surface with stair-stepping in the range of 0.005” to 0.007”. While this capability does not yet meet the desired requirements for the small-featured demonstration components that are the short term focus of this effort, the ink-jet based 3D printing process merits consideration for future trials as the commercial capabilities are improved.

Stereolithography:

Stereolithography for rapid prototyping relies on the rapid photo-polymerization of acrylate or epoxy monomer resins exposed to strong ultraviolet (UV) light as the solidification mechanism. This process was the first to be widely deployed for commercial RP applications, and it remains one of the most popular techniques, owing to its overall versatility and capability for building complex geometries and fine features with high fidelity.

There are two basic approaches used to deliver the UV photons to the build chamber to create the two dimensional pattern for each layer. The more common format uses a two axis galvo-mirror based scanner to guide a tightly focused UV laser beam point by point across the desired layer pattern. The alternate approach delivers a broad field uniform UV beam to the entire area of the build chamber simultaneously, using a photomask to transmit the necessary 2D light pattern to polymerize a particular layer. This latter photomask approach has been made practical in recent years by the development of electronically re-configurable masking devices, such as those based on liquid crystals. The part is built on an elevator platform that moves up and/or down in the resin bath to replenish a fresh layer of liquid monomer for each cycle and adjust the position of the part as it builds up. In addition, a sweeper or wiper of some sort is typically used to effect a final leveling of the liquid surface at the start of a new layer.

Stereolithography has seen several applications for building parts from ceramic powders. In these instances the desired ceramic material in a fine powder form is mixed in with the photosensitive resin. Halloran’s group at the Univ. of Michigan has built demonstration versions of alumina casting cores using UV laser stereolithography processing of ceramic suspensions as dense as 50% volume fraction of sub-micron alumina particles [Brady & Halloran – 1995, Griffith & Halloran – 1996].

The addition of ceramic powder to the resin bath introduces two notable complications. Firstly, the high concentration of fine ceramic particles causes significant scattering of the UL laser beam, reducing the penetration depth in the ceramic suspension. Secondly, as the ceramic particles are more dense than the resin monomer, they tend to settle out of suspension under the influence of gravity. This is less of a practical issue for sub-micron particle powder. However, practical production casting cores are typically composed of coarser 5 – 10 micron powder particles, for which settling is rapid enough to introduce variation within the time required to scan one layer.

Laser Sintering:

Laser sintering is the final class of SFF process to be considered in this effort. Like 3D printing, the build material is distributed in the form of a dry powder in a powder bed. In laser sintering, like stereolithography, each layer is fabricated by scanning a tightly focused laser beam point by point across the desired layer pattern under computer control. A two axis galvo mirror scanner is most often used in laser sintering systems. Solidification occurs through local heating and partial melting of the fresh powder. The melted material wets the remaining solid particles, consolidating the layer through capillary action. The un-sintered powder remains in place in the build chamber, surrounding the part as it builds to serve as a support structure. Once the laser has scanned a particular layer to sinter the powder, the elevator platen in the build chamber is lowered by the amount of the nominal layer thickness and another layer of fresh powder is distributed and leveled with a scraper and/or roller fixture, and the process repeats itself over the pattern of the next layer. Once the part is completed, it is typically put through an additional furnace sintering step to further reduce the residual porosity inherent in the laser sintering process.

Laser sintering is arguably the most versatile freeform fabrication method, having been applied to a number of different polymer, metal, ceramic and composite powder materials since its inception in the mid 1980's [Bourell, et al. – 1992, Kruth, et al. – 2001, Kumar – 2003, Shellabear, et al. - 2004]. It is the applications for ceramic materials that are of direct interest to this effort, and several different materials studies have been documented in the literature. Initial work with ceramics utilized powder blends of a conventional laser sintering polymer powder with a second ceramic constituent such as alumina [Subramanian, et al. – 1995]. The polymer powder melts at a low temperature, wetting the ceramic and serving as a binder upon cooling. The green state part must then be processed with additional de-binding / furnace sintering steps to produce the final ceramic part. This 'indirect laser sintering' process uses a fairly high volume fraction of the polymer in the original blend that results in considerable shrinkage during the de-binding / furnace sintering operations, so the dimensional capability is a concern for manufacture of precision components.

The laser sintering of other two component powder blends such as alumina plus cobalt oxide or alumina plus ammonium dihydrogen phosphate have also been reported [Bourell, et al. – 1992], with one goal reported to be the manufacture of molds for casting applications [Lakshminarayan, et al. – 1990]. As with the polymer/ceramic combinations, the 2nd component is included to act as a lower melting point binder, creating, via liquid phase sintering, a green part that can be further consolidated through conventional furnace sintering steps.

Direct laser sintering of a single component ceramic powder (no additional binder) is the preferred approach for rapid prototyping of casting cores, since it offers a path to optimize dimensional stability and mechanical properties by eliminating the intermediate effects of using a binder. At the Fraunhofer Institute in Germany, direct laser sintering of zirconium silicate ($ZrSiO_4$) has been developed and applied for manufacture of shell molds and cores for metal castings [Klocke & Ader – 2004]. This same group had also studied direct laser sintering of other ceramic powders such as alumina and aluminum silicate along the path to determining that zirconium silicate showed the greatest promise for their applications. Direct laser sintering of ceramic powders has also been the subject of research efforts in France at the Ecole Nationale Superieure de Ceramique Industrielle (ENSCI), culminating in the development of a process for laser sintering complex components from materials such as alumina [Hory, et al. – 2004]. This last direct laser sintering process has since been commercialized by Phenix Systems, making it the most promising option to pursue in for the purposes of this subtask. In short, the process and hardware refined by this group offers, to the best of our knowledge, the only commercially available alternative to manufacture prototype ceramic cores using direct laser sintering.

### 4.2.13.3 - Results

The geometries for the two advanced cooling features were conceived and reduced to CAD format by the design team. These cooling passage concepts were incorporated in simple external geometries to avoid any possible concerns with proprietary airfoil designs. Several replicates of each feature were included in the concept samples to give multiple examples from which to assess manufacturing capability. The CAD model of the first demonstration part is shown in Fig. 4.2.13.1. This part was designed to include slender mid-wall cooling channels in a thin-walled cylindrical geometry. The cross section of the cooling channels is representative of the sorts of geometries under consideration by the design team. The corresponding core (negative) geometry for these cooling channels is shown in Fig. 4.2.13.2. This version contains a total of 16 channels equally spaced around the circumference. A close-up view of the core (negative) geometry for a sequence of four of the cooling channels is shown in Fig. 4.2.13.3. As a check on the CAD geometry, a Stratasys rapid prototyping machine using the Fused Deposition Modeling process was used to fabricate a prototype of this part in ABS polymer. The full scale ABS prototype is shown in Fig. 4.2.13.4.

The CAD model for this final core configuration was converted to a STEP format for input to the laser sintering system control software. The laser sintering system used for this effort was a Phenix Systems model PM-100 operated in the manufacturers applications lab. Alumina was used as the build material for this effort, because it is a common core material for airfoil castings and because the applications lab had considerable previous experience in optimizing the process parameters for this powder.

This particular system offers some unique features that enhance its practicality for ceramic parts. As discussed earlier, it utilizes direct laser sintering of the ceramic powder, without the need for any sort of polymer binders. Accordingly, there is no need to have an additional step to ‘burn off’ the binder material after the part is laser sintered, contributing to a more streamlined process and improved dimensional stability. The powder bed is maintained at an elevated temperature, which can be held as high as 900C, depending on the material. With the powder heated to a significant fraction of its solid state sintering temperature, the required laser power level to complete the sintering step is greatly reduced. As a result, this process operates with industrially robust fiber laser (1 um wavelength) of modest CW output power of 50W. Therefore, the laser spot size incident on the powder bed can be kept very small and carefully controlled, enhancing the geometric accuracy of the process. Improved geometric accuracy is also achieved through precise distribution and compaction of the powder for each layer. The layer thickness is confined to approximately 2 – 3 mils for each layer, enabling the fabrication of fine features and minimizing the magnitude of the stair-stepping that is characteristic of any layer-based rapid prototyping method. All of these characteristics contribute to a high degree of spatial uniformity in the ceramic microstructure that is largely independent of geometric complexities such as sharp thickness transitions, thin walls, and long, narrow channels. As a result, laser sintered ceramic parts exhibit very uniform porosity, that in turn contributes to uniform shrinkage and core strength as a function of part geometry. This represents an important advantage relative to conventionally injection molded ceramic cores, for which geometric complexities can lead to non-uniform material flow during injection and thus inhomogeneity in microstructure and material properties.

Nevertheless, laser sintering of the mid-wall channel geometry illustrated in Fig. 4.2.13.2 proved to be much more challenging, and thus time consuming, than was originally anticipated. The configuration with the slender channels supported only at one end by the cylindrical baseplate in a cantilever fashion was too unstable and compliant to produce complete parts reliably. After several attempts, the decision was made to modify the part geometry to address this issue. Several additional stiffening features were added to the STEP format CAD file of the sample, as shown in Fig. 4.2.13.5. First, a small rib was added to augment the attachment point for each of the 16 cantilevered cooling channels. Also, the channels themselves were connected by a thin strengthening wall running around the full circumference of the cylinder. Finally, a stiffening ring was added to connect the previously unsupported ends of the channels.

With these additional modifications implemented to enhance the mechanical stability of the part during the layer by layer build process, the new version was successfully laser sintered. The completed part is shown in Fig. 4.2.13.6, still resting in a bed of un-sintered alumina powder. In this picture, the part is oriented such that the cylindrical base is towards the top and the added stiffening ring is at the bottom. This was the extent of the progress towards laser sintering this geometry at the time this report was prepared. However, plans for future steps have already been established. Based on the successful laser sintering of this version of the part, the next iteration will be attempted without the strengthening wall that joins the individual channels. This modified CAD geometry is shown in Fig. 4.2.13.7. If this version can be manufactured in tact, it will provide the ability to characterize the geometry of the cooling channels produced by the laser sintering process without interference from the adjacent strengthening wall.

### 4.2.13.4 – Conclusions and future work:

This sub-task has completed the first steps towards establishing the capability to rapidly prototype ceramic casting cores for trials to manufacture the sort of prototype airfoil geometries that have emerged from the activities of the design team. Direct laser sintering of alumina has been successfully demonstrated for the building of precision core features for advanced cooling concepts, in particular, for slender mid-wall channels. In fact, it was quite encouraging to see how robustly the laser sintering produced the thin strengthening wall that had to be used to connect the cantilevered channels in the first sample. This wall was only about 0.015” thick, yet it was fully consolidated around the entire shell of the cylinder.

However, this sub-task only got under way in the final few months of the program phase II, and unexpected complications were encountered in the actual laser sintering effort, so much additional research remains. Obviously, it remains to begin and complete the initial evaluation of the laser sintering of the second concept geometry (trail edge bleed slots). This effort will undoubtedly benefit from the knowledge gained in processing the first geometry with the mid-wall channels. It is also expected that the design team will have additional concepts for advanced cooling geometries that involve fine core features that require evaluation. More generally, it is clear that the mechanical stiffness of the overall sample needs to be further studied to gauge the influence on the manufacturing capability of laser sintering. It is anticipated that the design team will offer great insight towards addressing this issue. It is likely that the sample design will benefit if brought more in line with actual core configurations that typically include a greater degree of interconnection between the various internal passages, and thus greater overall stiffness. In final conclusion, direct laser sintering of alumina has performed well enough to merit the additional research studies required to fully characterize the manufacturing capability that can be deployed for complex core prototyping.

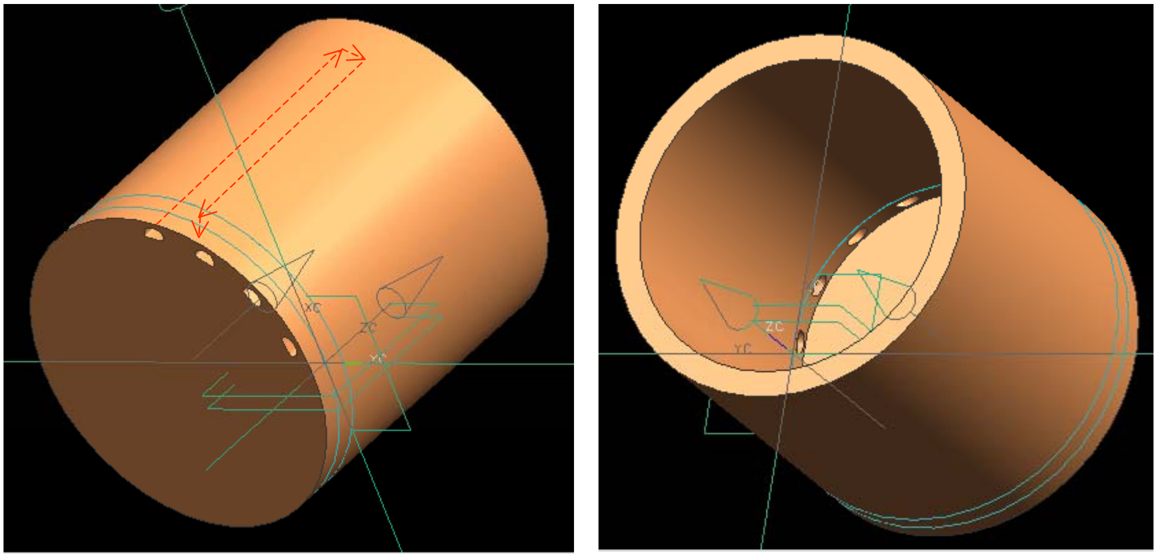

Figure 4.2.13.1: Solid model view of a representative thin wall cylinder containing four parallel mid-wall cooling channels. The approximate path of one of the channels is illustrated by the dashed red line.

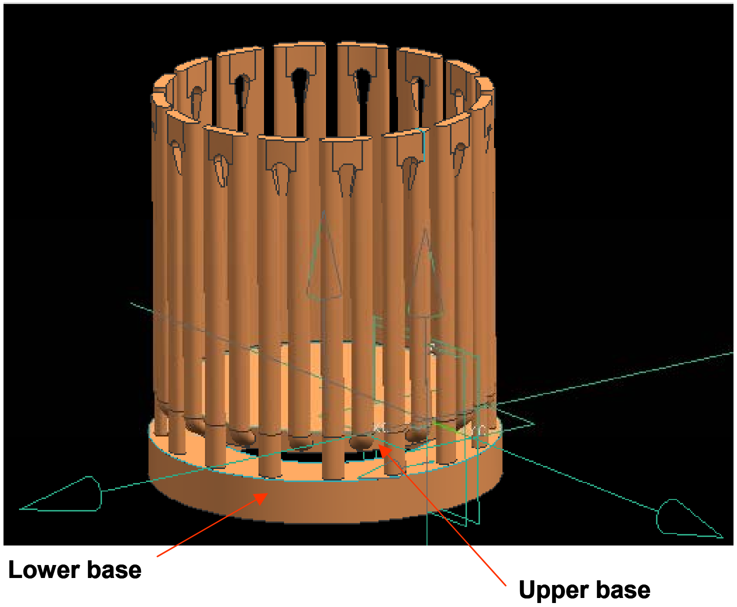

Figure 4.2.13.2: Solid model view of the casting core (negative) geometry showing a total of 16 parallel mid-wall cooling channels distributed on a cylindrical base. Although shown in this figure, the upper base is not necessary and will be omitted from the final build.

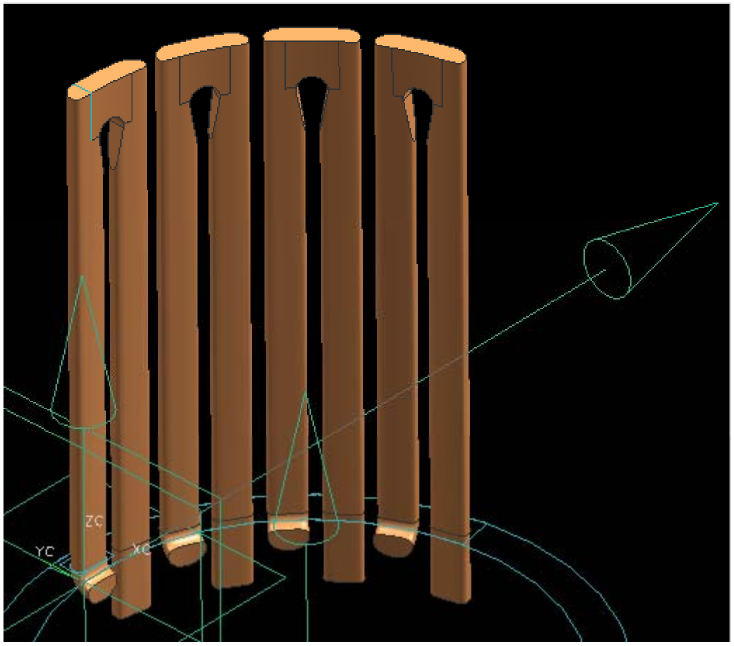

**Figure 4.2.13.3: Close up solid model view of the casting core (negative) geometry for four of the parallel mid-wall cooling channels.**

**Figure 4.2.13.4: ABS polymer prototype of of the casting core (negative) geometry for the concept sample containing 16 mid-wall cooling channels (Full scale).**

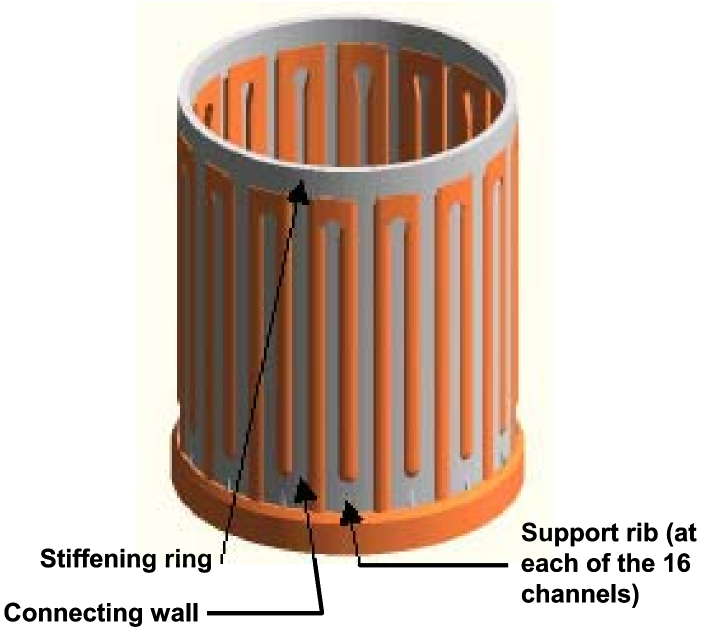

Figure 4.2.13.5: Solid model view of showing an alternate sample geometry that includes a stiffening ring, thin connecting wall & support ribs to aid in manufacturing the sample via direct laser sintering.

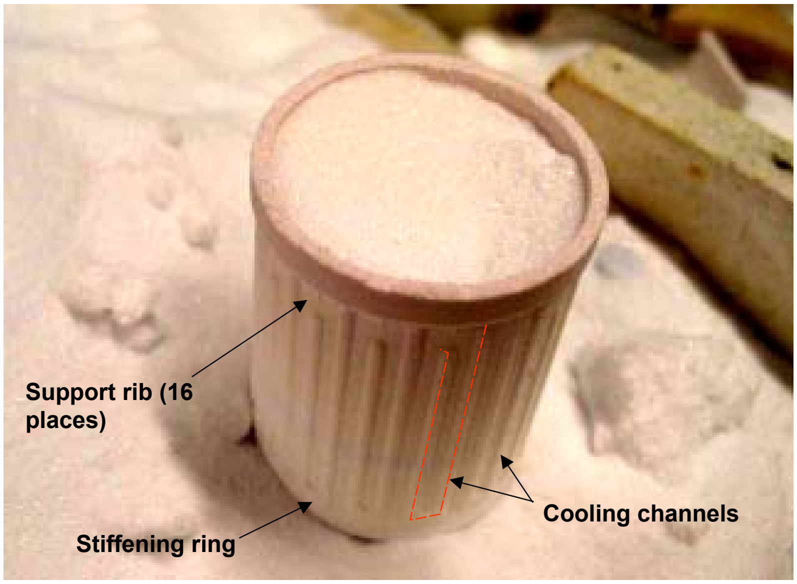

Figure 4.2.13.6: Direct laser sintered alumina part shown resting in alumina powder bed (the stiffening ring, thin connecting wall & support ribs are still in place).

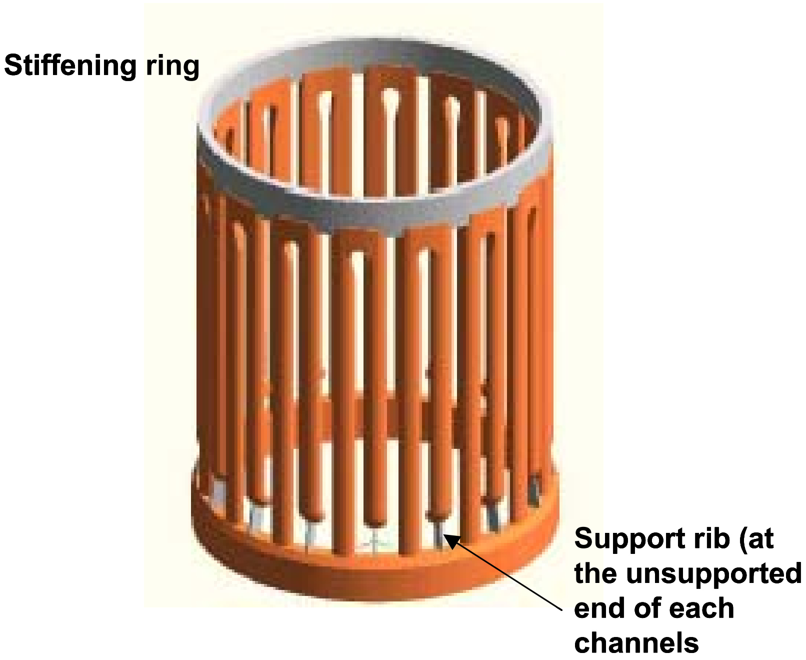

**Figure 4.2.13.7: Solid model view of showing a second alternate sample geometry that includes only a stiffening ring & support ribs to aid in manufacturing the sample via direct laser sintering.**

## 4.2.13.5 - References

Bourell, D.L., H.L. Marcus, J.W. Barlow & J.J. Beaman, “Selective Laser Sintering of Metals and Ceramics,” International Journal of Powder Metall., 28 (4) (1992), pp. 369– 381.

Brady, G.A. & John W. Halloran, "Stereolithography of ceramic suspensions," Rapid Prototyping Journal;Volume 3;Issue 2, pp. 61 – 65 (1997).

Cawley, James D., Zhien Liu, Wyatt S. Newman, Brian B. Mathewson, and Arthur H. Heuer, “Al2O3 Ceramics Made by CAM-LEM (Computer-Aided Manufacturing of Laminated Engineering Materials) Techonology," Solid Freeform Fabrication Symposium Proceedings, Austin, Texas, August 1995, pp. 9-16.

Cawley, James D., Arthur H. Heuer, Wyatt S. Newman, Brian B. Mathewson, "Computer-Aided Manufacturing of Laminated Engineering Materials," American Ceramic Society Bulletin, Volume 75, No. 5, May 1996, pp. 75-79.

Cima, Michael J. & Emanuel M. Sachs, “Three Dimensional Printing: Form, Materials, and Performance,” Solid Freeform Fabrication Proceedings, pp 187-194 (1991).

Griffith, M. L. and J. W. Halloran, “Freeform Fabrication of Ceramics via Stereolithography,” J. Am. Ceram. Soc., 79 [10], pp. 2601–608 (1996).

Hory, A., J.-M. Gaillard & P. Abelard, “Fast Prototyping Method by Laser Sintering of Powder,” US Patent No. 6767499-B1 (2004).

Klocke, F. & C. Ader, “Layer Manufacturing of Ceramic Materials,” Proceedings of 4th Laser Assisted Net Shape Engineering Conference (LANE-2004), Erlangen, Germany, pp. 505-510 (2004).

Klosterman, D., R. Chartoff, N. Osborne, G. Graves, A. Lightman, G. Han, A. Bezeredi, S. Rodrigues, "Direct Fabrication of Ceramics and CMCs by Rapid Prototyping," American Ceramic Society Bulletin, Vol. 77, No.10, October, 1998, pp. 69-74.

Klosterman, D., R. Chartoff, N. Osborne, G. Graves, A. Lightman, G. Han, A. Bezeredi, S. Rodrigues, "Development of a Curved Layer LOM Process for Monolithic Ceramics and Ceramic Matrix Composites," Rapid Prototyping Journal, Vol. 5, Issue 2, 1999, pp.61-71.

Kruth, J.P., X. Wang, T. Laoui & L. Froyen, “Lasers and Materials in Selective Laser Sintering,” Proceedings of 3rd Laser Assisted Nearshape Engineering Conference (LANE-2001), Erlangen, Germany, pp. 3 –24 (2001).

Kumar, S. “Selective Laser Sintering: A Qualitative and Objective Approach,” Journal of Metals, pp. 43–47 (2003).

Lakshminarayan, U., S. Ogrydziak & H.L. Marcus, “Selective Laser Sintering of Ceramic Materials,” Solid Freeform Fabrication Symposium Proceedings, Austin, Texas, August 1990, pp. 16 (1990).

Liu, Z.E., P. Wei, B. Kernan, A. H. Heuer, J. D. Cawley, “Metal and Ceramic Components made via CAM-LEM Technology,” Solid Freeform Fabrication Symposium Proceedings, Austin, Texas, August 1996, pp. 377-384 (1996).

Sachs, E., et al., “Three-Dimensional Printing: Rapid Tooling and Prototypes Directly from a CAD Model,” J. Eng. Ind., 114, 481–88 (1992).

Shellabear, M. & O. Nyrhila, “DMSL – Development history and state of the art,” Proceedings of 4th Laser Assisted Nearshape Engineering Conference (LANE-2004), Erlangen, Germany, pp. 393 – 404 (2004).

Subramanian, K., N. Vail, J. Barlow & H. Marcus, “Selective Laser Sintering of Alumina with Polymer Binders,” Rapid Prototyping Journal, 1 (2) (1995), pp. 24–35.

Uziel, Y., “Eliminating Prototype Tooling in Engine Castings,” presented at *Engine Expo ’99*, June, 1999, Hamburg, Germany (1999).

### 4.2.14 Pressure-Side Bleed Slot Producibility Assessment (Howmet)

#### Objective

The objective of this subtask was to produce castings with modified TE exits to evaluate ability to measure the thickness of the exits, effect on core and casting yields and collect final airflow data.

#### Technical Approach

#### Tooling

Construct new TE exit inserts to be used in a retired CFM56-7 HPB core die.

#### Ceramic Core Processing

The core die was chromed and cores were injected, fired and measured at Howmet Morristown. There was not a significant core yield difference relative to the baseline PS bleed slot design for this limited number of cores.

#### Castings

Cores were delivered to Howmet Whitehall. Wax patterns were injected, assembled into molds and cast off. NDI data was collected for all pertinent operations (fallout for cracked cores, autoclave rework, wall gauge, etc.). Parts are now fully processed and all the NDI and airflow data has been collected.

**REPORT DOCUMENTATION PAGE**

*Form Approved*
*OMB No. 0704-0188*

**1. REPORT DATE** *(DD-MM-YYYY)*
01-06-2008

**2. REPORT TYPE**
Final Contractor Report

**3. DATES COVERED** *(From - To)*
April 2005-August 2006

**4. TITLE AND SUBTITLE**
Intelligent Engine Systems
Thermal Management and Advanced Cooling

**5a. CONTRACT NUMBER**
NAS3-01135

**5b. GRANT NUMBER**

**5c. PROGRAM ELEMENT NUMBER**
4.2

**6. AUTHOR(S)**
Bergholz, Robert

**5d. PROJECT NUMBER**

**5e. TASK NUMBER**
37

**5f. WORK UNIT NUMBER**
WBS 984754.02.07.03.11.03

**7. PERFORMING ORGANIZATION NAME(S) AND ADDRESS(ES)**
General Electric Aviation
One Neumann Way
Cincinnati, Ohio 45215

**8. PERFORMING ORGANIZATION REPORT NUMBER**
E-16497

**9. SPONSORING/MONITORING AGENCY NAME(S) AND ADDRESS(ES)**
National Aeronautics and Space Administration
Washington, DC 20546-0001

**10. SPONSORING/MONITORS ACRONYM(S)**
NASA

**11. SPONSORING/MONITORING REPORT NUMBER**
NASA/CR-2008-215238

**12. DISTRIBUTION/AVAILABILITY STATEMENT**
Unclassified-Unlimited
Subject Category: 07
Available electronically at http://gltrs.grc.nasa.gov
This publication is available from the NASA Center for AeroSpace Information, 301-621-0390

**13. SUPPLEMENTARY NOTES**

**14. ABSTRACT**

The objective of the Advanced Turbine Cooling and Thermal Management program is to develop intelligent control and distribution methods for turbine cooling, while achieving a reduction in total cooling flow and assuring acceptable turbine component safety and reliability. The program also will develop embedded sensor technologies and cooling system models for real-time engine diagnostics and health management. Both active and passive control strategies will be investigated that include the capability of intelligent modulation of flow quantities, pressures, and temperatures both within the supply system and at the turbine component level. Thermal management system concepts were studied, with a goal of reducing HPT blade cooling air supply temperature. An assessment will be made of the use of this air by the active clearance control system as well. Turbine component cooling designs incorporating advanced, high-effectiveness cooling features, will be evaluated. Turbine cooling flow control concepts will be studied at the cooling system level and the component level. Specific cooling features or sub-elements of an advanced HPT blade cooling design will be downselected for core fabrication and casting demonstrations.

**15. SUBJECT TERMS**
Gas turbine engines; Turbines; Thermal management

| **16. SECURITY CLASSIFICATION OF:** | | | **17. LIMITATION OF ABSTRACT** | **18. NUMBER OF PAGES** | **19a. NAME OF RESPONSIBLE PERSON** |
|---|---|---|---|---|---|
| | | | | | STI Help Desk (email:help@sti.nasa.gov) |
| **a. REPORT** | **b. ABSTRACT** | **c. THIS PAGE** | | | **19b. TELEPHONE NUMBER** *(include area code)* |
| U | U | U | UU | 95 | 301-621-0390 |

Standard Form 298 (Rev. 8-98)
Prescribed by ANSI Std. Z39-18